Soft X-Ray-Assisted Detection Method for Airborne Molecular Contamination (AMC) and its Applications to AMC Filtration Issues

A DISSERTATION
SUBMITTED TO THE FACULTY OF
UNIVERSITY OF MINNESOTA
BY

Chang Hyuk Kim

IN PARTIAL FULFILLMENT OF THE REQUIREMENTS
FOR THE DEGREE OF
DOCTOR OF PHILOSOPHY

Dr. David Y.H. Pui

July 2016

Acknowledgements

I would like to express my sincere gratitude to my advisor Prof. David Y.H. Pui for his continuous guidance and mentoring throughout my graduate study. His instruction, advice, inspiration, encouragement, and patience have made the past five years the most memorable learning experience in my life.

I heartily thank my committee members: Prof. David B. Kittelson, Prof. Cari Dutcher and Prof Gurumurthy Ramachandran for reviewing my dissertation and offering valuable comments and suggestions. I would also like to thank Prof. Peter H. McMurry and Prof. Thomas H. Kuehn for serving as my committee members of the preliminary exam and offering valuable comments and suggestions.

I am also deeply grateful to my international collaborators: Prof. Heinz Fissan, Dr. Stefan Haep, Dr. Christof Asbach, Hartmut Finger and Ute Schneiderwind at the Institute of Environmental and Energy (IUTA e.V.) in Germany; Prof. Junji Cao and Jiamao Zhou at the Institute of Earth Environment, Chinese Academy of Science (IEECAS), Xi'an in China.

My sincere thanks also go to my current and former colleagues in the Particle Technology Laboratory: Dr. Shawn Chen, Dr. Shigeru Kimoto, Dr. Lin Li, Dr. Qisheng Ou, Dr. Tsz Yan Ling, Dr. Zhili Zuo, Drew Thompson, Leo Cao, Qinfeng Cao, Handol Lee, Seungkoo Kang, Chenxing Pei, Kai Xiao, Gustaf Lindquist, Dr. Mamoru Yamada and Dr. Ningning Zhang. Their company, discussion, and assistance have invaluable.

Thanks to the financial support from the Center for Filtration Research (CFR) at the University of Minnesota: 3M Corporation, A.O. Smith Water Products Company, BASF Corporation, Boeing Company, China Yancheng Environmental Protection Science and Technology City, Cummins Filtration Inc., Donaldson Company Inc., Entegris Inc., Ford Motor Company, Guangxi Wat Yuan Filtration System Co., Ltd., H.B. Fuller Company,

Mann+Hummel GmbH, MSP Corporation, Samsung Electronics Co., Ltd, Shigematsu Works Co., Ltd., TSI Inc., W. L. Gore & Associates, Inc., and Xinxiang Shengda Filtration Technology Co., Ltd. I also gratefully acknowledge the Department of Mechanical Engineering Fellowship in 2011 and the American Filtration and Separation Society Fellowship in 2015.

Finally, I am indebted to my parents and family (wife and three kids) for their constant love, trust and support.

Dedication

This dissertation is dedicated to all the graduate students
who are parents and take care of their children.

God Bless You, Parents!

Abstract

Airborne molecular contamination (AMC) represents a wide range of gas-phase chemical contaminants in cleanrooms. Because AMC can make defects of semiconductor chips by forming undesired nanoparticles and haze under ultra violet lights in the photolithography and change properties of semiconductor chips as dopants, developing methods for monitoring and controlling AMC is highly required in the semiconductor industry. This dissertation focuses on 1) development of a detection method for AMC and 2) its applications to AMC related issues in the semiconductor industry.

In the first study (Chapter 2), the detection method for AMC was developed by employing soft X-ray-assisted gas-to-particle conversion. Under soft X-ray irradiation, AMC was converted into nanoparticles, which were measured by the aerosol detection instrument, the scanning mobility particle sizer (SMPS). The soft X-ray-assisted detection method for AMC showed high sensitivity, e.g. down to ppt-level SO_2. By applying this method to evaluate the filtration efficiency of two AMC filters, a better AMC filter was determined based on the concentration of SO_2 downstream of the AMC filters measured by the method.

Even though gas contaminants in outdoor air are removed by gas filters, AMC can be emitted from many kinds of materials used in cleanrooms, such as organic solvents and construction materials. Volatile organic compounds (VOCs) from the materials also work as organic AMC in cleanrooms. In the second study (Chapter 3), the soft X-ray-assisted detection method was employed to screen cleanroom-use materials and find replacements emitting low-VOCs. This method was applied to measure VOCs from different organic

solvents and adhesives and showed good repeatability and high sensitivity to VOCs. When VOCs from cleanroom-use adhesives were measured by this method, the overall trend was well-matched with those measured by a widely used commercial method, thermal desorption-gas chromatography-mass spectrometry (TD-GC-MS). Based on the results, this screening method can help save costs and accelerate developing low-VOC materials for better cleanroom air.

In the third study (Chapter 4), the soft X-ray-assisted detection method was applied to measure outgassing from particulate air pollutants ($PM_{2.5}$), which is currently an important global pollution issue. Even though $PM_{2.5}$ is removed by particles filters, chemicals adsorbed on its surface can be outgassed and carried into cleanrooms, which is another source of AMC. The soft X-ray method was applied to determine the relation between the outgassing and $PM_{2.5}$ mass loading and showed a linear relationship between them. The simultaneous conducted chemical analyses showed a strong relation between organic carbons and the outgassing. Moreover, TD-GC-MS results showed the effect of the sampling location on the composition of the outgassing from $PM_{2.5}$.

For evaluating granular activated carbons (GACs) as filters for both gaseous and particulate contaminants using their pores and external surfaces, the soft X-ray-assisted detection method was employed to investigate the particle filtration efficiency of the GACs and the effects of the filtered particles on changing gas filtration efficiency of the GACs in the following studies. In the fourth study (Chapter 5), the filtration efficiency of the GACs for 3-30 nm particles with different compositions was obtained at different face velocities. The particle filtration behavior of the GACs followed conventional filtration theories, but

the single unit efficiency of the GACs was not matched with the previous single sphere efficiency.

In the fifth study (Chapter 6), the particle filtration efficiency of the GACs was measured for sub-3 nm particles, which was overlapped with that for 3-30 nm particles in the fourth study. When the particle filtration efficiency of the GACs was compared with that of the fibrous filters, the GACs showed lower filtration efficiency than the fibrous filters. However, the GACs had 90% filtration efficiency for sub-3nm particles in the present work and can be used to remove nanoparticles and AMC simultaneously.

Even though the GACs can remove both gaseous and particulate contaminants using their pores and external surfaces, the filtered particles may block the pores and reduce the gas filtration efficiency of the GACs. For evaluating the effects of the filtered particles on changing gas filtration efficiency of the GACs, the penetration of toluene through the GACs was measured as a function of time in the sixth study (Chapter 7) using the soft X-ray-assisted detection method, when the GACs were challenged with or without nanoparticles. As a results, the time-dependent toluene penetration curves showed no significant effect of the filtered particles on the gas adsorption efficiency. The particle filtration efficiency of the GACs did not change after filling the pores of the GACs with toluene molecules. The experimental results revealed that the gas and particle filtration occurred on the pores and the external surface of the GACs, respectively. Therefore, the GACs can be used to remove both gaseous and particulate contaminants simultaneously.

These four studies below comprise parts of the main body of this dissertation and have been published or are currently under review. Chapter 4 and 7 are in preparation for submission.

Chapter 2: Kim C, Zuo Z, Finger H, Haep S, Asbach C, Fissan H, Pui DYH (2015) Soft X-ray-assisted detection method for airborne molecular contaminations (AMCs), *Journal of Nanoparticle Research*, 17:126

Chapter 3: Kim C, Sul Y, Pui DYH. Real-time and n-line screening method for materials emitting volatile organic compounds, *Journal of Nanoparticle Research*, currently under review

Chapter 5: Kim C, Pui DYH (2015) Experimental study on the filtration efficiency of activated carbons for 3-30 nm particles, *Carbon*, 93:226–229

Chapter 6: Kim C, Kang S, Pui DYH (2016) Removal of airborne sub-3 nm particles using fibrous filters and granular activated carbons, *Carbon*, 104:125–132

Table of Contents

List of Tables

List of Figures

I. Introduction

Chapter 1: Introduction

1.1 Background

1.1.1 Airborne molecular contamination (AMC)

Semiconductors have brought convenient life-style as a part of modern portable electronic devices (e.g. laptop computers, tablets, smart phones and smart watches). Advanced semiconductor manufacturing technologies have facilitated the advance of semiconductors with smaller size, higher performance and lower power consumption by increasing the number of transistors in a dense integrated circuit. However, the advanced manufacturing technologies also have required strict standards for controlling particulate and gaseous contaminants in cleanrooms to enhance the yield of products (Sematech International 2011).

In the semiconductor industry, many efforts have been made to avoid particulate contaminants because the deposited particles on masks and wafers can cause defects and failures of semiconductor devices. For preventing particulate contaminants from entering cleanrooms, air filtration systems including high efficiency particle air (HEPA) and ultra-low particulate air (ULPA) filters have been installed in the manufacturing fab (Donovan 1990). However, as advanced photolithography technologies using shorter wavelength ultraviolet (UV) (e.g. 248 nm KrF, 193 nm ArF and 14 nm extreme UV) are used in photolithography to pattern narrower lines on silicon wafers (Ito and Okazaki 2000), a new gaseous contamination problem has been identified in cleanrooms, which are airborne

molecular contamination (AMC) (Den et al. 2006; Weineck et al. 2010; Sematech International 2011).

AMC represents a wide range of gaseous contaminants at ultra-low concentrations, down to part per billion (ppb, 10^{-9}) or part per trillion (ppt, 10^{-12}) levels in cleanrooms. Semiconductor equipment and materials international (SEMI) categorizes AMCs into four groups such as acids, bases, condensables and dopants by the standard, SEMI F21-95 (SEMI Standard F21-95 1996). The chemical nature of AMC can be organic or inorganic. Based on the potential health effects, AMC is classified as toxic, corrosive, irritant and odorous (Geng 2005). AMC can originate from inside and outside of cleanrooms, e.g. wet chemicals of the semiconductor manufacturing processes (Lin et al. 2010), outgassing from the construction materials of cleanrooms (Dallas et al. 2002) and outdoor air pollutants (Tamaoki et al. 2010a). Personnel working in cleanrooms are also major sources of AMCs (Weineck et al. 2010). Even though the concentration of AMC is extremely low, undesired elements can be doped in the wafers and change their electrical properties, etch rates and threshold voltages (Stevie et al. 1991; Lebens et al. 1996; Geng 2005). In particular, tiny amounts of AMC can produce particles and haze when it is exposed to UV lights in the photolithography (Lobert et al. 2009; Lobert et al. 2010; Pic et al. 2010; Gordon et al. 2005; Gordon et al. 2007b; Gordon et al. 2007a; Gordon et al. 2009; Weineck et al. 2010; Den et al. 2006). The unfavorable contamination and property changes cause defects and failures of manufacturing systems (e.g. lens and photomask) and/or patterned silicon wafers. Therefore, developing methods for monitoring and controlling AMC in cleanrooms is currently urgent.

1.1.2 Gas-to-particle conversion

The gas-to-particle conversion (i.e. generation of nanoparticles from AMC) can be observed in the atmosphere, e.g. sulfuric acid (H_2SO_4) particles from sulfur dioxide (SO_2) and secondary organic aerosols (SOAs) from hydrocarbon (HC)/NOx mixtures (Kulmala 2003; Kulmala et al. 2004; Zhang et al. 2004; Sihto et al. 2006; Kuang et al. 2008).

Some atmospheric researchers also have studied particle formations through the gas-to-particle conversion process experimentally in the laboratory with chambers and external energy sources, e.g. particle formation from SO_2/dry Ar mixtures after being exposed to a β-source (Wood et al. 1975), from SO_2/NH_3/humid air mixtures under a UV (Christensen et al. 1992; Christensen et al. 1994), from SO_2/NH_3/humid air assisted by α-ray ionization using a radioactive source, ^{241}Am Kim et al. (Kim et al. 1998) and from SO_2/NH_3/humid air mixtures under galactic cosmic rays (Kirkby et al. 2011). Berndt et al. (Berndt 2005; Berndt et al. 2006; Berndt et al. 2008; Berndt et al. 2010) investigated H_2SO_4 particle formation from SO_2-containing gas mixtures using a UV light and Laaksonen et al. (Laaksonen et al. 2008) compared their experimental results with the results measured in the atmosphere. The mechanism for H_2SO_4 particle formations from SO_2 is well described in Kim et al. (Kim et al. 1998) and Christensen et al. (Christensen et al. 1994).

Kleindiest, Edney and their colleagues (Kleindienst et al. 1999; Edney et al. 2001; Kleindienst et al. 2002; Kleindienst et al. 2004) investigated the SOAs formation when HC/NO_x mixtures were irradiated by a UV in a smog chamber. Others conducted similar experiments using outdoor smog chambers under sunlight (Forstner et al. 1997; Jang and Kamens 2001). Hildebrandt et al. (Hildebrandt et al. 2009) showed particle formation as a

function of time under a UV irradiation by batch experiments. Through the gas-to-particle conversion process under a UV light, Katz et al. (Katz et al. 1977; Katz et al. 2000) detected explosive materials, such as 2,4,6-trinitrotoluene (TNT). In the semiconductor industry, the UV of the photolithography instrument has shorter wavelength and higher energy, thus producing nanoparticles (or haze on the surface) even at the ppb or ppt-level AMC.

1.1.3 Detection methods for AMC in cleanrooms

Due to the adverse effects of AMC, highly sensitive detection methods for AMC should be employed in the semiconductor industry. International technology roadmap for semiconductors (ITRS) recommends UV fluorescence analyzer and gas chromatography-mass spectrometry (GC-MS) for detecting AMC in cleanrooms (Den et al. 2006; Sematech International 2011). Quartz crystal microbalance (QCM) also has been used to detect AMC in cleanrooms (Habuka et al. 2005). However, the UV fluorescence analyzer can only detect sulfur dioxide (SO_2) and is not for organic AMC. For the GC-MS analysis, sampling AMC in cleanrooms using adsorbent tubes is required prior to the analysis at off-sites, which cannot provide real-time information for AMC in cleanrooms. In addition, the QCM measures contaminants based on the frequency change of the quartz crystal due to the mass change by corrosive reactions and film growth, but it is not available for regeneration after using it.

Chemical ionization mass spectroscopy (CI-MS) (Munson and Field 1966; Smith et al. 2004; Huey et al. 2004; Zhao et al. 2011) and proton transfer reaction mass spectroscopy (PTR-MS) (Kim et al. 2009; Blake et al. 2009; Jordan et al. 2009) are frequently used in the atmospheric sciences, but they are difficult to apply for detecting

AMC in cleanrooms due to their limitations such as fragmentation, proton affinity, as well as costs.

1.1.4 Granular activated carbon (GAC) for removing AMC in cleanrooms

The chemical nature and gaseous form of AMC do not allow conventional particulate filters to prevent AMC from entering cleanrooms during semiconductor manufacturing processes. For removing AMC, additional gas-phase air filtration system should be installed next to the particle filtration system. Activated carbons (ACs) are widely used as the gas-phase air filters in the semiconductor industry to capture AMC through adsorption, which is a surface-based process defined as the adhesion in an extremely thin layer of molecules (adsorbate) to the surfaces of solid bodies (adsorbent) by weak van der Waals forces (physisorption) or by strong chemical bonds (chemisorption) (McCash 2001).

Activated carbons (ACs) are widely used materials for gas and liquid filtration through adsorption. Due to their highly developed porosity, large surface area, variable characteristics of surface chemistry and high degree of surface reactivity, ACs are very effective adsorbents for gaseous contaminants and aqueous pollutants in liquids (Bansal and Goyal 2005; Dias et al. 2007). By using their advanced physical and chemical properties, ACs have been used in a wide range of applications for air and water treatments, e.g. drinking and waste water filters, respirators, car cabin air filters, aircraft cabin air filters, home air purifiers and cleanrooms.

Due to the different shapes of ACs, they can be categorized into four groups as described in Table 1-1: granular activated carbon (GAC), powdered activated carbon

(PAC), activated carbon fiber (ACF) and activated carbon fiber cloth (ACFC) (Dias et al. 2007). Among the different kinds of ACs, GAC has been employed substantially in the semiconductor industry as the AMC filter.

Table 1-1. Four groups of activated carbons and their key features

Activated Carbons	Precursors	Size	Features
GAC	**Hard materials (e.g. coconut shell, coal)**	**0.177-5 mm**	**Column filler for gas and liquid treatment, available for regeneration**
PAC	**Small-sized materials (e.g. wood sawdust)**	**< 0.177 mm**	**Mixed with liquids to be treated and disposed of, very effective (small particle) but slower setting and removal**
ACF	**Homogeneous polymeric raw materials (e.g. PAN, rayon, novoloid)**	**7 – 15 μm dia.**	**Thin-fiber shape, enhanced intra-particle adsorption, improved contact efficiencies**
ACFC	**Woven or knitted cloths**		**Low pressure drop, high contact efficiency, flexibility**

For the use of GAC, sandwich-structure non-woven fibrous filters or containers are used to hold it (Kim et al. 2015; Kim and Pui 2015; Kim et al. 2016a). Depending on the chemical nature of AMC, the filtration performance of GAC can be enhanced by chemical treatments or coating catalysts (Figueiredo et al. 1999; Chen et al. 2003; Chingombe et al. 2005; Mugisidi et al. 2007; Rivera-Utrilla and Sánchez-Polo 2011; Yong et al. 2001;

Sharma et al. 2013; Weineck et al. 2010). However, the additional fibrous filter layers and chemical impregnations increase undesired pressure drops across the AMC filter and its manufacturing costs, which is undesirable for controlling cleanroom air quality (Weineck et al. 2010). An alternative way is designing a new filtration system by integrating the gas and particulate filters. If GAC can be used to remove nanoparticles using its external surface as a packed-beds filter, at least the fibrous filter in front of the GAC can be eliminated or replaced with a low-pressure drop filter. Even though the low-pressure drop filter has lower particle filtration efficiency than the original one, GAC can compensate for the discrepancy. Then, nanoparticles and gas molecules can be removed simultaneously by a single gas filter, GAC. For the new filtration concept, the effect of the filtered particles on the gas filtration efficiency of the GAC should be investigated as a function of time.

1.1.5 Particulate matter smaller than 2.5 μm ($PM_{2.5}$)

$PM_{2.5}$ represents particulate matter smaller than 2.5 μm in aerodynamic diameter. The U.S. Environmental protection agency (USEPA) has established it in 1997, and its current standard is 35 $\mu g/m^3$ over a 24h and 12 $\mu g/m^3$ for annual average in the U.S. (Pui et al. 2014). $PM_{2.5}$ is 1) emitted from vehicles, restaurants and industries after using energy sources (e.g. coal, oil, natural gas, gasoline, diesel and wood) and 2) synthesized through the photochemical reactions of gas contaminants (e.g. volatile organic compounds and polycyclic aromatic hydrocarbons) in the air under sunlight, which are also known as secondary organic and inorganic aerosols (Jimenez et al. 2009; Fu et al. 2012; Huang et al. 2014; Kim et al. 2015). If the concentration of $PM_{2.5}$ is high, it can cause various problems on the environment and human health, such as climate change, visibility reduction and

respiratory diseases, which are currently observed in many countries, such as China, India and Korea (Menon et al. 2002; Akimoto 2003; Tiwari et al. 2010; Cao et al. 2012a; Park et al. 2013).

$PM_{2.5}$ is also detrimental for the semiconductor industry by making defective semiconductor chips when it is deposited on silicon wafers and photo masks during semiconductor manufacturing processes. Although $PM_{2.5}$ was removed from the outdoor air by HEPA filters, the filtered $PM_{2.5}$ can outgas chemicals adsorbed on its surface and then reduce the lifetime of the gas-phase air filters by working as AMC in the semiconductor manufacturing fab. Therefore, semiconductor fabs located in areas with high concentration of $PM_{2.5}$ should change both particulate and gas filters more frequently due to the filtered $PM_{2.5}$ and its outgassing. To optimize the changing period of the filters, the relation between $PM_{2.5}$ and its outgassing should be investigated, but they have not been studied much yet.

1.2. Research objectives

The objectives of this study were to 1) develop a new detection method for AMC and 2) apply this method for investigating issues related to AMC filtration in cleanrooms.

For detecting AMC, the detection method should be on-line, simple, applicable for both inorganic and organic AMCs. High sensitivity to AMC, which can determine ppt-level AMC, is also necessary to meet the strict concentration limit for controlling AMC in cleanroom air. To meet these requirements, a detection method for AMC was developed in this dissertation by simulating the particle formation from AMC in the photolithography (the gas-to-particle conversion) assisted by soft X-ray, instead of UV lights.

The soft X-ray-assisted detection method for AMC was applied to a) evaluate the time-dependent gas filtration efficiency of AMC filters (e.g. GAC), b) screen from cleanroom-use materials by measuring their outgassing and c) determine the relation between $PM_{2.5}$ and its outgassing. In addition, the method was employed to determine d) the particle filtration efficiency of GACs and e) the effects of the filtered particles on the gas filtration efficiency of GACs. This fundamental study can provide the background knowledge for designing new filtration systems to control nanoparticles and AMC simultaneously in cleanrooms by integrating the gas and particulate filters.

1.3 Dissertation outline

This dissertation is organized in the following manner. A brief review of the topic of this dissertation is presented in this chapter. The next six chapters comprise the main body of the dissertation, each based on a separate manuscript that has been published, is currently under review or is in preparation for submission. Chapter 2 describes the newly developed method for detecting AMC assisted by soft X-ray and its application to evaluate the gas filtration performance of two GAC filters to SO_2 as a function of time. Chapter 3 discusses the use of the soft X-ray-assisted detection method to screen cleanroom-use materials by measuring their outgassing. In Chapter 4, the soft X-ray method is applied to determine the relation between $PM_{2.5}$ mass loading and its outgassing, and the result is compared with the chemical composition of the $PM_{2.5}$ samples, e.g. organic carbon/elementary carbon (OC/EC), water soluble ions and organic compounds. Through Chapter 5-7, the soft X-ray method is employed in the experimental setup to determine the particle filtration efficiency of GACs and the effects of the filtered particles on changing

gas filtration efficiency of GACs in series. In particular, Chapter 5 reports the filtration efficiency of GACs for 3-30 nm particles at different particle compositions and face velocities. Subsequently, Chapter 6 addresses the filtration efficiency of GACs for sub-3 nm particles and compares the results with those of fibrous respirators. In Chapter 7, the effect of the filtered particles on gas filtration efficiency of GACs is presented by measuring the time-dependent penetration of toluene through the GACs. Finally, the conclusion and future works are given in Chapter 8.

II. Detection of AMC

Chapter 2: Soft-X-Ray-Assisted Detection Method for AMC

2.1 Introduction

Over the last two decades, the integration and performance of semiconductor chips have been improved dramatically by employing advanced photolithography technologies to transmit smaller patterns from masks to silicon wafers (Ito and Okazaki 2000), which facilitated the advances of modern electronic devices such as computers, mobile-phones and TVs. In the semiconductor industry, avoiding particulate contaminations is critical to enhancing the yield of products because the deposited nanoparticles on masks and wafers can cause defects of semiconductors, thus increasing manufacturing costs. Therefore, many efforts have been made to develop filtration systems including high efficiency particulate air (HEPA) and ultra low particulate air (ULPA) filters for eliminating particulate contaminations (Donovan 1990).

However, as shorter wavelength ultraviolet (UV) light sources, such as a 248 nm KrF and 193 nm ArF excimer laser, are used in the advanced photolithography (Ito and Okazaki 2000), new contamination problems have been highlighted in cleanrooms, which are airborne molecular contaminations (AMCs) (Den et al. 2006; Weineck et al. 2010). AMCs represent a wide range of gaseous contaminants at very low concentrations, down to parts-per-billion (ppb, 10^{-9}) or parts-per-trillion (ppt, 10^{-12}) levels in cleanrooms. Semiconductor Equipment and Materials International (SEMI) categorizes AMCs into four groups, i.e. acids, bases, condensables and dopants by the standard, SEMI F21-95 (SEMI Standard F21-95 1996). AMCs can originate from inside and outside cleanrooms and can

include wet chemicals of the semiconductor manufacturing processes (Lin et al. 2010), air pollutants (Tamaoki et al. 2010b) or construction materials (Dallas et al. 2002). Personnel working in cleanrooms are also major sources of AMCs (Weineck et al. 2010). Even though the concentrations of AMCs are extremely low, they may lead to an undesired doping of the semiconductors (Stevie et al. 1991; Lebens et al. 1996). Additionally, nanoparticles or haze can form when gaseous AMCs are exposed to the UV lights of the photolithography (Gordon et al. 2005; Den et al. 2006; Lobert et al. 2009; Pic et al. 2010; Weineck et al. 2010). For example, acidic AMCs from cleaning processes with wet chemicals can react with basic AMCs from other cleaning processes through gas-to-particle conversion under the UV irradiation, thus generating unintentional salt nanoparticles (air-borne). Also, haze (surface-borne) can be grown on the surfaces of optical parts, such as lens and mask, if the conversion occurs from chemical residues on the surfaces from diverse manufacturing processes such as cleaning processes and photoresists. These unintentionally synthesized contaminations cause defects and failures of optical systems and/or patterned silicon wafers. Due to the adverse effects of AMCs, monitoring and controlling of AMCs are now important issues in the semiconductor industry. Furthermore, AMCs are still not well understood, which makes them difficult to monitor and control (Lobert et al. 2009; Lobert et al. 2010; Weineck et al. 2010).

Nevertheless, only a few detection methods, such as UV fluorescence analyzer and gas-chromatography-mass spectroscopy (GC-MS), have been used to monitor AMCs in cleanrooms as per the recommendation by International Technology Roadmap for Semiconductors (ITRS) (Den et al. 2006; Sematech International 2011). Although a UV

fluorescence analyzer is relatively cheap, it can only detect sulfur-containing inorganic compounds such as sulfur dioxide (SO_2). In addition, GC-MS is an off-line detection method which determines average contamination levels for long sampling time. Other gas detection and analysis methods, chemical ionization mass spectroscopy (CI-MS) (Munson and Field 1966; Smith et al. 2004; Huey et al. 2004; Zhao et al. 2011) or proton transfer reaction mass spectroscopy (PTR-MS) (Kim et al. 2009; Blake et al. 2009; Jordan et al. 2009) are frequently used in the field of atmospheric sciences, but they are seldom applied for detecting AMCs in cleanrooms due to their limitations such as fragmentation (CI-MS), proton affinity (PTR-MS) as well as costs. A detection method, which is economical, on-line and applicable for diverse AMCs including inorganics and organics, is not available now in cleanrooms.

For controlling AMC levels in cleanrooms, chemical filters, which capture AMCs by adsorption, have been developed and installed in cleanrooms in addition to the particle filters (Lobert et al. 2009; Lobert et al. 2010). Because the adsorption efficiency depends on the porosity and specific surface area of the media, granular activated carbons (GACs) are widely used as chemical filter media. Depending on the chemical nature of AMCs, GACs are modified by chemical treatments or coating catalysts to enhance their adsorptive performance (Figueiredo et al. 1999; Yong et al. 2001; Chen et al. 2003; Chingombe et al. 2005; Weineck et al. 2010). Sometimes, new filtration systems are designed to remove particular AMCs (Lobert et al. 2010; Weineck et al. 2010). For evaluating the improved performance of the modified chemical filters, reliable detection methods are also highly

required to measure the ultra-low concentrations of AMCs behind the chemical filters (Lobert et al. 2009; Riddle Vogt and Landoni 2011).

The objectives of this research were (1) to develop a new detection method for AMCs through soft X-ray assisted gas-to-particle conversion (converting gaseous AMCs into nanoparticles), which is economical, on-line and applicable for diverse AMCs with a detection limit, down to ppt-levels, better than existing methods and (2) to conduct a feasibility study of this method by applying for evaluating the filtration performance of chemical filters to AMCs as a reliable detection method. GACs and SO_2 were used for the feasibility study.

2.2 Materials and methods

Particle formation from gases, such as binary homogenous nucleation (BHN) of sulfuric acid and water (H_2SO_4/H_2O) from SO_2 and secondary organic aerosols (SOAs) from hydrocarbon (HC) mixtures, can be frequently observed in the atmosphere (Kulmala et al. 2004; Sihto et al. 2006; Hildebrandt et al. 2009). Many researchers working in the field of atmospheric chemistry have investigated the nanoparticle formation through gas-to-particle conversion in the laboratory using a chamber with an external energy source such as UV light, sunlight or α-ray (Christensen et al. 1994; Forstner et al. 1997; Kim et al. 1998; Kleindienst et al. 1999; Berndt 2005; Hildebrandt et al. 2009; Kirkby et al. 2011). Using the gas-to-particle conversion, Katz et al. (Katz et al. 2000) presented a detection method with a UV light for explosive 2,4,6-trinitrotoluene (TNT) in the environment. Although some of them showed particle formations from gas contaminations at sub-ppb-

levels in terms of particle number concentrations (Katz et al. 2000; Kirkby et al. 2011), these were too low due to the low external energy strength. This means low sensitivity to gas compounds if these methods are used for gas detection. Therefore, soft X-ray was employed to obtain high sensitivity to gas compounds of the new AMC detection method developed in this study.

AMC detection method through gas-to-particle conversion assisted by soft X-ray

A schematic diagram of the soft X-ray assisted detection method is depicted in Figure 2-1a, which employs gas-to-particle conversion using a 9.5 keV soft X-ray (Sunje Hi Tek, SXN-10F). The energy of the soft X-ray corresponds to a sub-nanometer wavelength, which is much shorter than the commercial UV lights such as ArF (248 nm) and KrF (193 nm) in photolithography (Attwood 2000). The extremely short wavelength makes it possible to see smaller features in microscopy and write smaller patterns in lithography (Bailey et al. 1982; Chao et al. 2005). Moreover, the soft X-ray has higher ionization energy to produce bipolar ions than radioactive materials such as a ^{241}Am, α-ray source (Han et al. 2003), which enables gases to be converted into nanoparticles by the ion-induced nucleation (Yun et al. 2009). In the conversion chamber, radicals, such as hydroxyl radicals, can be produced from water molecules in the gas mixture after exposed to the soft X-ray. These radicals can react with SO_2 to generate intermediate particle forms such as HSO_3. The final products, such as nano-sized H_2SO_4 particles, are synthesized by the reactions between the intermediate particles and water molecules (Kim et al. 1998). If the H_2SO_4 particles react with ammonia (NH_3), ammonium sulfate ($(NH_4)_2SO_4$) particles can

be synthesized. This is one of salt nanoparticle formation mechanisms in the photolithography. The nanoparticle formation under the soft X-ray may also show one of AMC problems in cleanrooms because soft X-ray is one of candidate light sources for the next generation photolithography (Bailey et al. 1982; Attwood 2000; Ito and Okazaki 2000). The cylindrical conversion chamber, where nanoparticles are generated under the soft X-ray irradiation, has a dimension of Φ 127 x 203 mm (Φ 5 x 8 in.). To minimize outgassing from the system, the chamber and tubing were made of stainless steel and baked at 200 $^{\circ}$C for at least 2 hours before experiments to eliminate contaminants desorbed from the conversion chamber wall.

Target gas mixtures for the detection method were sampled by vacuum pumps in the particle measurement systems including an ultrafine condensation particle counter (UCPC, TSI model 3776) and a scanning mobility particle sizer (SMPS, TSI model 3936N76) and introduced into the conversion chamber. The particle generation in the chamber was monitored by the UCPC, and then the size distributions of particles were measured by the SMPS. The aerosol flow rate of the UCPC was fixed at 1.5 lpm and the aerosol flow rate and the sheath flow rate of the SMPS were set at 1.5 lpm and 15 lpm, respectively with constant measuring times (120 s for the scan time and 15 s for the retrace time). With these settings, the SMPS measured number size distributions of generated nanoparticles in a size range from 2.5 to 65 nm. All particle number concentrations were obtained by integrating the size distributions measured by the SMPS. Particle volume concentrations were also calculated from the size distributions assuming all generated particles were spheres. Depending on the nature and concentration of the target gas,

appropriate gas analyzers can be used to measure corresponding gas concentrations simultaneously.

a)

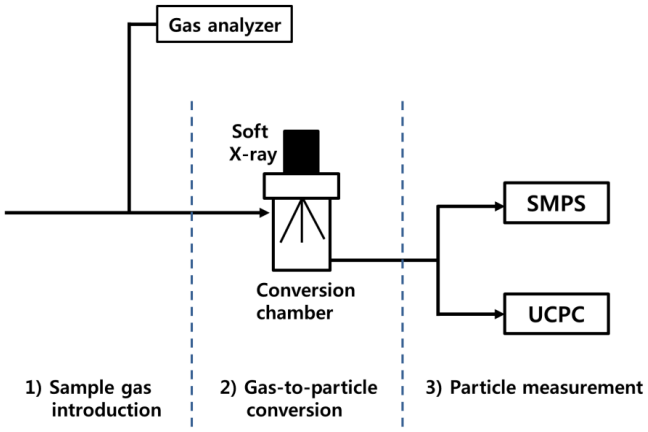

b)

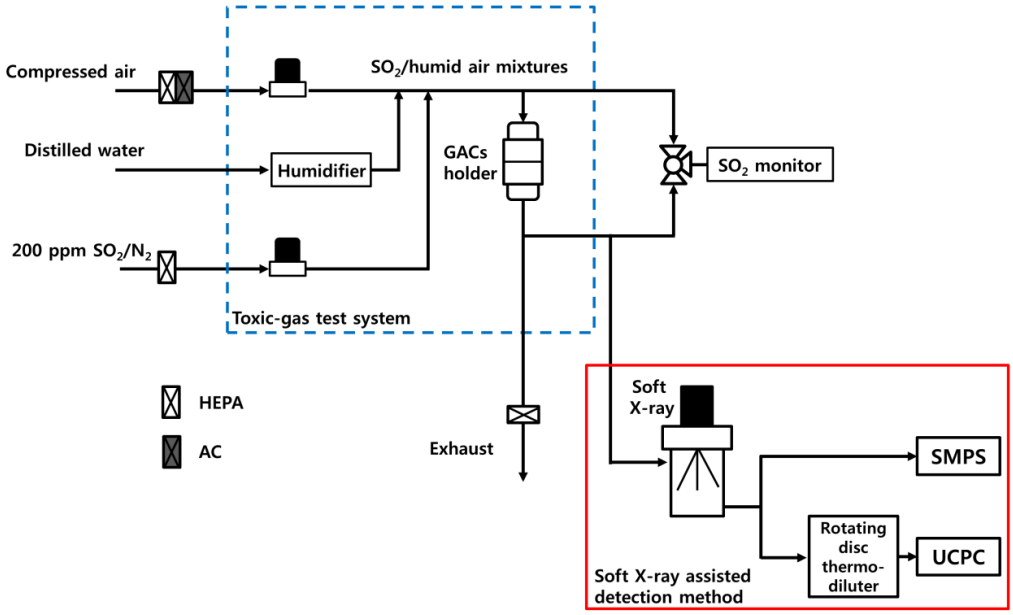

Figure 2-1. (a) Schematic diagram of the soft X-ray assisted detection method for AMCs and (b) experimental setup for the evaluation tests of GACs combined with the method

Feasibility study of the soft X-ray assisted detection method

The feasibility study of the soft X-ray assisted detection method was conducted through the evaluation tests of GACs using the experimental setup as shown in Figure 2-1b with SO_2, which is one of major AMCs. However, the available gas filter media and AMCs are not limited to those tested in the present work. For example, toluene (Hildebrandt et al. 2009) also can be used as the AMC source, which depends on the application of this method. SO_2/compressed air mixtures at different conditions in Table 2-2 were prepared by the toxic-gas test system at the institute of energy and environmental technology (IUTA) (blue dashed-line box). The compressed air, which was used as a carrier gas, was purified by a combination of commercial HEPA and activated carbon (AC) filters before entering the system and then was conditioned at 50±5 % RH and 23±2 °C using the embedded humidifier of the system. Next, the purified and humidified air was mixed with 200 ppm SO_2/N_2 (blended by Air Liquide) from a compressed gas cylinder and introduced to the GAC packed bed holder. Two different GACs provided by a filter company were pre-conditioned in a climate chamber at 50±5 % RH and 23±2 °C over 48 hours before all tests to avoid RH effects on the filtration performance, and then mounted into the GAC holder with a diameter of 50 mm. The SO_2/compressed air mixtures downstream of the GAC holder were sampled and analyzed by the soft X-ray assisted detection method (red straight-line box). When the number concentrations of generated particles were higher than the detection limit (3×10^5 #/cm^3) of the UCPC, a rotating disc thermodiluter (TSI model 379021) was used to dilute the particle concentrations before the UCPC. Simultaneously, SO_2 concentrations ([SO_2]) of all gas mixtures were measured by an ambient SO_2 monitor

(HORIBA, APSA-370), which had a lower detection limit of 1 ppb. The measured [SO_2] reduced through adsorption by the GACs were compared to the concentration of generated nanoparticles.

The residence time in the conversion chamber can be changed by the gas volume flow rate in the chamber and is one of important factors for the particle formation (Christensen et al. 1994; Kim et al. 1998; Yun et al. 2009). With the same chamber geometry, the bulk residence time can be determined as the ratio of the volume of the chamber to the volume flow rate of the carrier gas. In other words, the bulk residence time increases with the inverse of the gas volume flow rate. Longer residence time means more time for the particle formation, such as nucleation and growth by condensation and collision in the conversion chamber, thus changing the size distribution of generated particles. In this study, the pressure in the GAC holder of the toxic-gas test system was controlled at slightly lower than the ambient pressure for the safety issue caused by the leakage of tested toxic gases. Therefore, the gas volume flow rate was determined only by the vacuum pumping speed (1.5 lpm) of the UCPC and the SMPS to sample gas mixtures. During all measurements, the bulk residence time was fixed at 100 s. In addition, the particle formation was not influenced by the residence time.

Baseline tests using gas mixtures with different carrier gases

Due to the high ionization energy of the soft X-ray, particles can be formed from the intrinsic contaminants of the carrier gases in addition to the input AMCs (Yun et al. 2009). The unwanted particle formation from the carrier gases, defined as baseline particles in the present work, was investigated before the feasibility study. For testing the effect of

the baseline particles on the particle generation from AMCs, three gas mixtures were prepared at 50 ppb [SO_2] with different carrier gases such as N_2 (Air Liquide, N50), synthetic air (Air Liquide, Alphagaz) and compressed air (by a house compressor) as shown in Table 2-1. In this study, the relative humidity (RH) and temperature of all gas mixtures were 50±5 % RH and 23±2 °C, respectively. The RH for the gas mixtures with N_2 and synthetic air was conditioned using a homemade humidifier and that for compressed air was conditioned using the embedded humidifier in the toxic-gas test system at IUTA.

Table 2-1. Baseline particle concentrations (0 ppb SO_2) and net particles concentrations generated from SO_2 (50 ppb SO_2) with different carrier gases at 1.5 lpm, 50±5 % RH and 23±2 °C

Carrier gas species	SO_2 concentration (ppb)	Particle number concentration (#/cm^3)	Particle volume concentration (nm^3/cm^3)
N_2	0	$2.75 \times 10^5 \pm 5.3 \times 10^4$	$6.3 \times 10^7 \pm 3.5 \times 10^7$
	50	$3.92 \times 10^6 \pm 3.84 \times 10^5$	$3.76 \times 10^9 \pm 3.49 \times 10^8$
Synthetic air	0	$9.43 \times 10^5 \pm 4.77 \times 10^5$	$3.06 \times 10^8 \pm 2.22 \times 10^8$
	50	$2.89 \times 10^6 \pm 4.68 \times 10^5$	$4.26 \times 10^9 \pm 3.18 \times 10^8$
Compressed air	0	$1.65 \times 10^6 \pm 2.5 \times 10^4$	$4.86 \times 10^8 \pm 1.01 \times 10^8$
	50	$3.47 \times 10^6 \pm 1.84 \times 10^5$	$3.71 \times 10^9 \pm 4.07 \times 10^8$

Correlation equations between SO_2 and particle volume concentrations

In addition to the comparison of the measured [SO_2] with the concentrations of generated nanoparticles, the [SO_2] can be compared to those calculated from the particle concentrations using empirical correlation equations between [SO_2] and particle

concentrations. The correlation equations were obtained by calibrating the particle concentrations with the measured [SO_2], which were 1, 2, 5, 10, 20, 50, 100 and 200 ppb, without GACs. Measurements of particle concentrations were repeated in triplicate and results were averaged. When the calculated [SO_2] were in the detection range of the SO_2 monitor, the calculated [SO_2] were checked with [SO_2] measured by the SO_2 monitor. Furthermore, these equations were used to estimate [SO_2] lower than the detection limit of the SO_2 monitor by the extrapolation of them.

2.3 Results and discussion

The effect of baseline particles on the particle formation from SO_2

The test results for the effect of baseline particles are shown in Table 2-1. When only carrier gases (at 0 ppb [SO_2] for each carrier gas in Table 2-1) were introduced to the conversion chamber, nanoparticles were generated under the soft X-ray irradiation. Moreover, the baseline particle concentrations were varied with respect to the species of the carrier gas, which increased from N_2 to compressed air. This implies the total concentration of intrinsic contaminations in carrier gases were different because the hygroscopic conditions of carrier gases were fixed at 50±5 % RH and 23±2 °C. Total particle concentrations at 50 ppb [SO_2] also showed the same order as baseline particle concentrations. However, when net particle concentrations (at 50 ppb [SO_2] for each carrier gas in Table 2), which were determined by subtracting baseline particle concentrations (at 0 ppb [SO_2]) from the total particle concentrations (at 50 ppb [SO_2]), were calculated, all gas mixtures showed more or less concentrations. Based on the results in Table 1, although

baseline particles can be generated from the intrinsic contaminants of the carrier gases and the concentrations of them were different, the effect of baseline particles on the particle formation from the target AMC, SO_2, was not significant. Therefore, the net particle concentrations were used to compare only the concentration of generated nanoparticles from SO_2 during the evaluation tests for GACs, instead of total particle concentrations.

Correlation equations between SO_2 and particle volume concentrations

The net particle number and volume concentrations ($[N_{p,net}]$ and $[V_{p,net}]$, respectively) according to $[SO_2]$ are shown in Figure 2-2a. Interestingly, the correlations of both net particle concentrations according to $[SO_2]$ changed from non-linear to linear relationships over 50 ppb. The non-linearity in the $[SO_2]$ range lower than 50 ppb may come from the complicated reactions for the nanoparticle generations (Kirkby et al. 2011; Berndt 2005). The net number and volume size distributions at different $[SO_2]$ are depicted in Figure 2b and c, respectively. All net number size distributions in Figure 2b had two peaks. The lower mode could only be measured down to the lower detection limit of the SMPS, i.e. 2.5 nm, but obviously had a lower modal diameter, which is one of the peaks of the size distribution. The second broad peak showed modal diameters ranging from 5 to 10 nm for 1 to 200 ppb, respectively. On the other hand, all net volume size distributions in Figure 2-2c showed single peaks at 25 nm because smaller size nanoparticles have a negligible contribution to particle volume concentrations. The increasing modal diameter of the second broad peak in Figure 2-2b shows that nucleation and condensation (i.e. particle growth) occurred simultaneously in the conversion chamber. However, $[N_{p,net}]$, which was obtained by integrating each net number size distribution, on the left axis in Fig

2-2a didn't consider the amount of converted gas molecules for the particle growth, thus resulting in inaccurate correlations.. Therefore, correlation equations should be obtained using [$V_{p,net}$] on the right axis in Fig 2-2a for more quantitatively accurate results because [$V_{p,net}$], which was obtained by integrating each net volume size distribution, included both nucleation and condensation processes, which are related to mass balances (Sato et al. 2007) between gas molecules and nanoparticles through the gas-to-particle conversion. If the exact density of measured nanoparticles is given, particle mass concentrations can be used instead of particle volume concentrations.

Due to the change of linearity between [SO_2] (in ppb) and [$V_{p,net}$] (in nm^3/cm^3), the difference between the measured and calculated [SO_2] increased as [SO_2] increased when we tried to fit the measured results in a single equation. Therefore, two empirical correlation equations were obtained by curve-fitting mean of [$V_{p,net}$] in the non-linear and linear regions as shown in Figure 2-2d, with R^2, higher than 0.99.

$$[SO_2] = 4.452 \times 10^{-10}[V_{p,net}] - 7.162 \times 10^{-19}[V_{p,net}]^2 + 1.006 \times 10^{-27}[V_{p,net}]^3 \quad [1]$$

$$[SO_2] = -123.37 + 4.68 \times 10^{-8}[V_{p,net}] \quad [2]$$

[SO_2] according to [$V_{p,net}$] less than 5×10^9 nm^3/cm^3 (corresponding to 100 ppb [SO_2]) were calculated using equation (1). For [$V_{p,net}$] over 5×10^9 nm^3/cm^3, equation (2) was used to calculate [SO_2]. Because there were no calibration data for [SO_2] at ppt-levels, equation (1) was extrapolated to estimate unknown [SO_2] at ppt-levels from [$V_{p,net}$].

a) b)

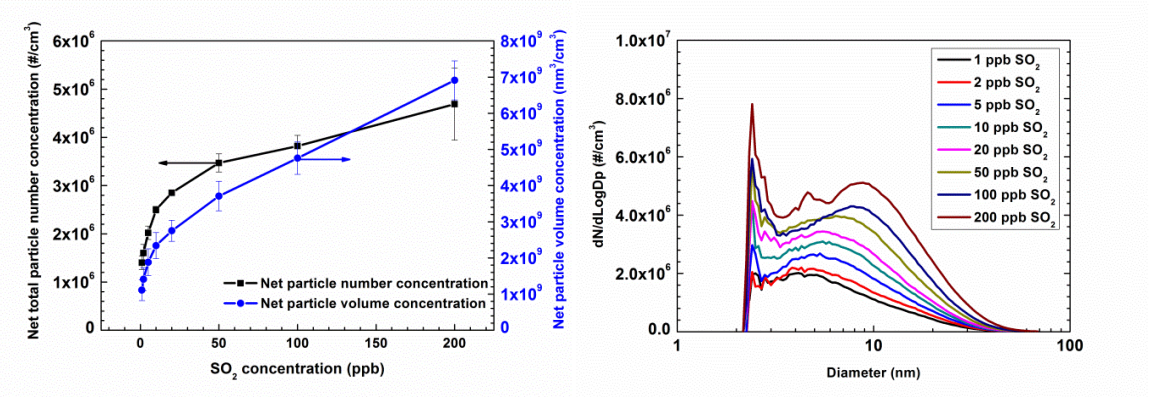

c) d)

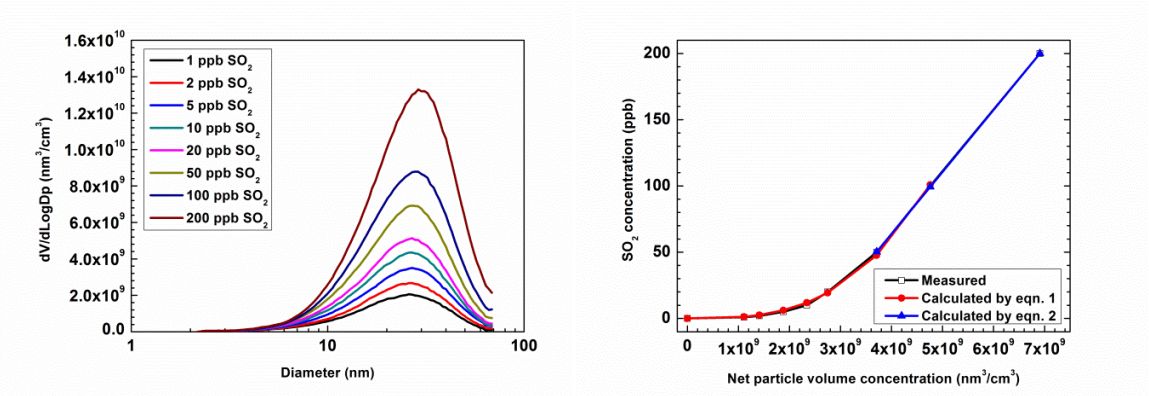

Figure 2-2. (a) Net particle number (black square with solid line) and volume (blue circle with solid line) concentrations, (b) number size distributions and (c) volume size distributions according to SO_2 concentrations from 1 to 200 ppb and (d) SO_2 concentrations measured by the SO_2 monitor (black open circle with solid line) and calculated using the correlation equation (1) and (2) (red circle and blue triangle with solid lines)

Evaluation of the performance of GACs to SO_2 using the soft X-ray assisted AMC detection method

Results for the evaluation tests of the GACs using the detection method and correlation equations at the first condition in Table 2-2 are shown in Figure 2-3. At the condition to accelerate breakthrough of the GACs with 5 mm height and 10 ppm inlet [SO_2], [$V_{p,net}$] for both GACs increased quickly within only 1 hour as shown in Figure 2-3a and [SO_2] calculated using both equation (1) and (2) from [$V_{p,net}$] in Figure 2-3a were over 300 ppb after 1 hour as shown in Figure 2-3b. Because both calculated [SO_2] in Figure 2-3b were in the detection range of the SO_2 monitor, they were compared to [SO_2] measured in parallel by the SO_2 monitor as shown in Figure 3c and d for the GAC A and B, respectively. In Figure 2-3c and d, the calculated [SO_2] and measured [SO_2] were well-matched with each other at ppb-levels. From these results, the soft X-ray assisted detection method combined with the correlation equations was validated to evaluate GACs, at least at ppb-levels. As shown in Figure 2-3a, the GAC A showed higher [$V_{p,net}$] than the GAC B during the whole measurement. This shows that the GAC B had better filtration performance than the GAC A.

Table 2-2. Conditions of the GAC evaluation tests at 50±5 % RH and 23±2 °C (face velocity was calculated as the ratio of the volume flow rate of each gas mixture to the area of GACs with 50 mm ID)

No.	Face velocity (m/s)	Inlet SO_2 concentration (ppm)	Height of GACs (mm)
1	0.33	10	5
2	0.2	10	20
3	0.9	1	20

a) b)

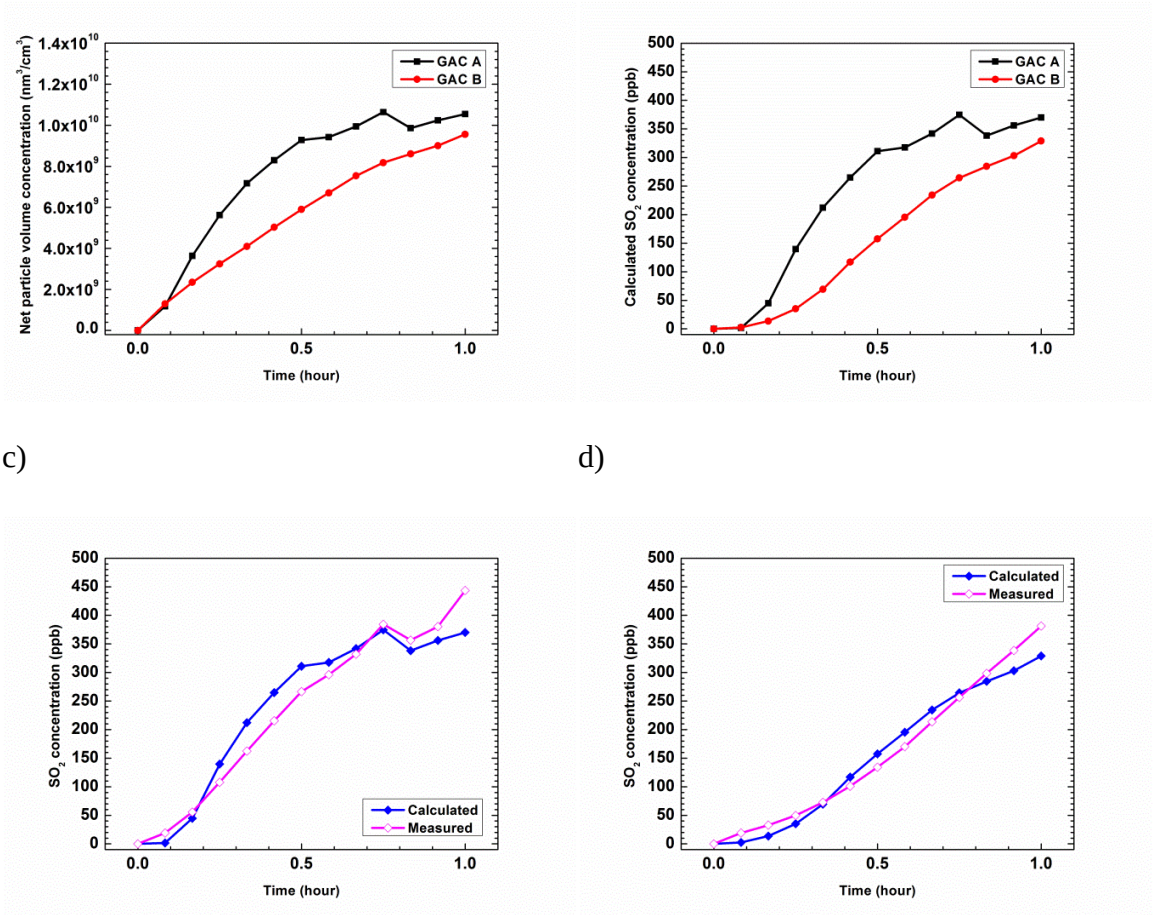

Figure 2-3. Results of evaluation tests during 1 hour at the first condition in Table 2-2: (a) net particle volume concentrations and (b) calculated SO_2 concentrations for the GAC A and B (black square and red circle with solid lines); comparison of the measured (magenta diamond with solid line) and the calculated (blue diamond with solid line) SO_2 concentrations for (c) the GAC A and (b) the GAC B

At the second evaluation condition in Table 2-2 to investigate the sensitivity of this method by increasing the height of GACs to 20 mm, $[V_{p,net}]$ for the GAC A decreased

drastically and was saturated after 2 hours as shown in Figure 2-4a. Because the final [SO_2] for the GAC A, which was converted from the final [$V_{p,net}$] in Figure 2-4a using equation (1), approached to around 1 ppb, the detection limit of the SO_2 monitor, as shown in Figure 4b, the SO_2 monitor was not applicable to measure directly [SO_2] at this condition. Therefore, all [SO_2] were calculated by extrapolating equation (1). For the GAC B, [$V_{p,net}$] was three times lower than that for the GAC A after 2 hours as shown in Figure 2-4a. Furthermore, the highest [SO_2] calculated by extrapolating equation (1) in Figure 2-4b was around 120 ppt. Although all calculated [SO_2] were not quantitatively exact due to the extrapolation of equation (1), the filtration performance of the two GACs can be distinguished qualitatively by this detection method, which is highly sensitive to SO_2, down to ppt-levels. Also, at this condition, the GAC B showed lower [$V_{p,net}$] than the GAC A, which means better filtration performance of the GAC B.

To check the detection sensitivity of this method further, the inlet [SO_2] decreased to 1 ppm (see the last condition in Table 2-2). As shown in Figure 2-4c, the GAC A showed [$V_{p,net}$] than the GAC B during the whole measurement. Because all [SO_2] downstream of the GACs were lower than 1 ppb, [SO_2] of both GACs in Figure 2-4d were also only calculated by extrapolating equation (1) from [$V_{p,net}$] in Figure 2-4c and the maximum concentrations were 100 ppt and 60 ppt for the GAC A and B, respectively. The decrease of [SO_2] after around 2 hours might be caused by the shift of the adsorption layer of both GACs for the SO_2 gas molecules. The filtration performance of the two GACs can be distinguished qualitatively by this detection method again with high sensitivity to SO_2, down to ppt-levels. For all evaluation conditions, the relative filtration performance

between the two GACs was consistent, i.e. the GAC B was better than the GAC A as shown in Figure 2-3 and 2-4. This means that the novel detection method using soft X-ray is valuable to evaluate AMC filters as well as to detect SO_2 at extremely low concentrations, ppt-levels.

Although this detection method is highly sensitive to gaseous components, it is limited to materials available for gas-to-particle conversion. Also, it needs further study or additional analyzers (Katz et al. 2000) to distinguish different gas compounds from their mixtures. However, this soft X-ray assisted detection method can work as faster and easier method to control the cleanroom air quality by evaluating the installed filter media and detecting highly contaminated areas as a monitor. Especially, this method can be applied where highly sensitive and/or fast detection methods are required, e.g., in evaluating performance of adsorbent materials at ultra-low gas concentrations.

a) b)

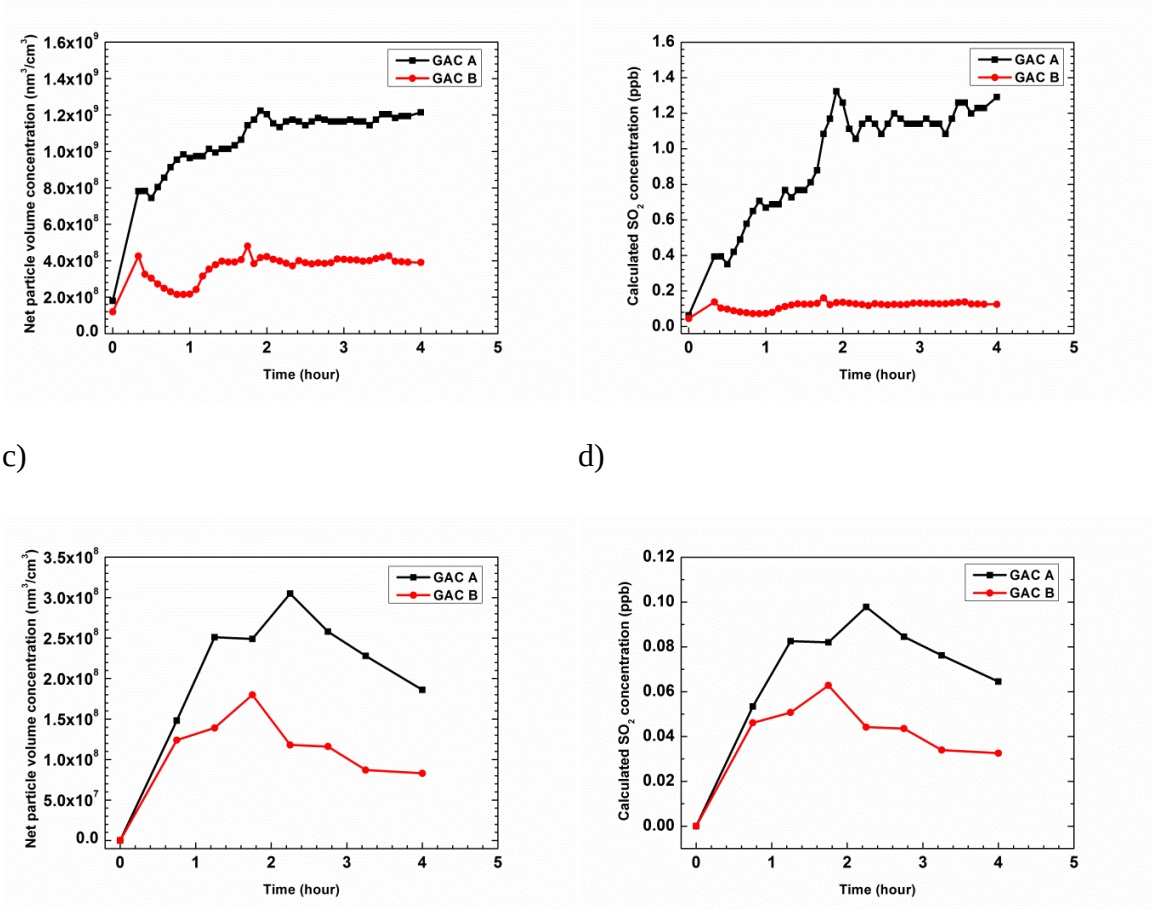

c) d)

Figure 2-4. Results of evaluation tests for the GAC A and B (black square and red circle with solid lines) during 4 hours: (a) net particle volume concentrations and (b) calculated SO_2 concentrations at the second condition in Table 2; (c) net particle volume concentrations and (b) calculated SO_2 concentrations at the last condition in Table 2-2

2.4 Summary

In this study, the novel detection method for AMCs using soft X-ray assisted gas-to-particle conversion was developed as an on-line, economical and highly sensitive detector. The feasibility study of this method was conducted through the evaluation tests for two GACs with SO_2. The filtration performance of the GACs was determined in terms of particle volume concentrations, which were generated from the gas mixtures downstream of the GAC holder in the conversion chamber under the soft X-ray irradiation. The results at different evaluation conditions showed a consistent relative performance between the two GACs. When $[V_{p,net}]$ were converted into $[SO_2]$ using the empirical correlation equations, the calculated gas concentrations showed good agreement at ppb-levels. In addition, the correlation equation (1) was extrapolated to gas concentrations below those measurable by the commercial gas analyzer and the results showed the remarkable sensitivity of this detection method for SO_2, down to ppt-levels. Although the results at ppt-levels were not quantitatively exact due to the lack of calibration data by a SO_2 monitor, the results qualitatively agreed well with the results from measurements at higher concentrations. However, further research is needed to validate the extrapolated equation. This method is also expected to detect diverse AMCs such as aromatic organics, which can be converted into nanoparticles through gas-to-particle conversion, in addition to an inorganic AMC, SO_2.

Chapter 3: Real-time and On-line Screening Method for Materials Emitting Volatile Organic Compounds (VOCs)

3.1 Introduction

In the semiconductor manufacturing industry, managing the concentration of nanoparticles in cleanrooms is an important issue for increasing yields of semiconductor products, because the nanoparticles deposited on silicon wafers and photomasks create defects on the semiconductor products. To prevent nanoparticles from entering semiconductor manufacturing processes, outdoor air is purified by aerosol filtration systems including high-efficiency and ultra-low particulate air (HEPA and ULPA) filters (Donovan 1990; Kim et al. 2007). Even though the particle-free air is introduced in cleanrooms, a new contamination issue known as airborne molecular contamination (AMC) originates from gaseous contaminants in the particle-free cleanroom air during the semiconductor manufacturing processes (Kim et al. 2015). As shorter wavelength ultraviolet (UV) lights (e.g. excimer laser and extreme UV) are used in the advanced lithography techniques, nanoparticles and haze can be formed from AMC under the UV irradiation, in spite of the ultra-low concentration of AMC such as part per billion (ppb, 10^{-9}) or part per trillion (ppt, 10^{-12}).

To remove AMC from the outdoor air, gas filtration systems are also installed next to the aerosol systems. For the gas filtration, granular activated carbons (GACs) are widely used due to their pores. The pores of GACs increase the specific surface area of GACs, which works as capturing sites for gas contaminants through adsorption. (Bansal and Goyal

2005; Kim et al. 2015; Kim and Pui 2015). To enhance the gas filtration efficiency of GACs, the surface of GACs is modified by adding counter chemicals or catalysts (Chen et al. 2003; Chingombe et al. 2005; Weineck et al. 2010). However, the complexity and diversity of the chemical nature of the gaseous contaminants require multiple gas filter layers, thus increasing the maintenance costs (Lobert et al. 2010). Even though AMC in the outdoor air is controlled by the gas filtration systems before entering cleanrooms, AMC can exist in the cleanroom air due to materials used in cleanrooms such as organic solvents and cleanroom construction materials (e.g. adhesives, flame retardants and sealants) (Dallas et al. 2002). The organic solvents and construction materials emit different kinds of volatile organic compounds (VOCs) to the cleanroom air. As organic AMC, VOCs become sources of unwanted nanoparticle and haze formation during photolithography processes. Moreover, some of VOCs are known as carcinogens (Billet et al. 2008) and should be well controlled to avoid adverse health effects on working personnel in cleanrooms (Hakim et al. 2012). Therefore, many efforts have been made to reduce the contamination problems caused by VOCs in the semiconductor industry through developing low-VOC materials for cleanroom-use.

Conventionally, X-ray photoelectron spectroscopy (XPS), time-flight secondary ion mass spectrometry (TOF-SIMS), thermal desorption-gas chromatography-mass spectrometry (TD-GC-MS) and proton transfer reaction-mass spectrometry (PTR-MS) (Licciardello et al. 1986; Schueler 1992; Den et al. 2006; Blake et al. 2009) have been used to measure the concentration of VOCs and to analyze their chemical characteristics. However, these conventional methods are inefficient for frequent measurements to find

candidate low-VOC materials for cleanroom-use, since the conventional instruments require complicated conditions for operating them (e.g. high-vacuum and regent gases) and have time consuming processes for sampling gas contaminants using adsorbents and extracting the contaminants from the adsorbents (Veillerot et al. 2003; Kang et al. 2005). Therefore, choosing candidates roughly by screening materials in the early stage can save time and costs to develop new replacements that emit low VOCs. In the early stage of the screening, measuring total VOC (TVOC) concentration is also more practical than analyzing the composition of VOCs by the conventional instruments due to the wide range of species of VOCs (Barro et al. 2009).

In the present work, we propose and demonstrate a novel screening method for VOCs emitted from materials. This screening method can measure the real-time concentration of VOCs concentration by converting the VOCs into nanoparticles under soft X-ray (namely soft X-ray radiolysis) and measuring the converted nanoparticles through commercial aerosol instruments. This on-line method does not require sampling processes using adsorbents. First, this method was applied to measure VOCs emitted from different kinds of organic solvents and adhesives (i.e. Super Glue (SG) and cleanroom-use adhesives). Subsequently, the TVOC level of the cleanroom-use adhesives was measured by this method and compared with the TVOC level measured by TD-GC-MS. By using this method to screen materials, we can save time and focus on investigating the screened candidate materials precisely using the conventional analysis methods such as TD-GC-MS.

3.2 Materials and methods

Figure 3-1 shows a schematic diagram of the screening method for measuring VOCs through the soft X-ray radiolysis. VOCs emitted from materials in the VOC chamber were carried by nitrogen (N_2, UHP grade) and introduced into the soft X-ray radiolysis chamber. The carrier gas, N_2, passed through the metal filter and activated carbon filter to eliminate its intrinsic contaminants (e.g. particulate and gaseous contaminants as well as water vapors) before carrying VOCs. The VOC chamber was made of stainless steel to control the concentration of VOCs by heating the chamber with a hot plate. The soft X-ray radiolysis chamber was also made of stainless steel to remove contaminants adsorbed on the chamber wall by heating the chamber. Both VOC and soft X-ray chambers have a same dimension of ϕ 127 x 203 mm (ϕ 5 x 8 in.), which corresponds to the bulk residence time, 100 s at 1.5 litter per minute (lpm). In the soft X-ray radiolysis chamber, nanoparticles were generated from VOCs under the soft X-ray irradiation. The nanoparticles generated from VOCs through the soft X-ray radiolysis were collected on a copper grid using a nanometer aerosol sampler (TSI model 3089, TSI Inc.) for analyzing the shape of the particles by a transmission electron microscopy (TEM, Tecnai T12, FEI company). The TEM image in Figure 3-1 shows the nanoparticles generated from VOCs. The number distribution of the generated nanoparticles was measured from 6 to 228 nm by a scanning mobility particle sizer (SMPS, TSI model 3938L76, TSI Inc.), which consists of a differential mobility analyzer and an ultrafine condensation particle counter (DMA and UCPC, TSI model 3081 and 3776, TSI Inc.). The volume distribution of the nanoparticles was obtained from the number distribution by assuming the generated nanoparticles as

spherical, as shown in the TEM image in Figure 3-1. By integrating the measured number distribution and the calculated volume distribution, the total particle number and volume concentrations (N_p and V_p) were determined. When the number concentration of the generated nanoparticles was too low to be measured by the SMPS (McMurry 2000), the UCPC was used to determine N_p instead of the SMPS. However, V_p cannot be estimated by the UCPC due to the lack of the information about the particle size. Because this screening method could not analyze the composition of VOCs from materials, the N_p and V_p were considered as TVOC of the evaluated materials.

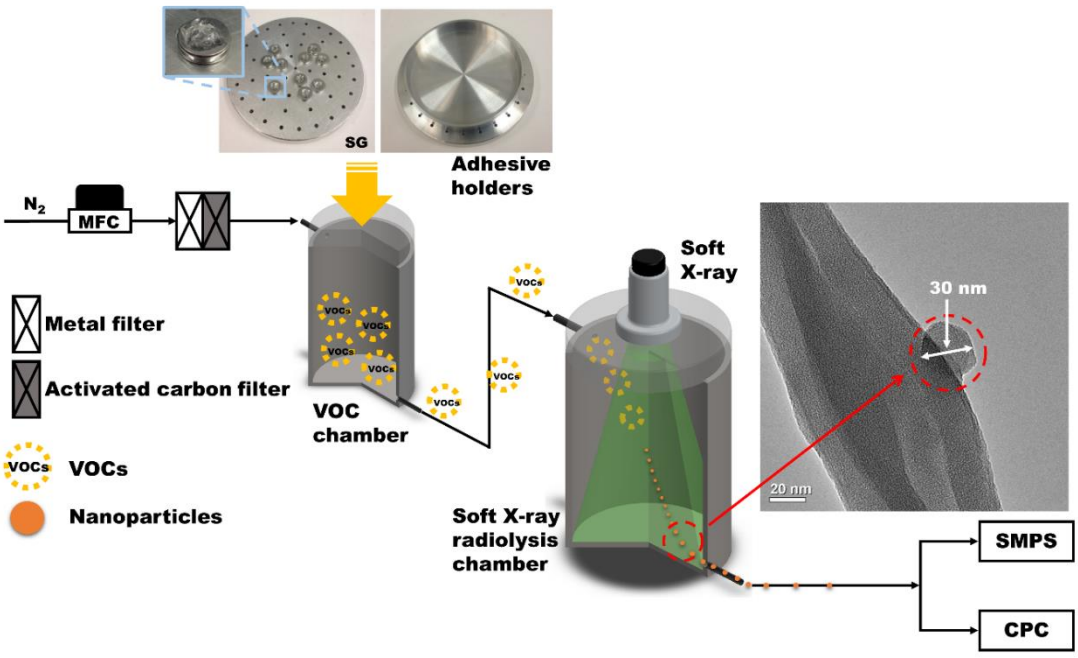

Figure 3-1. Schematic diagram of the screening method for volatile organic compounds (VOCs) via soft X-ray radiolysis. The inserted transmission electron microscopy (TEM) image next to the soft X-ray radiolysis chamber represents an example of the nanoparticles generated in the chamber. Two adhesive holders shown above the VOC chamber were prepared for different kinds of VOC-materials, e.g. gel-type super glue (SG) (small holder, left) and cleanroom-use adhesives (large holder, right).

This screening method was applied first to detect VOCs from organic solvents. Table 3-1 lists the organic solvents used for the feasibility test, which were aromatic and aliphatic compounds as well as alcohols (Sigma-Aldrich, Co., Acros organics and Mallinckrodt Chemicals). Each organic solvent was contained in a pyrex petri dish (50 mm ID, Corning Inc.) and put into the VOC chamber. VOC, evaporated organic solvent, was then delivered to the soft X-ray radiolysis chamber by N_2 as the carrier gas. N_p of the nanoparticles generated from the VOC in the radiolysis chamber was measured by the UCPC.

Table 3-1. Organic solvents used for the VOC measurements by the screening method via soft X-ray radiolysis and the measured VOCs from the organic solvents in terms of the particle number concentration (N_p) by an ultrafine condensation particle counter (UCPC)

Category	Name	Formula	N_p (#/cm^3)
Aliphatic compounds	Hexane	C_6H_{14}	Not detected
	Octane	C_8H_{18}	
	Decane	$C_{10}H_{22}$	
	Dodecane	$C_{12}H_{26}$	
	Tetradecane	$C_{14}H_{30}$	
	Hexadecane	$C_{16}H_{34}$	
	Cyclohexane	C_6H_{12}	
Aromatic compounds	Benzene	C_6H_6	$> 3 \times 10^5$
	Toluene	C_7H_8	$2.14 \times 10^5 \pm 2.04 \times 10^4$
Alcohols	Methanol	CH_3OH	Not detected
	Ethanol	C_2H_5OH	
	IPA	C_3H_7OH	
	Butanol	C_4H_9OH	
	2-Hexanol	$C_6H_{13}OH$	
	3-Hexanol	$C_6H_{13}OH$	
	1-Octanol	$C_8H_{18}O$	$3.36 \times 10^4 \pm 7.83 \times 10^3$
	Cyclohexanol	$C_6H_{12}O$	$2.81 \times 10^4 \pm 3.29 \times 10^3$
	Cyclooctanol	$C_8H_{16}O$	$> 3 \times 10^5$

Figure 3-1 also shows two kinds of holders for measuring VOCs from two different types of adhesives (gel-type SG and solid cleanroom-use adhesives). Gel-type SG was sampled on the small commercial aluminum holder (15363-1, TED Pellar, Inc.). The unit of the SG sample on the small holder had a hemispherical shape and its mass was 0.1 g. The total mass of the SG sample in the VOC chamber was controlled by changing the number of the unit SG sample. The unit SG samples were mounted on the disc through holes and put into the VOC chamber. VOCs from the SG sample were measured by the screening method at different conditions such as mass (0.1, 0.2, 0.5 and 1 g), heating temperature for the VOC chamber (23, 50 and 100 °C), N_2 flow rate (1.5, 3.0, 4.5 and 6 lpm), and curing time (1, 2, 3, 5, 15 and 30 days), as depicted in Figure 3-2 and 3-3. The insert in Figure 3-3c shows the change of mass during curing SG up to 30 days. The reference condition for the evaluations of VOCs from SG were 1.0 g, 23 °C and 1.5 lpm for the mass, heating temperature and N_2 flow rate, respectively.

For measuring VOCs from the cleanroom-use adhesives (A, B, C and D, H.B. Fuller Company), the adhesives, which were solid-state at room temperature, were prepared as pieces with size of about 5x5 mm. The samples were contained on the large circular holder and put into the VOC chamber, as shown in Figure 3-1. Due to the low VOC level of the cleanroom-use adhesives, the VOC level of the cleanroom-use adhesives were also measured at conditions for higher concentration of VOCs by changing the mass (1 to 10 g) and the heating temperature (23 to 50 °C and 100 °C) after measuring VOCs at the reference condition.

The TVOC of the cleanroom-use adhesives was also analyzed by TD-GC-MS to validate the results measured by this screening method. The TD-GC-MS consists of a GC-MS (6890 GC-5973 MS, Agilent technologies) with a thermal desorption unit/cooled injection system (TDU/CIS, Gerstel Inc.). The TD-GC-MS was calibrated using toluene as a standard. Each cleanroom-use adhesive was prepared at 30±3 mg, and VOCs from the adhesives were collected on tenax TA liners using the auto sampler in the TDU/CIS. Then, the TVOC of the trapped VOCs on the tenax TA liners was measured by increasing the oven temperature of the GC-MS from 40 to 280 °C.

3.3 Results and discussion

Table 3-1 shows the N_p generated from the VOCs of the organic solvents in the soft X-ray radiolysis chamber, which was measured by this screening method. Through the measurements, the aromatic compounds, such as benzene and toluene, produced a lot of nanoparticles through the soft X-ray radiolysis. In addition, the N_p for the benzene exceeded the upper detection limit of the UCPC, $3x10^{-5}$ #/cm^3. Although the mechanism for the formation of nanoparticles from VOCs through the soft X-ray radiolysis is similar to the mechanism for the formation of secondary organic aerosols under the sun light in nature, this screening method did not require adding seed aerosols and nitric oxides (NO_x) for the nanoparticle formation from the aromatic compounds (Keywood et al. 2004; Sato et al. 2007; Kim et al. 2015). However, the aliphatic compounds (saturated hydrocarbons) showed much less reactivity than the aromatic compounds (unsaturated hydrocarbons), resulting in no particle detection using this screening method at the reference condition.

The aliphatic compounds may need nitrogen oxides (e.g. NO_x) or seed aerosols (e.g. ammonium sulfate) to form nanoparticles as secondary organic aerosols (SOAs) during the soft X-ray radiolysis (Pitts et al. 1978; Atkinson 2000). In addition, VOCs of the aliphatic compounds may be detected by this method if instruments with size detection limit (d_{50}) smaller than that of the UCPC (d_{50}=2.5 nm) are available to detect sub-2 nm particles generated in the radiolysis chamber (Jiang et al. 2011). For this study, the reference condition for the flow rate was set at 1.5 lpm. If the flow rate in the soft X-ray radiolysis chamber decreases in order to increase the reaction time for the nanoparticle generation, the aliphatic compounds may also be detected by this screening method.

VOCs from alcohols, such as 1-Octanol, cyclohexanol and cyclooctanol, were also detected by this screening method. Even though 1-octanol has a chain structure as aliphatic compounds do, the hydroxyl (OH) group attached to the chain structure may contribute to the particle generation under soft X-ray irradiation by making OH radicals (Sato et al. 2007). The hydroxyl group also participated in the reactions for the nanoparticle generation from cyclohexanol and cyclooctanol via soft X-ray radiolysis. Moreover, cyclooctanol showed a rapid particle generation, the concentration of which exceeded the upper detection limit of the UCPC.

Figure 3-2 shows the N_p and V_p of the nanoparticles generated from VOCs of SG, which were measured by this soft X-ray assisted screening method, at different conditions such as mass, temperature, carrier gas (N_2) flow rate, and curing time. Both N_p and V_p increased with the mass of SG and the heating temperature of the VOC chamber, as shown in Figure 3-2a and b, because the concentration of VOCs increased at more mass and higher

temperature conditions. In addition, the measured N_p (or V_p) increased linearly according to the mass of SG. This implies that the concentration of VOCs from adhesives can be controlled by increasing their mass. Moreover, the relative concentration of VOCs can be estimated based on the measured N_p (or V_p). The residence time in the soft X-ray radiolysis chamber (i.e. the time exposed to the soft X-ray) is also an important parameter of the nanoparticle formation.

When the flow rate of N_2 increased to reduce the reaction time in the radiolysis chamber (i.e. the time exposed to the soft X-ray), N_p also increased as shown in Figure 3-2c. This phenomenon was different from general particle formation according to the reaction time (Christensen et al. 1994). To figure out the reason for this phenomenon, number and volume distributions of the generated nanoparticles were analyzed simultaneously. For the number distribution as shown in Figure 3-3a, the magnitude of the second (larger size) peak at around 50 nm decreased with the flow rate from 1.5 to 6.0 lpm, but that of the first (smaller) peak at around 11 nm increased. The size of the first peak also increased slightly to 13 nm as shown in the insert in Figure 3-3a. On the contrary, the volume distribution had a single peak (See Figure 3-3b) and the magnitude and size of the sole peak decreased dramatically with the flow rate. The results showed that the growth of nanoparticles by condensation and collision were suppressed with the insufficient reaction time at higher flow rate. Therefore, the magnitude of the volume distribution was diminished, and the V_p decreased as shown in Figure 3-2c, even though the N_p increased. Because the soft X-ray radiolysis is a mass-based conversion process (Kim et al. 2015), using V_p is preferred to N_p for measuring TVOC through this screening method.

Subsequently, the amount of VOCs emitted from SG according to the curing time was also measured using this screening method, as shown in Figure 3-2d. The N_p and V_p decreased during the curing (leaving the SG samples in air) and were lower than the detection limit of the SMPS after 30 days. During the curing, the total mass of the SG samples decreased drastically for the first 5 days (down to 20%), as shown in the insert in Figure 3-3c. Simultaneously, the number and volume distributions of the generated nanoparticles were also changed significantly (see Figure 3-3c and d), thus decreasing the N_p and V_p during this five-day period. After the first 5 days, the mass of the SG samples did not change much, but VOCs of the SG samples were still detected until about the thirtieth day, as shown in Figure 3-2d. In addition, the peak size of the number distribution decreased between the third and fifth days due to low TVOC level. At the low TVOC level, the growth of nanoparticles was suppressed as in the case with higher flow rate (see in Figure 3-3a), thus increasing the magnitude of the number distribution as well as the N_p at the fifth day of the curing. On the contrary, the V_p still continuously decreased at the fifth day because both magnitude and the peak size of the volume distribution continuously decreased (see the insert in Figure 3-3d), even though the volume distribution of the generated nanoparticles was also changed significantly, as shown in Figure 3-3d. This phenomenon also implies that comparing V_p is more reliable than N_p to evaluate TVOC by this screening method. Based on the results, adhesives such as SG cannot be used in cleanrooms, where the standard of the air quality is very strict, and the VOCs from adhesives should be carefully monitored, even though they are already polymerized in air.

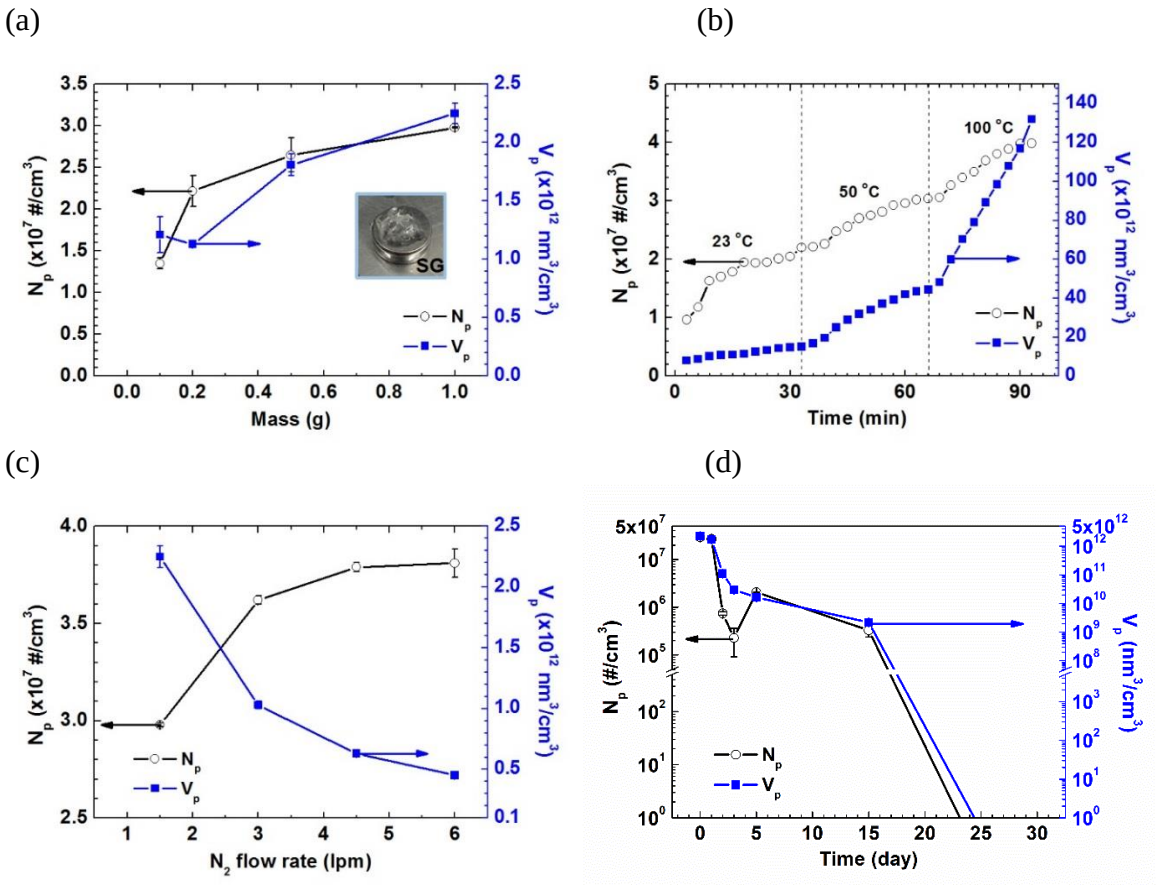

Figure 3-2. Total particle number and volume concentrations (N_p and V_p) generated from VOCs of SG through the VOC screening method via soft X-ray radiolysis at different (a) masses (0.1, 0.2, 0.5 and 1.0 g), (b) temperatures (23, 50 and 100 °C), (c) N_2 flow rates (1.5, 3.0, 4.5 and 6.0 lpm), and (d) curing times (0, 1, 2, 3, 5, 15 and 30 days) (black open circle: N_p, blue solid square: V_p)

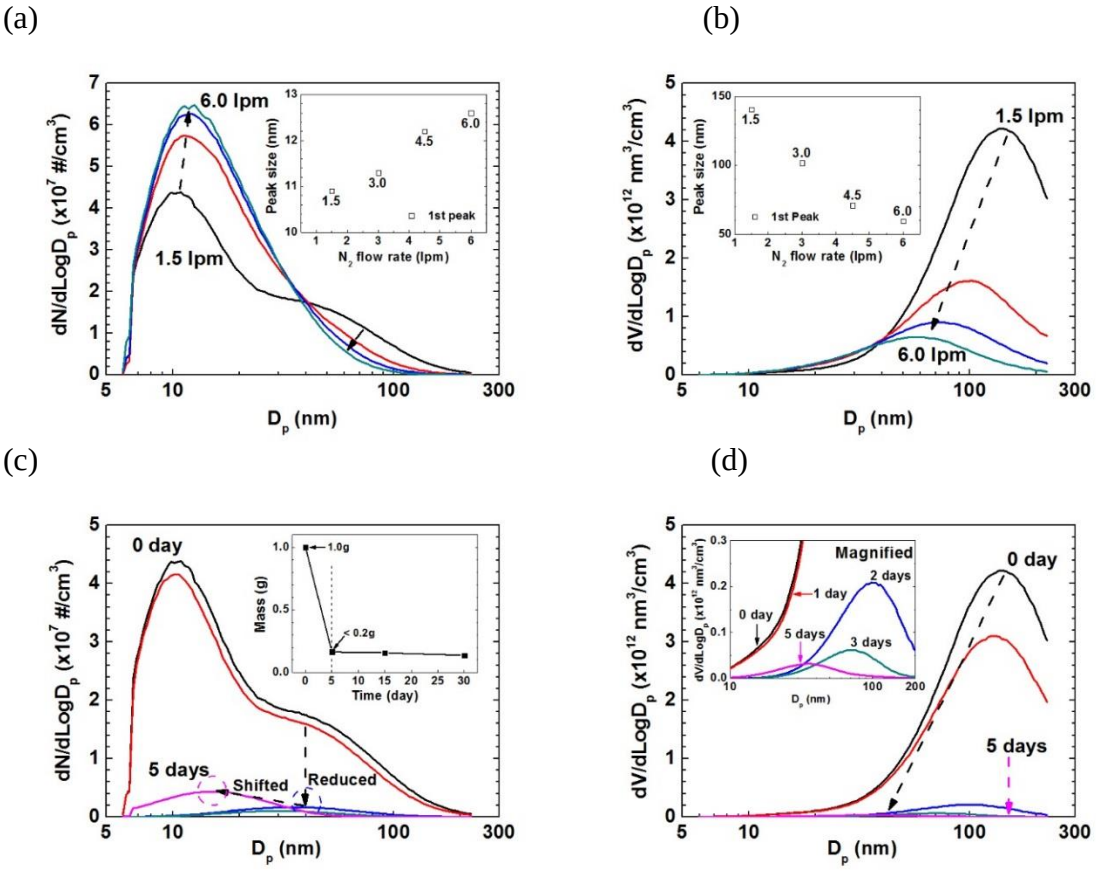

Figure 3-3. (a) Number and (b) volume distributions at different N_2 flow rates, and (c) number and (d) volume distributions at different curing times for nanoparticles generated from VOCs of SG through the screening method via soft X-ray radiolysis. The inserts in (a) and (b) show the change of the peak size at different N_2 flow rates. The insert in (c) provides the change of the mass of SG samples according to the curing time up to 30 days. The insert in (d) represents the magnified distributions.

Due to the strict standard for the air quality in cleanrooms (Sematech International 2011), materials used in cleanrooms including adhesives should be designed for releasing lower VOCs than current materials. This proposed VOC screening method was also applied

to screen the four cleanroom-use adhesives for finding the lowest VOC releasing materials. The TVOC of the four cleanroom-use adhesives was first measured by this screening method at room temperature, as the SG samples were. However, particle generation was not detected at the reference condition by this screening method. To enhance the amount of VOCs, the screening conditions, such as mass and heating temperature, were changed to 10 g and 50 °C, respectively. However, particle generation was also not observed at the changed condition. Because 50 °C is already higher than the real cleanroom condition (21 °C), this result proved that the cleanroom-use adhesives were well-designed for the purpose. By further heating the adhesives at 100 °C, the TVOC of the four cleanroom-use adhesives could be differentiated based on the N_p, as shown in Figure 3-4. Due to the low TVOC level, the UCPC was used instead of the SMPS. Based on the result, the adhesive A released the highest TVOC, followed by D, C and B. The TVOC of the adhesives B and C were more or less based on the N_p measured by this screening method. Figure 3-4 also shows the TVOC for the same cleanroom-use adhesives measured by TD-GC-MS. TD-GC-MS showed the highest TVOC (91 ppm) for the adhesive A and the lowest TVOC (3 ppm) for the adhesive C. Whereas the adhesives A and C showed similar trend between the screening method and TD-GC-MS, the TVOC levels for the adhesives B and D measured by TD-GC-MS were different from those measured by the screening method. The difference might have been caused by the different heating temperatures of the two methods (100 and 40 to 280 °C, respectively). Although the order of TVOC measured by this VOC screening method was not exactly matched with the result measured by TD-GC-MS, the overall trend of TVOC measured by this VOC screening method was comparable

with that by TD-GC-MS. In addition, the results obtained by this VOC screening method at 23 °C can give information of TVOC, which is close to the real cleanroom environment at room temperature.

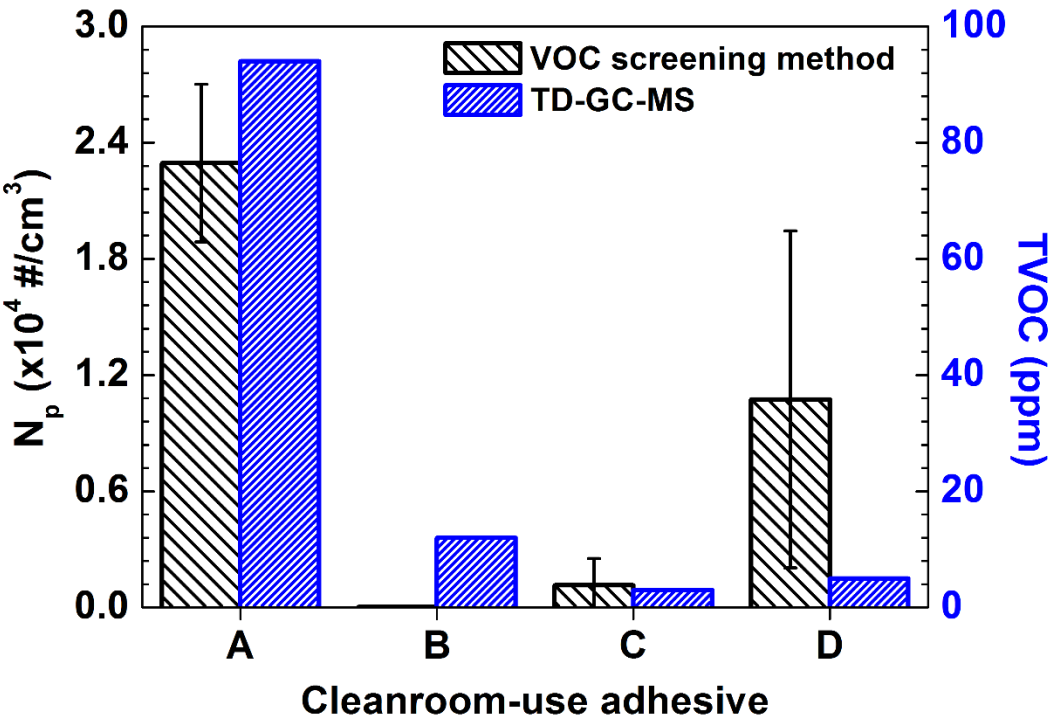

Figure 3-4. Total particle number concentration (N_p) measured by the VOC screening method via soft X-ray radiolysis with the ultra condensation particle counter (UCPC) at 100 °C (left black column) with total VOC (TVOC) concentration analyzed by the thermal desorption-gas chromatography-mass spectrometry (TD-GC-MS) (right blue column)

3.4 Summary

The VOC screening method for materials used in cleanrooms was developed by converting the VOCs into nanoparticles under soft X-ray irradiation. By adding the simple conversion system through the soft X-ray radiolysis, the methods for measuring properties

of aerosols can be extended to measuring VOCs. This method was applied to measure VOCs from different kinds of solvents and adhesives. Moreover, the TVOC of the cleanroom-use adhesives showed a similar trend with the TVOC measured by TD-GC-MS, although the unit of the screening method was different from that of TD-GC-MS. This screening method can be applied to select candidate materials used in cleanrooms utilizing the measured N_p and V_p as TVOC. The saved time and costs by this VOC screening method can help evaluate efficiently the selected low-VOC candidate materials. The composition of the VOCs from the tested adhesives should be analyzed further to improve the reliability of this method. In addition, the conversion of the unit between two methods should be investigated together along with the analysis on the composition of the VOCs.

Chapter 4: Measurement of Outgassing from $PM_{2.5}$ Samples Collected in Xi'an, China through Soft X-Ray-Radiolysis

4.1 Introduction

$PM_{2.5}$ (particulate matter smaller than 2.5 μm in aerodynamic diameter) has been found as a source of various issues on the environment and human health, such as climate change, visibility reduction and respiratory diseases (Cao et al. 2012b; Pui et al. 2014). Many countries, such as China, India and Korea, have suffered the environmental and health problems caused by the airborne pollutants including $PM_{2.5}$ (Menon et al. 2002; Akimoto 2003; Tiwari et al. 2010; Cao et al. 2012a; Park et al. 2013) and are currently struggling to reduce the concentration of $PM_{2.5}$ by removing its origins, e.g. filtering exhaust air from vehicles and industries (Huang et al. 2014; Pui et al. 2014). However, $PM_{2.5}$ is not only emitted from vehicles and industries (primary $PM_{2.5}$) (Pedata et al. 2015), but also synthesized from gas contaminants (e.g. volatile organic compounds and polycyclic aromatic hydrocarbons) in the air through photochemical processes (secondary $PM_{2.5}$), which are also known as secondary organic and inorganic aerosols (SOAs and SIAs) (Jimenez et al. 2009; Fu et al. 2012; Huang et al. 2014; Kim et al. 2015).

In the semiconductor industry, avoiding the particulate air pollutants, $PM_{2.5}$, is critical to enhance the production yield of semiconductor chips because particles deposited on silicon wafers or photo masks in the lithography cause defects of the semiconductor chips. Therefore, particulate filters have been installed in semiconductor manufacturing fab to prevent both primary and secondary $PM_{2.5}$ in the outdoor air from entering the fab and

creating defects on the semiconductor chips(Donovan 1990). However, gaseous contaminants in the outdoor air can penetrate the particle filters and create new contamination problems in the semiconductor manufacturing, i.e., airborne molecular contamination (AMC) (Kim et al. 2015). Even though the cleanroom air is particle-free, AMC in the particle-free air can form nanoparticles and haze on the lenses, photomasks and silicon wafers through photochemical processes under ultraviolet lights in the lithography process, thus increasing the yield loss of the semiconductor chips. To reduce AMC originated from the outdoor air, additional gas filters, such as granular activated carbons (Bansal and Goyal 2005; Kim and Pui 2015; Kim et al. 2016a), have been installed next to the particle filters. In addition, many efforts have been made to replace current materials used in cleanrooms with low-AMC emitting materials for eliminating the sources of AMC (Kim et al. 2016b).

Recently, several semiconductor companies have built their manufacturing facilities in Xi'an, which is one of largest cities in China. However, Xi'an is currently suffering environmental and health problems caused by $PM_{2.5}$, such as the low-visibility and respiratory diseases (Huang et al. 2012; Cao et al. 2012b; Zhu et al. 2015). In addition, the high concentration of $PM_{2.5}$ is detrimental for operating the semiconductor fab in the city, because the particles filters for removing $PM_{2.5}$ in the air should be replaced more frequently than other manufacturing sites in the world. The daily concentration change of the ambient $PM_{2.5}$ (Cao et al. 2009; Dai et al. 2012) also makes the lifetime of the particle filters difficult to estimate. Even though $PM_{2.5}$ is removed by the particle filters, chemicals adsorbed on the collected $PM_{2.5}$ can be outgassed from the particulate contaminants and

then contribute to reduce the lifetime of the gas filters, which are installed next to the particle filters. If no gas filter is installed for the outdoor air or the breakthrough of the gas filters occurs (Bansal and Goyal 2005), the outgassing can pass through the gas filters and enter the semiconductor manufacturing processes, thus causing AMC caused problems, i.e. nanoparticle and haze formation. Although the effect of $PM_{2.5}$ on the environment and human health has been investigated substantially (Cao et al. 2003; Billet et al. 2007; Abbas et al. 2009; Zhu et al. 2014), its effect to the semiconductor industry is still not well-kwon.

Kim et al. developed a detection method for AMC through gas-to-particle conversion assisted by soft X-ray (soft X-ray radiolysis) (Kim et al. 2015; Kim et al. 2016b), which simulated the nanoparticle and haze formation from AMC in the lithography process. By converting the outgassing into nanoparticles and measuring them, the soft X-ray radiolysis method can determine the total concentration of outgassing from $PM_{2.5}$, thus providing the correlation between the outgassing concentration and the mass loading of $PM_{2.5}$ collected on the particle filters. Although the method cannot analyze the composition of outgassing, the outgassing measured by the soft X-ray method is very close to AMC due to the principle of the detection. For the composition of outgassing from $PM_{2.5}$, the chemical analysis methods used for investigating the environmental and human health effects of $PM_{2.5}$, such as thermal/optical reflectance (TOR) method, ion chromatography (IC) and gas chromatography-mass spectrometry (GC-MS) for organic and elemental carbons (OC/EC), water soluble ions and organic compounds, respectively, can be employed. By comparing the results measured by the soft X-ray method with the results

analyzed by the OC/EC and GC-MS, the effect of $PM_{2.5}$ to the semiconductor industry and the changing periods of the particle filters installed in the fab can be estimated.

In this study, the outgassing from $PM_{2.5}$ and the correlation between the outgassing and $PM_{2.5}$ mass loading have been investigated through the soft X-ray radiolysis method. The $PM_{2.5}$ samples were collected at the Institute of Earth Environment, Chinese Academy of Science (IEECAS) in Xi'an, China and shipped to the University of Minnesota (UMN), USA for measuring the outgassing by the soft X-ray method. The chemical analyses of the outgassing from $PM_{2.5}$ collected at the same time was also conducted using the TOR, IC and GC-MS. Based on the results, the correlation between the outgassing and the mass loading of the $PM_{2.5}$ was obtained and compared with the chemical composition of the outgassing.

4.2 Materials and methods

Sampling the $PM_{2.5}$ at IEECAS in Xi'an, China and shipping the samples to UMN, USA

The $PM_{2.5}$ samples used in this study were collected by two $PM_{2.5}$ samplers (TE-Wilbur-2.5, Tisch International, Inc.) at the IEECAS in Xi'an, China. High efficiency particulate air (HEPA) filters made of fiberglass(Kim et al. 2007) were prepared as substrates for collecting $PM_{2.5}$ using the samplers with the sampling flow rate at 16.7 lpm. The diameter (ϕ) of the circular HEPA filters was 47 mm, and $PM_{2.5}$ was collected on the center of the filters with ϕ=37 mm during the sampling. Table 4-1 shows the five mass loading conditions (0.12 – 6.0 mg) of the $PM_{2.5}$ samples in the two different periods (A and

B) for investigating the correlation between the outgassing and the mass loading of $PM_{2.5}$. The sampling time for each $PM_{2.5}$ sample was calculated based on the annual average concentration of the ambient $PM_{2.5}$ in Xi'an, 100 $\mu g/m^3$. However, the actual mass loading of each $PM_{2.5}$ sample was different from its planned mass loading, due to the change of the ambient $PM_{2.5}$ concentrations during the sampling periods. Therefore, the actual mass loading of each $PM_{2.5}$ sample was calculated using the average concentration of the ambient $PM_{2.5}$ for each sampling and used for the data analysis instead of the planned mass loading. The collected $PM_{2.5}$ samples were kept at below -18 $^{\circ}C$ to minimize the outgassing loss of the samples during storage and shipping to UMN, USA.

Table 4-1. Conditions of the $PM_{2.5}$ samples collected at IEECAS in Xi'an, China

Sampling period	No.	Planned $PM_{2.5}$ mass loading (mg)	Ambient $PM_{2.5}$ concentration ($\mu g/m^3$)	Actual $PM_{2.5}$ mass loading (mg)
A	1	0.12	143	0.14
	2	0.6	117.7	0.71
	3	1.2	164	2.13
	4	2.4	151.1	3.78
	5	6.0	60	3.60
B	1	0.12	100	0.15
	2	0.6	50	0.33
	3	1.2	50	0.63
	4	2.4	110	2.64
	5	6.0	140	6.91

Measurements of outgassing from the $PM_{2.5}$ samples at UMN

Figure 4-1 shows the experimental setup for measuring the outgassing of the adsorbed chemicals from the $PM_{2.5}$ samples through soft X-ray radiolysis method (Kim et al. 2015; Kim et al. 2016b). One of the two samples for each mass loading condition was used to measure the outgassing from $PM_{2.5}$ and the other sample was analyzed for the chemical composition of the outgassing. The $PM_{2.5}$ samples were contained in the outgassing chamber, which can be heated up to 200 $^{\circ}$C by a hot plate for accelerating the outgassing process. The outgassing from the $PM_{2.5}$ samples was carried by the nitrogen (N_2, UHP grade, 99.999% purity) and introduced into the soft X-ray radiolysis chamber. The N_2 was purified by the particle and gas filters for removing intrinsic particulate and gaseous contaminants before entering the outgassing chamber. In the radiolysis chamber, the outgassing was converted into nanoparticles through the soft X-ray radiolysis. The particle generation was monitored by the ultrafine condensation particle counter (UCPC, TSI model 3776, TSI Inc.), and the number distribution of the nanoparticles generated in the radiolysis chamber was determined by the scanning mobility particle sizer (SMPS, TSI model 3938L76, TSI Inc.) as shown in Figure 4-3a and c. When the soft X-ray emitter was turned off, no particle generation was observed by the UCPC. From the measured number distribution, the volume distribution was calculated as shown in Figure 3b and d. Then, the total particle number and volume concentration (N_p and V_p) were obtained by integrating the number and volume distribution, respectively and plotted according to the actual mass loading of the $PM_{2.5}$ samples, as shown in Figure 4-4. By curve fitting the N_p and V_p vs. the actual mass loading, the correlations between the outgassing and the actual mass

loading of the $PM_{2.5}$ samples were determined and also shown in Figure 4-4. If the particle number concentration converted from the outgassing was lower than the detection limit of the SMPS(McMurry 2000), the UCPC was used to measure the N_p(Kim et al. 2016b), which can give rough comparisons of the quantified outgassing between the $PM_{2.5}$ samples. The UCPC was also employed to scan the outgassing rapidly and compare the outgassing level roughly, although the N_p was higher than the lower limit of the SMPS. All measurements of the outgassing were repeated thrice for the same sample and averaged.

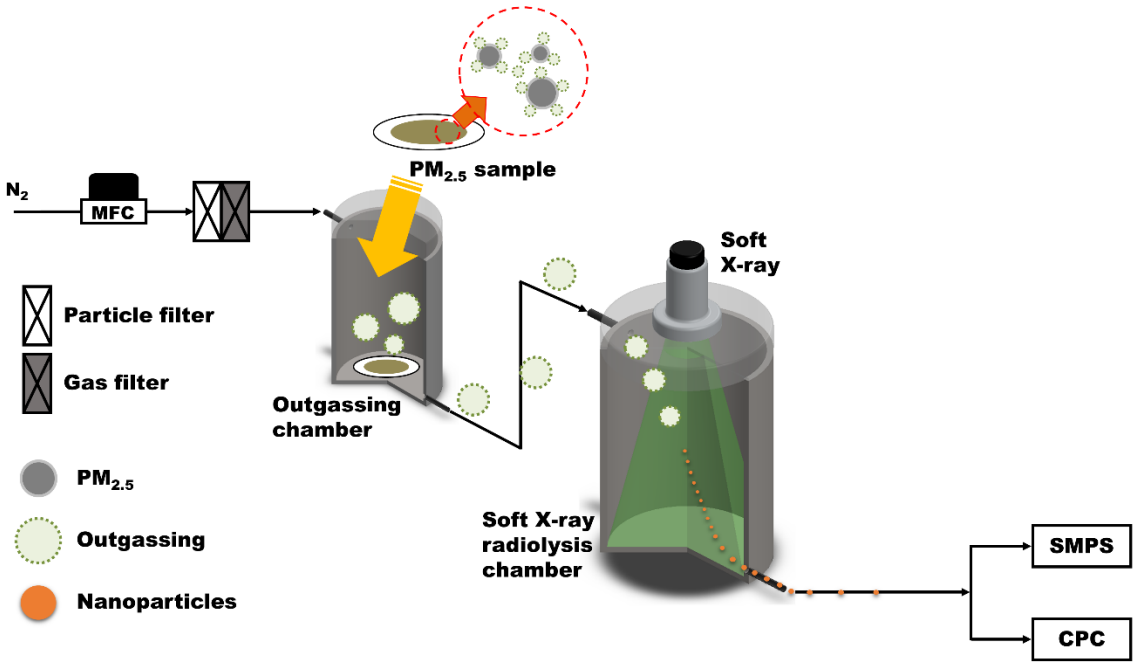

Figure 4-1. Experimental setup for measuring the outgassing from the $PM_{2.5}$ samples

One set of the $PM_{2.5}$ samples collected in the period A (A samples) were evaluated for the feasibility tests of the soft X-ray radiolysis method as quantifying the outgassing from $PM_{2.5}$. During the feasibility tests, the outgassing chamber was heated at 100 ˚C to increase the outgassing from the A samples, and the UCPC was deployed to rapidly scan and compare the N_p of the nanoparticles converted from the outgassing through the soft X-ray radiolysis as shown in Figure 4-2. After the feasibility tests, one set of the $PM_{2.5}$ samples collected in the period B (B samples) were tested at 23 ˚C first and then 100 ˚C to observe the outgassing from the $PM_{2.5}$ samples at the real and severe weather conditions for semiconductor manufacturing facilities. The SMPS measured the size distribution of the nanoparticles generated from the outgassing for the B samples as shown in Figure 4-3.

During the feasibility tests, the A samples were heated at 100 °C for accelerating outgassing, but the condition did not represent the normal situations of the removal of the $PM_{2.5}$ in the semiconductor manufacturing facilities. Therefore, the B samples were tested at 23 °C first, because 23 °C is more close to the real environment of the particle filtration in the semiconductor industry. After the measurement at 23 °C, the B samples were also tested at 100 °C for estimating the outgassing during hot weathers. However, the A samples were not evaluated at 23 °C, because the chemicals adsorbed on the A samples were almost outgassed by the heating the samples at 100 °C.

Analyses of the outgassing from $PM_{2.5}$ by TOR, IC and TD-GC-MS

Carbonaceous species (OC and EC) of the outgassing from the $PM_{2.5}$ samples were obtained by analyzing the $PM_{2.5}$ samples, which were collected daily by IEECAS (Cao et al. 2012b), through the TOR method (DRI model 2001 Thermal/Optical Carbon Analyzer,

Atmoslytic Inc.) (Chow et al. 2007) as shown in Table 4-2 (see Table 4-S1 for more details). In addition, water soluble ions were also analyzed by the IC (Dionex 600, Dionex Corp.) (Cao et al. 2012b) and depicted in Table 4-2 and 4-S1. The concentrations of OC/EC and water soluble ions were compared with the outgassing measurement results by the soft X-ray radiolysis method to figure out dominant species of the outgassing for the particle generation processes. Sampling the A and B samples was conducted continuously in each sampling period and finished in 3 days for each set of samples in the two periods. Therefore, the concentration of the ambient $PM_{2.5}$ for the A and B samples as described in Table 4-1 was different with the concentration of the $PM_{2.5}$ for the OC/EC analysis as described in Table 4-2.

The outgassing from the B samples was analyzed by the TD-GC-MS (6890 GC-5973 MS, Agilent technologies, Inc.) with a thermal desorption unit/cooled injection system (TDU/CIS, Gerstel, Inc.) (Kim et al. 2016b) using the other set of the B samples. The TD-GC-MS was calibrated using toluene as a standard for the analysis. Quarter of each B sample was prepared and put in the TDU/CIS for capturing outgassing from the sample. Then, outgassing from the $PM_{2.5}$ sample were collected on tenax TA liners using the auto sampler in the TDU/CIS. Then, the total volatile compound (TVOC) of the trapped outgassing on the tenax TA liners was measured by increasing the oven temperature of the GC-MS from 40 to 280 °C and the composition of the outgassing were analyzed during the measurement based on the list of the compounds, which was obtained from literature (Mølhave et al. 1986; Mølhave et al. 1997; Billet et al. 2007; Billet et al. 2008) (see Table 4-S2 for the details of the compound list). The TVOC and the detected compounds are

listed in Table 3. For the TD-GC-MS, one filter sample obtained from the semiconductor manufacturing facility (Industry sample) in Xi'an was also analyzed and compared with the results of the B samples.

4.3 Results and discussion

Through the feasibility tests using the A samples, the N_p measured by the UCPC changed with the actual mass loading of $PM_{2.5}$ as shown in Figure 4-2a. The actual $PM_{2.5}$ mass loading of A5 lower than that of A4 caused lower N_p than A4. When the N_p was plotted according to the actual mass loading of the A samples (see Figure 2b), the measured N_p increased linearly with the actual $PM_{2.5}$ mass loading. The large deviation of A4 was caused by decreasing outgassing from the $PM_{2.5}$ during the repeated measurement. Because the amount of the chemicals adsorbed on the surface of the $PM_{2.5}$ was limited and not refilled again, the concentration of the outgassing decreased continuously, which made the large deviation. Therefore, the deviations of A1 and A2 were much smaller than that of A4 with the $PM_{2.5}$ mass loading due to the small amount of the outgassing. Interestingly, the N_p for A3 was similar to A5, although their $PM_{2.5}$ mass loadings was different. This phenomenon might be caused by the concentration of the ambient $PM_{2.5}$ for A5 (60 $\mu g/m^3$), which was lower than other A samples as described in Table 4-1. In other words, the amount of chemicals adsorbed on the $PM_{2.5}$ surface of A5 was lower than other A samples, because the concentration of the gaseous contaminants in the ambient air during sampling A5 might be lower than other samples as the ambient $PM_{2.5}$ due to cleaner ambient air.

(a)

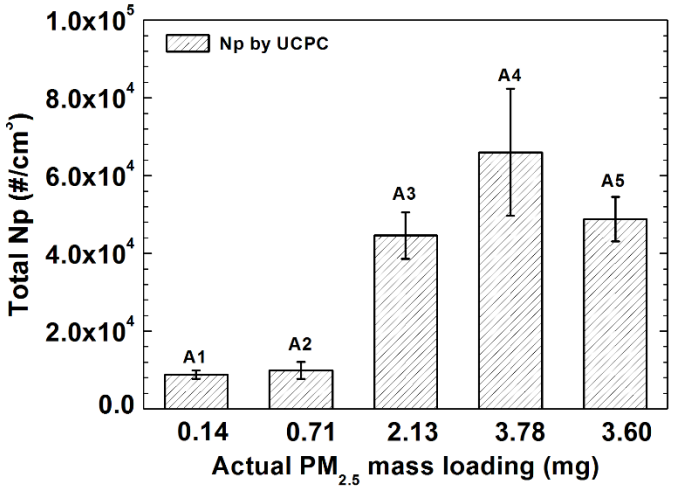

(b)

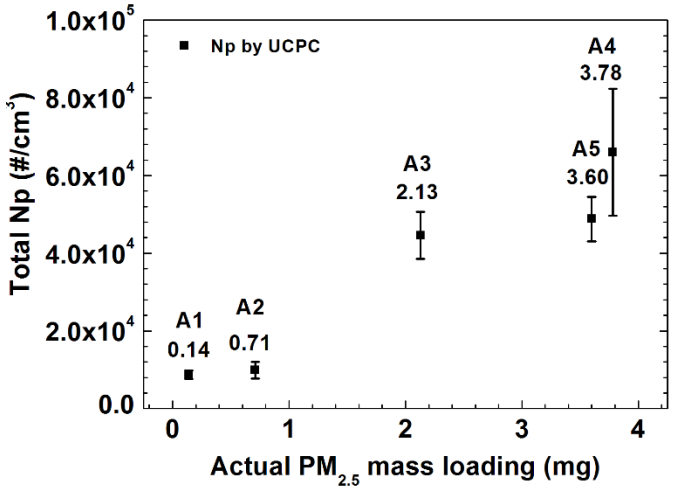

Figure 4-2. Total particle number concentration (Np) according to the actual mass loading of the $PM_{2.5}$ samples collected in the A period (A samples). The samples were heated at 100 °C and the UCPC was used to measure the nanoparticles generated in the soft X-ray conversion chamber.

Figure 4-3 shows the number and volume distributions of the nanoparticles generated from the outgassing of the B samples through the soft X-ray radiolysis at 23 and 100 °C. The magnitude of the distributions for the B samples also increased with the actual $PM_{2.5}$ mass loading. In addition, the deviation of the outgassing increased with the mass loading of the B samples as the A samples showed due to decreasing outgassing during repeating the measurement.

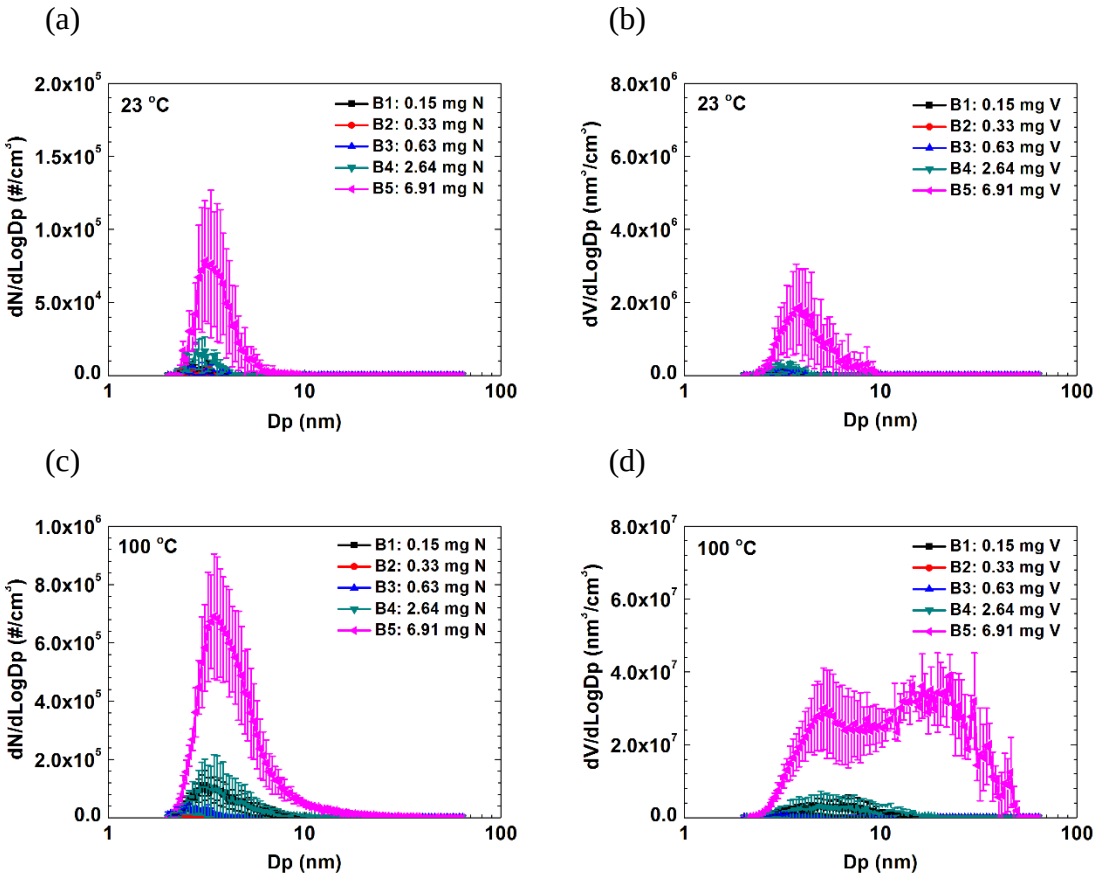

Figure 4-3. Size distributions of the nanoparticles converted from the outgassing from the B samples: (a) number and (b) volume distributions at 23 °C, and (c) number and (d) volume distributions at 100 °C

The peak intensity for the number distribution increased with heating temperature of the outgassing chamber from $8x10^4$ (23 °C) to $6.8x10^5$ #/cm^3 (100 °C) as shown in Figure 4-3a and c, because the desorption of the chemicals from the $PM_{2.5}$ was facilitated at the higher temperature. The peak intensity for the volume distribution also increased with the heating temperature, and the overall shape of the volume distribution changed from unimodal (one-peak) to bimodal (two-peaks) (see Figure 4-3b and d), while the number distribution maintained the unimodal shape due to the high contribution of large size particles on the volume.

After integrating the number and volume distributions to calculate the N_p and V_p, the N_p and V_p were plotted according to the actual $PM_{2.5}$ mass loading as shown in Figure 4-4. They also increased linearly with the actual $PM_{2.5}$ mass loading at both 23 and 100 °C, as the results of the feasibility tests using the A samples (see Figure 4-2b). The R^2 of the trend lines was larger than 0.89. The N_p and V_p for B1 – B3 samples were very close to each other at 23 °C as depicted in Figure 4a and b. However, Figure 4-4c and d show the N_p and V_p of B1 is higher than those of B2 and B3 at 100 °C. The concentration of ambient $PM_{2.5}$ for B2 and B3 (50 μg/m^3), which was lower than that for B1 (100 μg/m^3), also can cause the phenomenon as did for A5. In addition, the difference of the outgassing between them was amplified by increasing the heating temperature, and then clearly seen at 100 °C. Although the N_p and V_p for B4 (580 #/cm^3 and 8,078 nm^3/cm^3) were below the fitting curve, they are 4 – 5 times higher than those for B1 (2,308 #/cm^3 and 37,480 nm^3/cm^3).

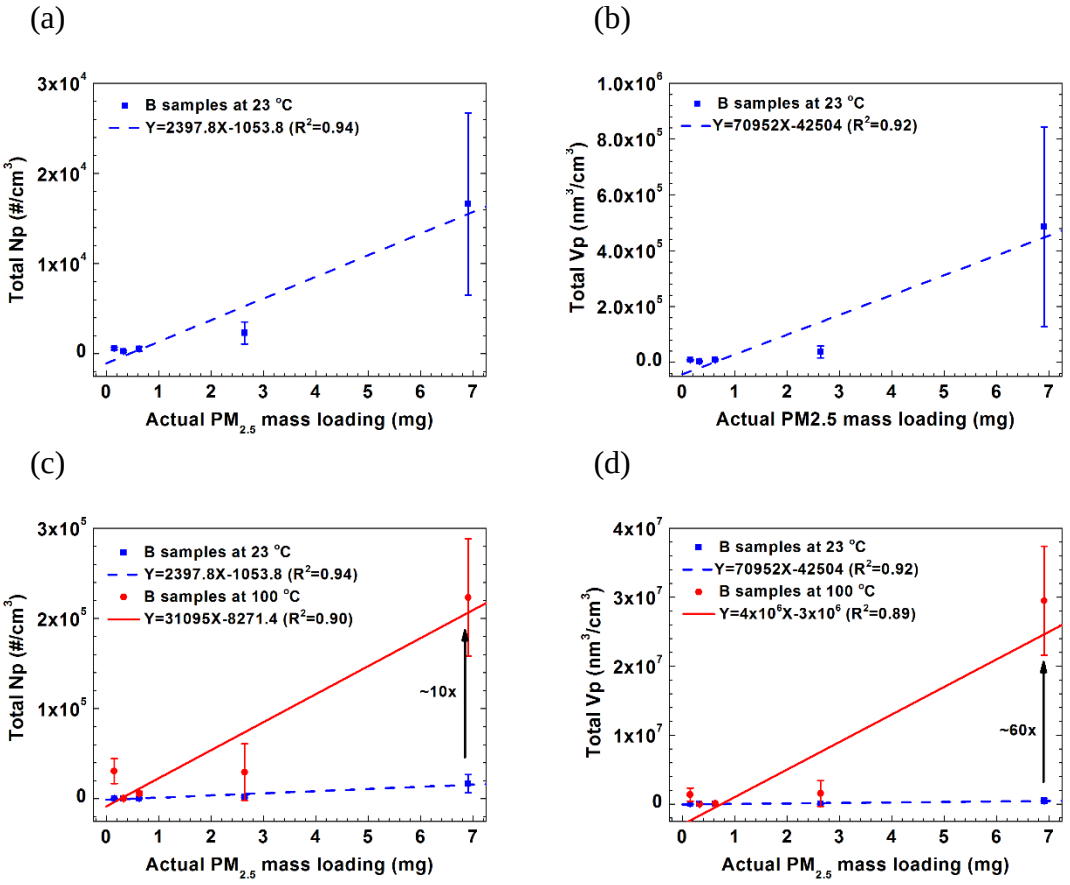

Figure 4-4. Correlations between the total particle (a) number or (b) volume concentrations and the actual mass loading of the B samples at 23 °C. The correlations at 23 and 100 °C are plotted together for total particle (c) number or (d) volume concentrations.

Table 4-2 shows the concentrations of the carbonaceous species (OC and EC) and the water soluble ions from the daily $PM_{2.5}$ samples collected by IEECAS. SOA and SIA can be generated through the soft X-ray radiolysis from the carbonaceous species (OC and EC) and the water soluble ions (NO_3^-, SO_4^{2-} and NH_4^+), respectively. The ratio of the OC and EC concentrations between the $PM_{2.5}$ samples followed the ratio of the $PM_{2.5}$ concentrations. However, the water soluble ions showed different ratios and did not follow

the ratio of the $PM_{2.5}$ concentrations. As shown in Figure 4-2 and 4-4, the concentration of the nanoparticles generated through the soft X-ray radiolysis increased linearly according to the actual $PM_{2.5}$ mass loading. Therefore, these ratios imply the generation of outgassing originated nanoparticles was initiated dominantly by the carbonaceous species (OC and EC), more than by inorganic ions (water soluble ions). In particular, OC contributes much more than EC because OC represents different kinds of hydrocarbons, which EC consists of nearly pure carbon (Fu et al. 2012). In other words, SOA is more abundant in the nanoparticles originated from the outgassing than SIA. For synthesizing SIA, OH radicals from water vapors are very important components than SOA (Kim et al. 2015; Kim et al. 2016b), but this study was conducted without introducing water vapors intentionally to the soft X-ray radiolysis chamber. The very dry experimental condition might also contribute to the low SIA concentration.

Table 4-2. Concentrations of the carbonaceous species (organic and elemental carbon, OC and EC) and the water soluble ions (NO_3^-, SO_4^{2-} and NH_4^+) from the $PM_{2.5}$ samples collected daily by IEECAS in Xi'an, China (more compounds are depicted in Table S1)

Sampling period	$PM_{2.5}$		OC		EC		NO_3^-		SO_4^{2-}		NH_4^+	
	Conc. ($\mu g/m^3$)	Ratio	Conc. ($\mu g/m^3$)	Ratio	Conc. ($\mu g/m^3$)	Ratio	Conc. ($\mu g/m^3$)	Ratio	Conc. ($\mu g/m^3$)	Ratio	Conc. ($\mu g/m^3$)	Ratio
A-1	**138.8**	**1.00**	**37.99**	**1.00**	**9.51**	**1.00**	**30.52**	**1.00**	**15.73**	**1.00**	**11.6**	**1.00**
A-2	**145.6**	**1.05**	**31.57**	**0.83**	**7.81**	**0.82**	**31.33**	**1.03**	**21.33**	**1.36**	**12.59**	**1.09**
A-3	**68.5**	**0.49**	**18.46**	**0.49**	**4.12**	**0.43**	**3.88**	**0.13**	**6.54**	**0.42**	**1.93**	**0.17**
B-1	**51.10**	**1.00**	**12.78**	**1.00**	**2.30**	**1.00**	**4.25**	**1.00**	**6.90**	**1.00**	**1.89**	**1.00**
B-2	**105.80**	**2.07**	**24.64**	**1.93**	**5.11**	**2.22**	**21.14**	**4.97**	**19.77**	**2.87**	**9.85**	**5.21**
B-3	**74.20**	**1.45**	**14.46**	**1.13**	**3.08**	**1.34**	**23.97**	**5.64**	**39.64**	**5.74**	**14.81**	**7.84**

Table 4-3 shows the TVOC and composition of the outgassing from the B samples analyzed by the TD-GC-MS. The TVOC increased with the mass loading of the $PM_{2.5}$ from B1 to B5. However, the outgassing of B1 measured by the soft X-ray radiolysis method was higher than those of B2 and B3, as shown in Figure 4-4. This inconsistency came from the different temperature conditions of the two methods, i.e. 23 and 100 °C for the soft X-ray method; 40 to 280 °C for the TD-GC-MS. Therefore, the TVOC could be higher than the outgassing measured by the soft X-ray method. However, the soft X-ray method can provide results close to the real filtering situation in the semiconductor industry and help the industry estimate the changing period of the filters in the manufacturing facilities (Kim et al. 2016b). For the composition of the outgassing from the $PM_{2.5}$, Propylene glycol, Nonanal and Decanal were found for all B samples, while Acetic acid was only found for B4 and B5 samples. B1 – B3 samples might also release acetic acid, but the concentration of Acetic acid might be too small to detect by the TD-GC-MS. On the contrary, all the six compounds were found in the outgassing from the Industry filter sample including 2-Ethyl-1-Hexanol and Propanoic acid. The difference between the B samples and the Industry sample came from the location of the sampling. Further study is required to figure out the exact sources of the different compounds depending on the sampling location.

Table 4-3. Total volatile organic compound (TVOC) and composition of the B samples analyzed by TD-GC-MS

Sample	TVOC (μg/g)	Acetic Acid (μg/g)	Propylene Glycol (μg/g)	2-Ethly-1-Hexanol (μg/g)	Nonanal (μg/g)	Decanal (μg/g)	Propanoic Acid (μg/g)
B1	**3.8**	**n/a**	**0.41**	**n/a**	**0.25**	**0.52**	**n/a**
B2	**5.3**	**n/a**	**0.77**	**n/a**	**0.30**	**0.36**	**n/a**
B3	**5.2**	**n/a**	**0.94**	**n/a**	**0.46**	**0.23**	**n/a**
B4	**6.7**	**0.10**	**1.46**	**n/a**	**0.66**	**0.17**	**n/a**
B5	**8.2**	**0.13**	**1.40**	**n/a**	**1.07**	**0.21**	**n/a**
Industry	**7.9**	**0.59**	**0.16**	**0.30**	**0.27**	**0.15**	**0.19**

4.4 Summary

The outgassing from the $PM_{2.5}$ samples collected in Xi'an, China was measured by the soft X-ray radiolysis method. The amount of the outgassing from $PM_{2.5}$ measured by the soft X-ray method increased linearly with the $PM_{2.5}$ mass loading. The linear correlation between the outgassing and the $PM_{2.5}$ mass loading was remained at both heating temperatures (23 and 100 °C) of the outgassing chamber. The linearity was well found in the PM2.5 samples collected when the concentration of the ambient PM2.5 was higher than 100 $\mu g/m^3$. However, this can be modified by changing the conditions of the soft X-ray radiolysis method such as residence time in the soft X-ray radiolysis chamber. Simultaneously, the analyses to figure out the chemical composition of the outgassing were conducted using the TOR, IC and TD-GC-MS. The concentrations of the OC and EC analyzed by the TOR method linearly changed with the concentration of the $PM_{2.5}$, but the concentrations of the water soluble ions analyzed by the IC method did not follow the concentration change of the $PM_{2.5}$. When comparing the chemical analysis results with the outgassing levels measured by the soft X-ray method, OC was significantly well detected through the soft X-ray radiolysis method rather than inorganic compounds (i.e. water soluble ions), which might be caused by the very dry condition for the soft X-ray method. The TD-GC-MS results showed the effect of the sampling location on the composition of the outgassing. In addition, the soft X-ray method can be used to estimate the changing period of the filters in the manufacturing facilities because the temperature condition for the soft X-ray was more close to the real filtration condition in the semiconductor industry.

Further study is required to determine the exact sources for the composition of the outgassing from $PM_{2.5}$.

4.5 Supporting information (SI)

Table 4-S1. The details of the chemical analysis for carbonaceous species and water soluble ions.

Sampling period	$PM_{2.5}$ concentration ($\mu g/m^3$)	Carbonaceous species ($\mu g/m^3$)												Water soluble ions ($\mu g/m^3$)								
		TC	OC	EC	OC/EC	OC1	OC2	OC3	OC4	EC1	EC2	EC3	OP2	F^-	Cl^-	NO_3^-	SO_4^{2-}	Na^+	NH_4^+	K^+	Mg_2^+	Ca_2^+
A	138.8	47.50	37.99	9.51	3.99	1.52	8.56	13.99	12.48	10.61	0.33	0.00	1.43	0.62	6.85	30.52	15.73	3.39	11.60	2.28	0.40	1.83
	145.6	39.39	31.57	7.81	4.04	1.48	6.75	10.45	11.36	8.16	0.68	0.51	1.54	0.68	5.79	31.33	21.33	3.70	12.59	2.29	0.53	2.06
	68.5	22.59	18.46	4.12	4.48	0.86	4.58	6.58	5.36	5.05	0.17	0.00	1.09	0.54	3.26	3.88	6.54	3.33	1.93	1.11	0.35	1.43
B	51.1	15.08	12.78	2.30	5.56	0.71	3.02	4.05	3.74	3.02	0.34	0.20	1.26	0.58	3.05	4.25	6.90	3.58	1.89	0.84	0.43	2.09
	105.8	29.75	24.64	5.11	4.82	1.10	5.25	8.22	7.72	7.21	0.25	0.00	2.35	0.55	4.73	21.14	19.77	3.43	9.85	2.27	0.40	1.56
	74.2	17.54	14.46	3.08	4.69	0.87	3.94	4.16	3.73	4.62	0.22	0.00	1.76	1.08	3.40	23.97	39.64	3.84	14.81	2.16	0.47	2.27

Table 4-S2. List of the organic compounds analyzed by the TD-GC-MS

Organic compound	Formula
Benzene	C_6H_6
Toluene	C_7H_8
Nonene	C_9H_{20}
Xylene	C_8H_{10}
Styrene	C_8H_8
1-Ethenyltrimethylbenzene	$C_{11}H_{14}$
Decane	$C_{10}H_{22}$
Diethlybenzene	
Limonene epoxyde	$C_{10}H_{16}O$
Tetramethylbenzene	$C_{10}H_{14}$
Naphtalene	$C_{10}H_8$
Methlynaphtalene	$C_{11}H_{10}$
Dimethylnaphtalene	$C_{12}H_{12}$
Heptadecane	$C_{17}H_{36}$
Anthracene	$C_{14}H_{10}$
Phenanthrene	$C_{14}H_{10}$
Dibutylphtalate	$C_{16}H_{22}O_4$
Eicosane	$C_{20}H_{42}$
Fluoranthene	$C_{16}H_{10}$
Henicosane	$C_{21}H_{44}$
Docosane	$C_{22}H_{46}$
Tricosane	$C_{23}H_{48}$
Tetracosane	$C_{24}H_{50}$
Pentacosane	$C_{25}H_{52}$
Bis(ethyl.hexyl)phtalate	$C_{24}H_{38}O_4$
Acenaphthene	$C_{12}H_{10}$
Fluorene	$C_{13}H_{10}$
Pyrene	$C_{16}H_{10}$
Benzo(a)anthracene	$C_{18}H_{12}$
Chrysene	$C_{18}H_{12}$
Benzo(b+k)fluoranthene	$C_{20}H_{12}$
Benzo(a)pyrene	$C_{20}H_{12}$
Ethylbenzene	C_8H_{10}
Trimethylsilanol	$C_3H_{10}OSi$
Trimethylbenzene	C_9H_{12}
2-Butanone	C_4H_8O
Acetic acid, ethyl ester	$C_4H_8O_2$
Acetic acid, butyl ester	$C_6H_{12}O_2$
o-Xylene	C_8H_{10}
p-Xylene	C_8H_{10}
2-ethyl-1-Hexanol	$C_8H_{18}O$
Propanoic acid, 3-propanediyl ester	
Perfluorotributylamine	$C_{12}F_{27}N$

III. Filtration of AMC and Nanoparticles

Chapter 5: Experimental Study on The Filtration Efficiency of GACs for 3 – 30 nm Particles

5.1 Introduction

Diffusion is the sole mechanism for the gas filtration by adsorption. During adsorption, gas molecules are diffused deep into the gas filters, such as activated carbons (ACs), and removed when they are adhered on the filter surface. Due to the large surface area by pores, ACs are widely used to eliminate gaseous contaminants through adsorption (Bansal and Goyal 2005). However, diffusion is also a dominant filtration mechanism for nanoparticles (NPs) smaller than 100 nm (Japuntich et al. 2007; Kim et al. 2007; Wang et al. 2007). Therefore, if the particle size decreases down to single-digit nanometers, NPs can be diffused into the AC pores and be deposited on the pore surface. The particle deposition can degrade the gas filtration efficiency of ACs by blocking pores, the gas capturing sites through adsorption. In other words, the breakthrough of ACs for gases can be accelerated due to the deposition of NPs on the pores of ACs. Therefore, the nanoparticle deposition through diffusion should be considered to determine the gas filtration efficiency of ACs.

The filtration of NPs has been substantially investigated with fibrous filters such as high-efficiency and ultra-low- particulate air (HEPA and ULPA) filters (Japuntich et al. 2007; Kim et al. 2007; Wang et al. 2007). The filtration efficiency of these fibrous filters increases with the inverse of the particle size due to diffusion. In addition, granular shaped packed-beds (e.g. glass beads, sands and quartz gravels) also have been studied as filter

media for NPs (Paretsky et al. 1971; Gebhart et al. 1973; Schmidt et al. 1978; Lee and Gieseke 1979). The diffusive filtration efficiency trend and model of packed-beds were similar to those of fibrous filters because fibrous filters and packed-beds removed NPs by the external deposition. ACs also can be classified as packed-beds due to its granular shapes. However, the filtration efficiency of ACs for NPs can be different from other non-porous filter media due to the internal diffusive deposition of NPs on the pore surface. The internal deposition of NPs has not been considered much because ACs are generally used as gas filters, not as particle filters. Therefore, the objectives of this study were to investigate the diffusive filtration efficiency (E_d) of ACs for NPs, down to single-digit nanometers at different conditions and to compare it with previous models for fibrous filters and packed-beds for finding the effect of the internal deposition of NPs through diffusion.

5.2 Materials and methods

The experimental setup is as shown in Figure 5-1. For this study, two methods were used to produce three kinds of NPs. First, the evaporation and condensation method using a tube furnace (Lindberg/blue M, STF55030C-1, Thermo electron corporation) generated polydisperse silver (Ag) NPs at 1020 ^{o}C (3 to 10 nm) and 1100 ^{o}C (15 to 30 nm), which were carried by nitrogen (N_2) at 1.5 lpm. Polydisperse sulfuric acid and ammonium sulfate (H_2SO_4 and $(NH_4)_2SO_4$) NPs were synthesized through gas-to-particle conversion assisted by soft X-ray in the soft X-ray conversion chamber (Kim et al. 2015). The source of these two NPs were prepared by mixing 2 ppm SO_2/N_2 and 2 ppm NH_3/N_2 gases (Oxygen Service

Company) with N_2 at the ratios of N_2:SO_2/N_2:NH_3/N_2 = 0.9:0.2:0.4 and 1.5:0.3:0.6 (total flow rates were 1.5 and 2.4 lpm), which correspond to the face velocities (FVs), 2.46 and 3.93 cm/s, respectively. Monodisperse NPs at 3~30 nm were classified from polydisperse NPs by a nano differential mobility analyzer (nanoDMA, TSI 3080 and 3085, TSI Inc.). All NPs upstream and downstream of the nanoDMA were neutralized by two radioactive materials (Po-210). The monodisperse NPs were introduced into the gas filter holder, which was made of stainless steel with 36 mm ID and 27 mm inner height. Granular shaped ACs used in this study were sampled from 3M carbon filters (GVP-403, 3M). The apparent density and size of the ACs were in the range of 0.4~0.44 g/cm^3 and 1.1~1.3 mm, respectively. The average pore size of the ACs was in the rage of 10~20 nm, and the smallest size of the pores is less than 2 nm. When the gas filter holder filled with 15 mm ACs was challenged only by N_2 up to 10 lpm (FV was 16.4 cm/s), no particle shedding downstream of the holder was observed by an ultrafine condensation particle counter (UCPC, TSI 3776, TSI Inc.). The pressure drop (ΔP) between upstream and downstream of the holder was measured by a magnehelic gauge (25.4 mmH_2O, Dwyer instruments). The particle number concentrations upstream and downstream of the gas filter holder were measured by the UCPC.

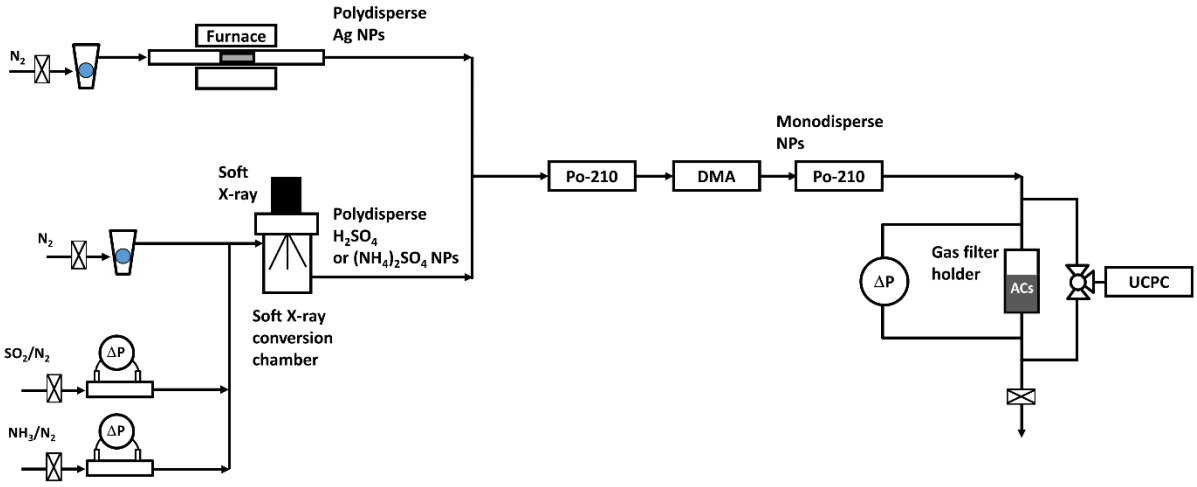

Figure 5-1. Schematic diagram of the experimental setup for the evaluation of the diffusive filtration efficiency (E_d) of activated carbons (ACs) for three kinds of nanoparticles (NPs) such as silver (Ag), sulfuric acid (H_2SO_4) and ammonium sulfate ($(NH_4)_2SO_4$)

The penetration ratio (P) of ACs was calculated by the ratio of particle number concentrations downstream to upstream of ACs. E_d was obtained from the penetration as

$$E_d = 1 - P. \quad (1)$$

Because piling of NPs on the pore surfaces can change E_d, only brand-new ACs were used for every experiment at different conditions to avoid the aging effect of the ACs on E_d. Therefore, all experimental results of this study showed the initial filtration efficiency of unused ACs. To compare the experimental E_d ($E_{d,exp}$) of this study with the models for

fibrous filters and packed-beds (Lee and Gieseke 1979; Wang et al. 2007), $E_{d,exp}$ was converted into the experimental single sphere efficiency ($\eta_{d,exp}$) through

$$\eta_{d,exp} = -\frac{2(1-\alpha)d_s}{3\alpha t}\ln\left(1 - E_{d,exp}\right), \quad (2)$$

where α is the solidity, t is the thickness of the filter and d_s is the mean diameters of the packed-bed. $\eta_{d,exp}$ was compared with the single fiber efficiency ($\eta_{d,\text{ single fiber}}$) and the single sphere efficiency ($\eta_{d,\text{ single sphere}}$) given by Wang et al. (2007) and Lee and Gieseke (1979) as

$$\eta_{d,single\ fiber} = \eta_{d,Wang} = 0.84Pe^{-0.43}, \quad (3)$$

$$\eta_{d,single\ sphere} = \eta_{d,Lee} = 3.5\left(\frac{1-\alpha}{K}\right)^{\frac{1}{3}}Pe^{-\frac{2}{3}}, \quad (4)$$

$$\text{Pe} = \frac{U_0 d_f}{D} \text{ or } \frac{U_0 d_s}{D}, \quad (5)$$

where K is Kuwabara hydrodynamic factor, which represents the flow field around the filter media (Lee and Gieseke 1979), D is the diffusion coefficient and U_0 is the face velocity. α of the ACs is the packing density, which is the ratio of the apparent density to the solid density. If the solid density of the ACs was 2 g/cm^3 (the density of amorphous carbons without pores) (McKenzie et al. 1991) and the apparent density was 0.44 g/cm^3 (the measured density of the ACs including pores within ACs and void space between

ACs), the α was 0.22, which was 3 times lower than α of the pack-beds in the literature (0.6) (Lee and Gieseke 1979). The t and the d_s used for the conversion were 10 mm and 1.3 mm, respectively.

5.2 Results and discussion

$E_{d,exp}$ and ΔP of ACs for 3 nm Ag NPs according to the amount of ACs are depicted in Figure 5-2. The amount of ACs was controlled and described by the height of ACs in the gas filter holder. $E_{d,exp}$ increased from 92.6 % to 99.5 % with the height of ACs from 5 to 15 mm. The corresponding ΔP also increased from 1 to 7 mmH_2O, which was similar to that of much thinner fibrous filters with smaller solidities (Kim et al. 2007; Wang et al. 2007). The large standard deviation at 5 mm ACs was caused by insufficient coverage of ACs in the holder. In this study, the height of ACs was fixed at 10 mm to observe more clearly the change of $E_{d,exp}$ of ACs according to the particle size.

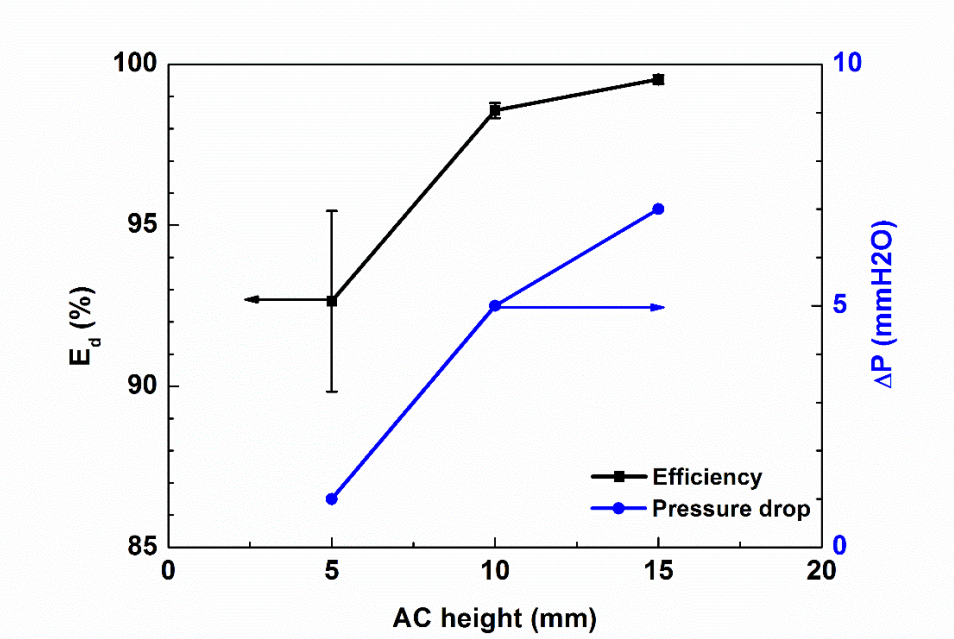

Figure 5-2. Diffusive filtration efficiency (E_d, black squares) and pressure drop (ΔP, blue circles) of ACs for 3 nm silver (Ag) NPs at different activated carbon (AC) heights (5, 10 and 15 mm)

Figure 5-3a shows $E_{d,exp}$ of ACs for the three kinds of NPs from 3 to 30 nm. $E_{d,exp}$ decreased with the inverse of the size of NP due to diffusion, and no significant difference was found among the different compositions of NPs. However, $E_{d,exp}$ decreased with FV as shown in Figure 5-3b. Based on the single sphere theory , E_d is a function of Pe, which is proportional to FV. When FV increases, Pe increases, thus reducing $\eta_{d,\ single\ sphere}$. This results in the decrease of E_d. However, E_d was not changed by the composition of NP, because E_d is not a function of it.

(a)

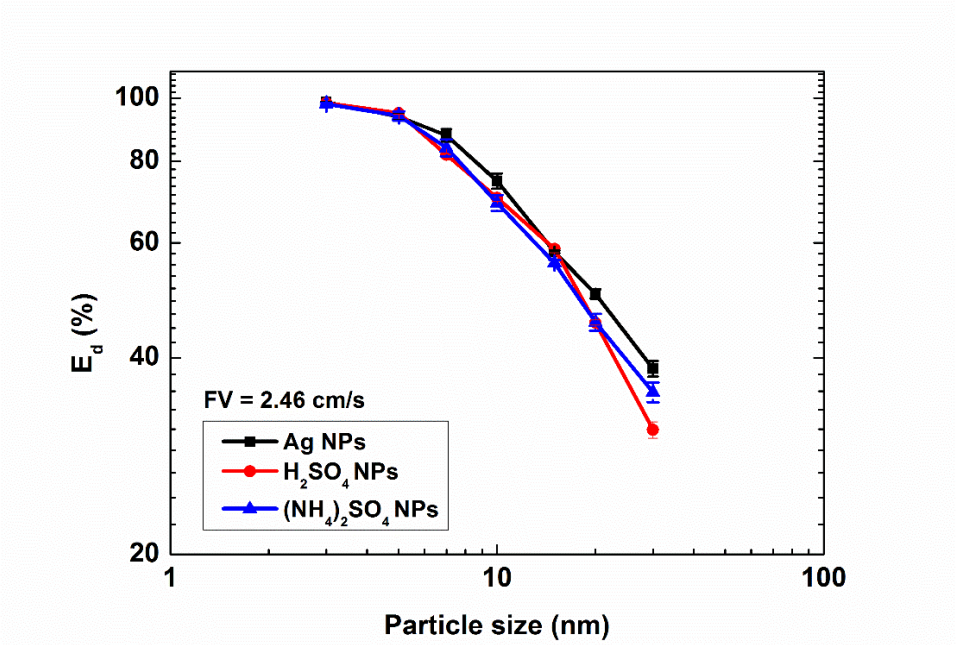

(b)

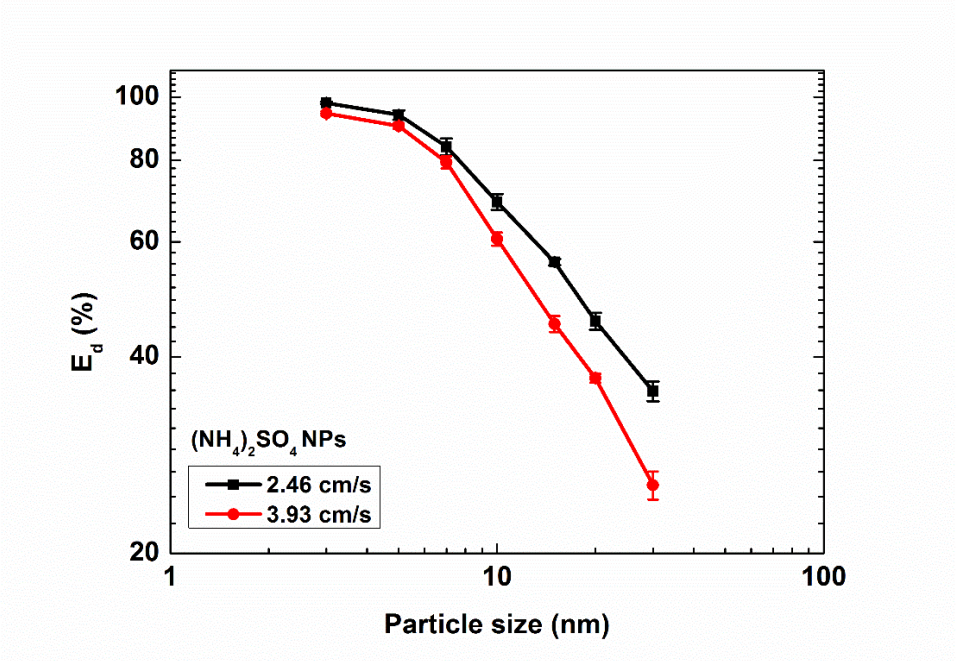

Figure 5-3. Diffusive filtration efficiency (E_d) of activated carbons (ACs) for nanoparticles (NPs) at different (a) particle compositions and (b) face velocities (FVs)

Figure 5-4 shows the comparison of $\eta_{d,exp}$ with the previous models ($\eta_{d,Wang}$ and $\eta_{d,Lee}$) at two αs. At α=0.22, $\eta_{d,exp}$ was higher than $\eta_{d,Wang}$ and $\eta_{d,Lee}$ as shown in Figure 4a. In addition, the slope (the exponent of Pe) of $\eta_{d,exp}$ was different from those of $\eta_{d,Wang}$ and $\eta_{d,Lee}$. When $\eta_{d,exp}$ was fitted on a curve,

$$\eta_{d,exp} = 10.6Pe^{-0.5}. \quad (6)$$

When the largest apparent density of the ACs, 0.44 was used as α, $\eta_{d,exp}$ was getting close to $\eta_{d,Lee}$ as Pe decreased and was almost same at Pe=100 as shown in Figure 4b. The coefficient of the fitting curve for $\eta_{d,exp}$ decreased to 4.68, but the efficiency was still higher than the models for NPs from 3 to 30 nm, which corresponds to Pe=92~13800. Interestingly, the exponents of $\eta_{d,exp}$ for both αs were the same as -0.5, which was between these exponents of two models, -0.43 (fibrous filters, $\eta_{d,Wang}$ (Wang et al. 2007)) and -2/3 (packed-beds, $\eta_{d,Lee}$ (Lee and Gieseke 1979)). In addition, all $\eta_{d,exp}$ are on the same fitting curve at each α, even though FV was different. This was also observed by Wang et al. (2007). Therefore, a simple universal model, which is a function of Pe, can be obtained for different FVs. Although the shape of the ACs was granule (one of the packed-beds), the exponent (-0.5) of Pe was close to that (-0.43) of the fibrous filter media, not that (-2/3) of the granules. However, the exponent was still not same as -0.43. This implicates the diffusive deposition of NPs on the pore surface of the ACs, but Lee and Gieseke's and Wang et al.'s models did not take the internal deposition of the unit collectors into account

because they investigated non-porous filter media. Therefore, this filtration behavior of ACs for NPs cannot be explained neither by the single sphere efficiency nor by the single fiber efficiency model. It requires a new filtration model including filtration mechanism by both external (on the exterior surface of ACs) and internal (on the pore surface) depositions.

(a)

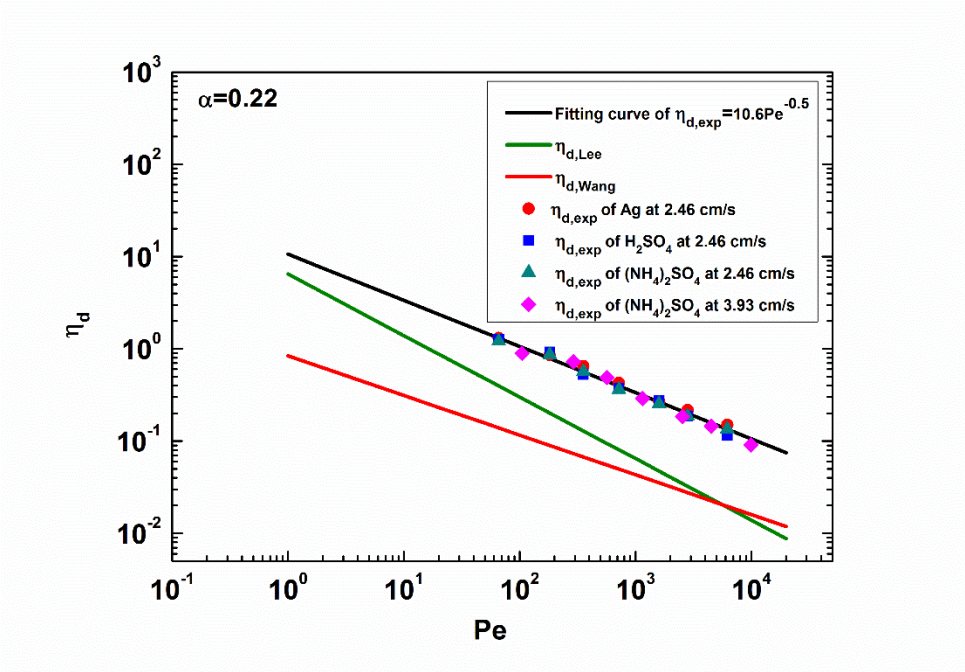

(b)

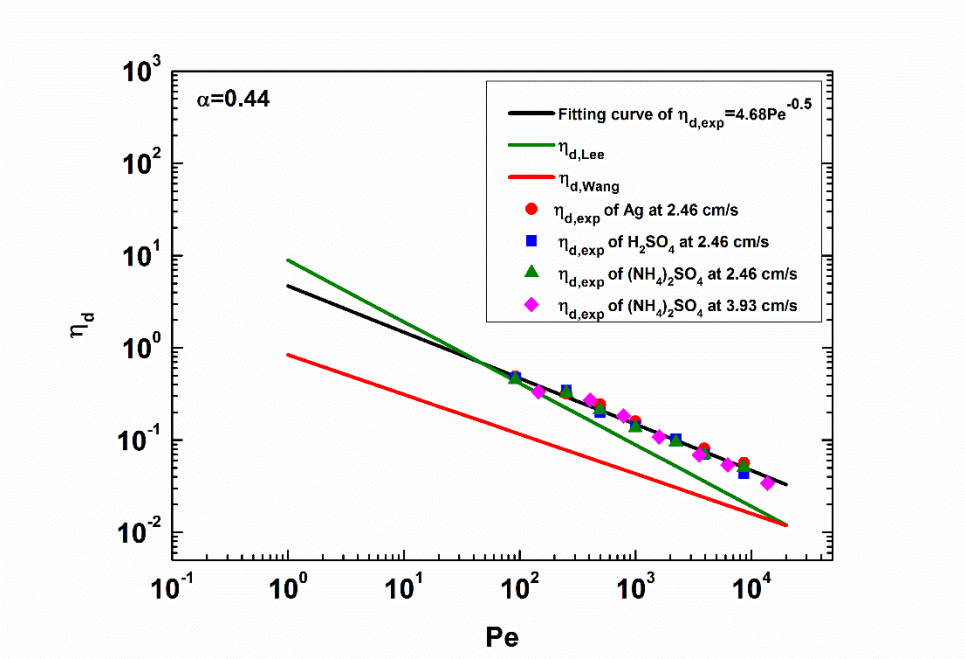

Figure 5-4. Comparison of the experimental single sphere efficiency ($\eta_{d,exp}$) for activated carbons (ACs) with previous models for the single fiber ($\eta_{d,wang}$) and the single sphere ($\eta_{d,Lee}$) at different solidities (αs), (a) 0.22 and (b) 0.44

5.4 Summary

The filtration efficiency of ACs for NPs was evaluated at different conditions such as the composition of NPs and FV. The experimental results showed that the particle composition did not influence the filtration efficiency, but FV did a lot, which was well matched with the previous models for fibrous filters and packed-beds. Although ACs can be categorized into packed-beds due to their granular shapes, the filtration efficiency could not be explained simply by the single sphere efficiency model for the packed-beds. Rather, the trend of the experimental results according to Pe was close to the single fiber efficiency model. This means that the traditional filtration model is not suitable to describe the filtration efficiency of ACs for NPs. To understand the particle filtration behavior of ACs, a new filtration model should be developed by considering both the external deposition on the surface of ACs as well as the internal deposition on the pore surface of ACs. The size of pores can vary the filtration efficiency. If the size of NPs is close to that of gas molecules, the internal deposition of NPs also can influence the filtration performance of ACs for gaseous contaminants by blocking the gas capturing sites through adsorption. Therefore, this and following studies on the filtration behavior of ACs for NPs will be useful for designing filters including ACs for gaseous and particulate contaminants such as activated carbon embedded HEPA filters.

Chapter 6: Removal of Airborne Sub-3 nm Particles Using Fibrous Filters and GACs

6.1 Introduction

Nanoparticles (NPs) have been used in various fields (e.g. medicine, drugs, toothpastes, electronic devices, paints, sensors and foods) (Salata 2004; Reiss and Hütten 2005; Peng et al. 2009; Nie et al. 2010; Weir et al. 2012) due to their distinct properties, which are not found in bulk materials. Moreover, sub-10 nm semiconductor particles, which are known as quantum dots, have been substantially investigated for developing next generation solar cells and light emitting diodes (Jang et al. 2010; Semonin et al. 2011). While the use of engineered NPs is growing drastically, concerns about potential risks of airborne NPs to human health and the environment during the use and production of NPs are also increasing due to their unique physicochemical properties. For example, titanium oxide NPs, which are major ingredients of sunscreens and foods, have been reported as a cause of asthma and Crohn's disease as well as a potential carcinogen (Weir et al. 2012). Another widely-used material for personal care products (e.g. sunscreens and cosmetics), zinc oxide NPs, have been studied due to their ecotoxicology (Ma et al. 2013). Although silver NPs are famous for antibacterial properties, silver ions released from silver NPs are highly toxic to organisms in the environment (Levard et al. 2013). In addition, vehicles emit a lot of particulate matters, especially, sub-10 nm particles (Pedata et al. 2015). Because the surface area to mass ratio of NPs is higher than larger particles, more volatile or semi-volatile compounds can be adsorbed on the surface of NPs emitted from vehicles,

thus increasing potential risks when they enter a human body. Although the toxicity of NPs recently has been vigorously investigated, limited information is available.

Generally, airborne NPs are able to enter a human body through the respiratory tract and cause inflammation in organs (Grassian et al. 2007; Elsaesser and Howard 2012). Therefore, wearing respirators is a highly recommended method to prevent unexpected diseases caused by the airborne NPs (Lee et al. 2008; Eninger et al. 2008). Moreover, installing particle filters or air cleaners in buildings is one of the best ways to keep the indoor air in good quality (Fisk et al. 2002). Exhaust air from producing facilities for engineered NPs and vehicles should be also purified by suitable filter media to protect the environment against potential hazards by discharged NPs.

In the field of the airborne particle filtration, many have extensively investigated the filtration efficiency of fibrous media (e.g. respirators, high efficiency and ultra-low particulate air filters) (Lee and Liu 1982; Japuntich et al. 2007; Kim et al. 2007) as well as packed-beds using granular media (e.g. sands and beads) (Cookson Jr. 1970; Gebhart et al. 1973; Lee and Gieseke 1979) for particles larger than 3 nm. Although previous research on the packed-beds filtration generally have focused on non-porous materials, granular activated carbons (GACs), which are porous materials used for removing gas molecules in air or particles and ions in liquids through adsorption (Bansal and Goyal 2005; Mugisidi et al. 2007; Tennant and Mazyck 2007), are also able to work as packed-beds for removing NPs by the external surface as the non-porous materials. If the particle size decreases down to the molecular levels (~1 nm), the NPs can pass between fibers of particle filters as gas molecules or be bounced from the fibers (known as the thermal rebound (Wang and Otani

2012)), thus reducing the filtration efficiency of the fibrous filters. However, the tiny particles can be diffused into the pores of GACs and deposited on the pore surfaces as gas molecules are captured by the GACs through adsorption. If the filtration efficiency of GACs meets standards for removing NPs of gas streams, GACs are good candidates for eliminating simultaneously both gaseous and particulate contaminants. However, few groups have studied the particle filtration efficiency of GACs (Kim and Pui 2015). In addition, most previous research on the particle filtration efficiency of air filter media has been conducted for particles down to 3 nm due to the detection limit of commercial instruments such as an ultrafine condensation particle counter (UCPC) (McMurry 2000). Therefore, developing instruments for classifying and detecting sub-3 nm particles is another issue when evaluating the air filter media for the sub-3 nm particles (Kim et al. 2006; Iida et al. 2009; Jiang et al. 2011; Fernández de la Mora and Kozlowski 2013).

In this study, we investigated the filtration efficiency of GAC and fibrous filter media for sub-3 nm particles by measuring the penetration of the classified NPs through the filter media. The sub-3 nm particles were classified by a Herrmann-type high resolution differential mobility analyzer (HRDMA) (Herrmann et al. 2000), and the number concentration of NPs upstream and downstream of the filter media were detected by an aerosol electrometer (Heim et al. 2010). Subsequently, the filtration efficiency of the GAC and the fibrous filters for the sub-3 nm particles were compared. Moreover, the single sphere efficiency of the GAC for the sub-3 nm particles were compared with the previous research using 3-30 nm particles (Kim and Pui 2015), to find the effect of the particle size on the particle filtration efficiency of the GAC.

6.2 Materials and methods

Figure 6-1 shows the experimental setup for measuring the penetration of sub-3 nm particles through filter media, such as a GAC (GVP-403, 3M Co.) and fibrous filters (six respirator filters A, B, C, D, E and F, Shigematsu Works, Co., Ltd.). The Herrmann-type HRDMA in Figure 1 was employed to classify sub-3 nm particles. Before classifying sub-3 nm particles, the HRDMA was calibrated using tetraheptyl ammonium bromide (THABr, >99.0 %, Sigma-Aldrich, Co.) ions, which were generated from a methanol-based THABr solution by an electrospray attached to the HRDMA(Ude and De La Mora 2005; Jiang et al. 2011) and carried by the filtered compressed air at 10 lpm. The distribution of the THABr ions according to the applied voltage of the HRDMA was measured by the aerosol electrometer (TSI3068B, TSI Inc.) (dashed line in Figure 6-1). Due to the measurement method, the aerosol electrometer, the THABr ions were not neutralized by a radioactive material (Po-210). From the measured distribution of THABr ions as shown in Figure 6-S1, the HRDMA voltages for THABr ion monomers, dimers and trimers (V_1, V_2 and V_3, see Table 6-S2) were found. The ratios of V_1/V_2 and V_1/V_3 in Table 6-S2 were calculated and compared with the reference ratios (Ude and De La Mora 2005) to determine the accuracy of the HRDMA. Based on the measured V_1, V_2 and V_3, the HRDMA voltage for classifying sub-3 nm particles was calculated as depicted in Table S3. Then, the distribution of THABr ions was measured again after conducting experiments to evaluate the stability of the NP generation using the experimental system in Figure 6-1 (see the detailed procedure in supporting information (SI)).

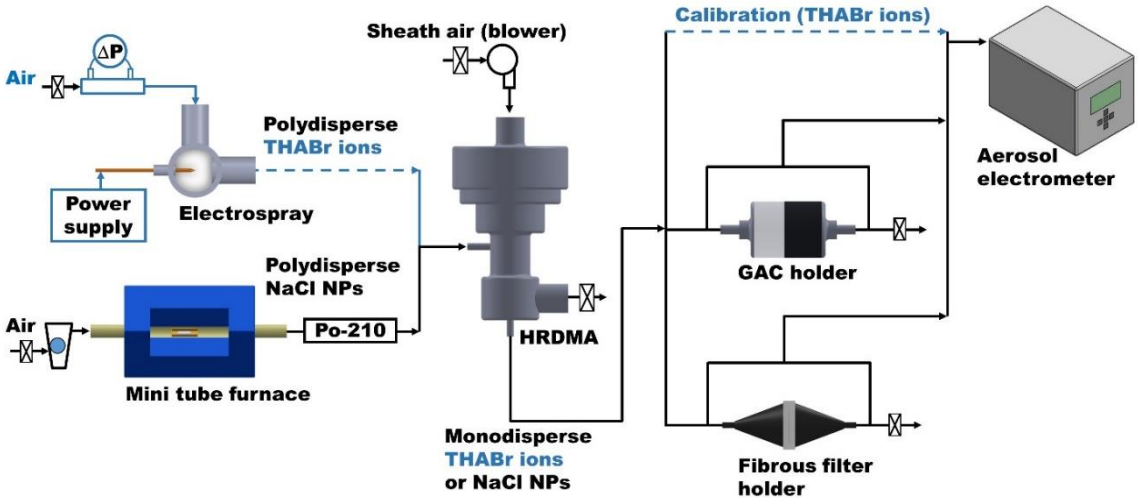

Figure 6-1. The experimental setup for measuring penetration of sub-3 nm particles through the granular activated carbon (GAC) and the fibrous filters. The sodium chloride NPs (NaCl NPs) were classified by the high resolution differential mobility analyzer (HRDMA), which was calibrated using tetraheptyl ammonium bromide (THABr) ions.

For the test aerosol, sodium chloride (NaCl, >99.0 %, Sigma-Aldrich Co.) NPs were produced by the evaporation and condensation method using a tube furnace (Lindberg/blue M, STF55030C-1, Thermo electron corporation). A NaCl contained boat was placed in the center of the furnace and heated below the melting point of NaCl, 800 °C, to control the peak size of NaCl NPs smaller than 10 nm and prevent NaCl from melting down. The generated NPs were also carried by the filtered compressed air at 10 lpm to use the HRDMA voltage, which was calibrated by THABr ions using the electrospray. After neutralizing the polydisperse NaCl NPs by a Po-210, the NaCl NPs were classified by the HRDMA at 1.5, 2, 3, 4 and 5 nm. The tested particle size range was expanded to 5 nm to

compare the current results with previous research using particles down to 3 nm (Kim and Pui 2015).

Before measuring the penetration of the classified NPs through the filter media, the pressure drop (ΔP) between upstream and downstream of each filter was first measured using magnehelic gauges (Dwyer instruments, Inc.). The ΔP for each filter was calibrated by subtracting the ΔP of its filter holder from the total ΔP. The distance between upstream and downstream of the filter media was 12 in. (about 30 cm). The inner diameters of the GAC holder and fibrous filter holder were 36 and 38 mm, respectively. Figure 6-2a shows the ΔP caused by the two filter holders (see Figure 6-1) for the fibrous filters and GAC. The ΔP between upstream and downstream of the fibrous filter holder was similar with that of the GAC holder. By subtracting the ΔP of the holders in Figure 6-2a from the total ΔP measured after mounting the filter media in the holders, the ΔP of each filter was obtained at different face velocities (FVs, see Table 6-1) as shown in Figure 6-2b.

(a) (b)

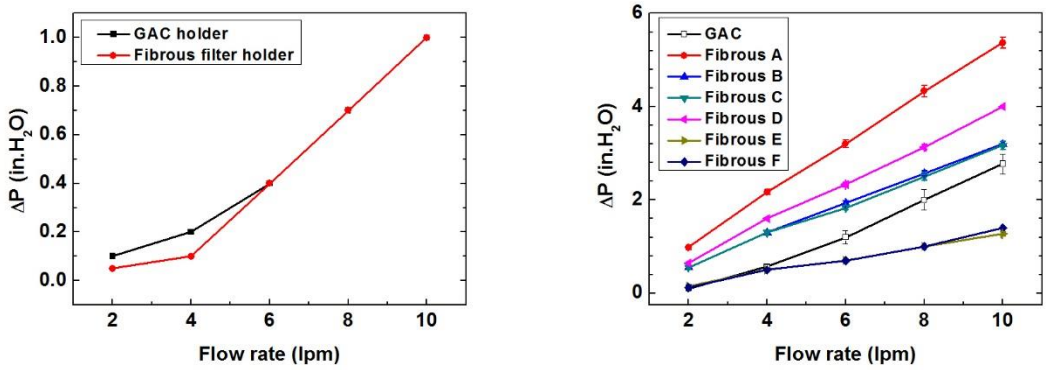

Figure 6-2. The pressure drop (ΔP) (a) across each filter holder and (b) across the granular activated carbon (GAC) and the fibrous filters (A-F)

Table 6-1. The face velocities (FVs) for the granular activated carbon (GAC) and fibrous filters at different flow rates.

Flow rate (lpm)	Face velocity (cm/s)	
	GAC	Fibrous filters
2	3.27	2.94
4	6.55	5.88
6	9.82	8.82
8	13.10	11.76
10	16.37	14.70

The properties of the fibrous filters A-F and the GAC are described in Table 6-2. The fibrous filters A-F were made of mainly 4 different size glass wools and binder fibers. Especially, the fibrous filters E and F included activated carbon fibers for eliminating nasal level gas contamination. To compare the particle filtration efficiency of the GAC for sub-3 nm particles with that for 3-30 nm particles, the same GAC tested in previous research (Kim and Pui 2015) was used in the present work. The surface structures of the filter media were analyzed by a field-emission gun scanning electron microscope (FEG-SEM 6500F, JEOL Ltd.) as shown in Figure 6-3.

As previously noted, the THABr ions were not neutralized by a Po-210 during the calibration of the HRDMA due to the aerosol electrometer. For the same reason, the classified NPs were also not neutralized by a Po-210. Therefore, the monodisperse and singly positive-charged (+1) NaCl NPs were introduced into the filter holders. Because the particles size was in single digit nm, the multiple charge effect was negligible. In addition,

no electrostatic field was built in the GAC and fibrous filter holders because the experimental setup was grounded using conductive materials (e.g. stainless steel holders and conductive tubes). Although the fibrous filters might have few charges, the effect of the charge was assumed as negligible in this study due to the high particle filtration efficiency of the fibrous filters by diffusion.

The penetration (P) of NPs through each filter was calculated from the ratio of particle number concentrations upstream (C_{up}) and downstream (C_{down}) of the filter measured by the aerosol electrometer as

$$P = \frac{C_{down}}{C_{up}}. \quad (1)$$

The aerosol electrometer has the lower detection limit, 0.1 fA (~10^{-16}A), which corresponds to 20 cm^{-3} at 2 lpm (4 cm^{-3} at 10 lpm) (McMurry 2000). In this study, the C_{down} measured by the aerosol electrometer was accepted for calculating the P, when the C_{down} was higher than 50 cm^{-3}. Or, the C_{down} was assumed as zero. For the fibrous filters, the measured C_{down} was lower than 50 cm^{-3} at all conditions. Therefore, the C_{down} was assumed as zero, and then the P was calculated as zero. However, the GAC filter showed the C_{down} lower than 50 cm^{-3} at only some measurements using 1.5 nm particles.

Then, the diffusive filtration efficiency (E_d) of each filter was calculated from P through

$$E_d = 1 - P. \quad (2)$$

The P of NPs were measured at different FVs, which were controlled by the inlet flow rate of the aerosol electrometer as shown in Table 6-1. The FVs for the fibrous filters were slightly different from those for the GAC due to the difference of the inner diameter between two filter holders. For measuring P, the GAC was filled in the holder at 10 mm and the thickness of the fibrous filters were between 400 and 800 μm as described in Table 2.

For comparing the current results with the previous results about the particle filtration efficiency of the GAC, the experimental P of sub-3 nm particles through GACs was converted into the single sphere efficiency (η_d) at two solidities (αs, see Table 2) by the following equation (Kim and Pui 2015):

$$\eta_d = -\frac{2(1-\alpha)d_s}{3\alpha t}\ln(1 - E_d), \quad (3)$$

where, d_s is the granule diameter of GACs and t is the thickness of GACs. The curve fitting of the η_d was a power-law as a function of the Peclet number (Pe) (Kim and Pui 2015) as

$$\eta_d = APe^m, \quad (4)$$

where, A and m are the coefficient and exponent of the power-law. The m of the Pe for each fitting curve was compared with previous results using 3-30 nm particles (Kim and

Pui 2015). Also, m for the whole particle size range (1.5-30 nm) was obtained and compared with each particle size range, i.e., 1.5-5 nm and 3-30 nm.

6.3 Results and discussion

Table 6-2 shows that the fibrous filters A and B had the same fiber compositions with C and D, respectively. However, the fibrous filters A and D had higher ΔP than C and B due to the t as shown in Figure 6-2b. The fibrous filter C and D had same t, but C showed lower ΔP because C had larger average fiber diameter than D (Wang and Otani 2012). In addition, the fibrous filters A-D had higher ΔP than the GAC at all flow rates (2-10 lpm), but E and F had similar (at 2-4 lpm) or lower (at higher than 4 lpm) ΔP than the GAC as shown in Figure 6-2b. Although the fibrous filters C-F had similar t, E and F showed lower ΔP than C and D because E and F had a larger average fiber diameter than C and D. Although the ΔP of the GAC was similar with or higher than the fibrous filter E and F, the t of the GAC (10 mm) was 100 times thicker than those of the fibrous filters (less than 1 mm), thus increasing the ΔP of the GAC. Figure 6-3 shows the SEM images of the fibrous filters A-F and the GAC. As shown in Figure 6-3a-f, the fibrous filters A-F consisted of different size glass wools and binding materials (see Table 6-2), but no significant difference was observed among different fibrous filters. Also, the activated carbon fibers of the fibrous filters E and F were not distinguished by the SEM images. Figure 6-3g and h show the millimeter-size GAC and its surface with pores, which increased the surface area of the GAC. Even though the SEM images shows only micrometer-size pores on the

GAC, the GAC also had nanometer-size pores that capture gas molecules inside (Kim and Pui 2015).

Table 6-2. The properties of the granular activated carbon (GAC) and fibrous filters

Filter media	Thickness (t) (mm)	Solidity (α)	Granule diameter (d_s) (mm)
GAC	**10**	**0.22 (= packing density at bulk density = 2 g/cm^3), 0.44 (= apparent density)**	**1.3**

Filter media		Thickness (mm)	Fiber diameter (μm)					
			Weight ratio of fibers (%)					
			Glass wool 1 (1.8)	Glass wool 2 (1.0)	Glass wool 3 (0.65)	Glass wool 4 (0.50)	Binder fiber (13.0)	Activated carbon fiber (9.34)
Fibrous filter	A	0.8	35	-	-	20	45	-
	B	0.41	-	-	50	10	40	-
	C	0.65	35	-	-	20	45	-
	D	0.64	-	-	50	10	40	-
	E	0.63	-	35	10	-	35	20
	F	0.62	-	30	10	5	40	15

(a)

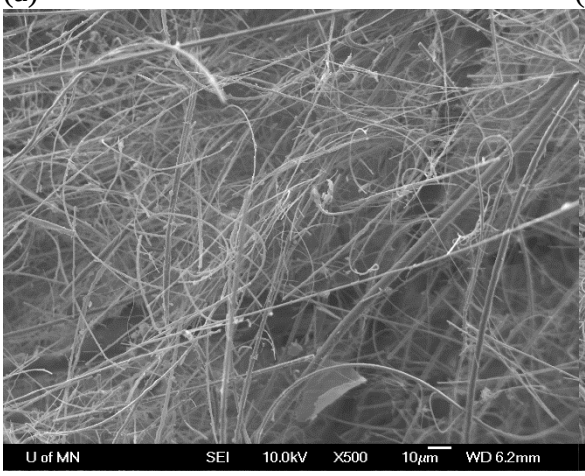
U of MN SEI 10.0kV X500 10μm WD 6.2mm

(b)

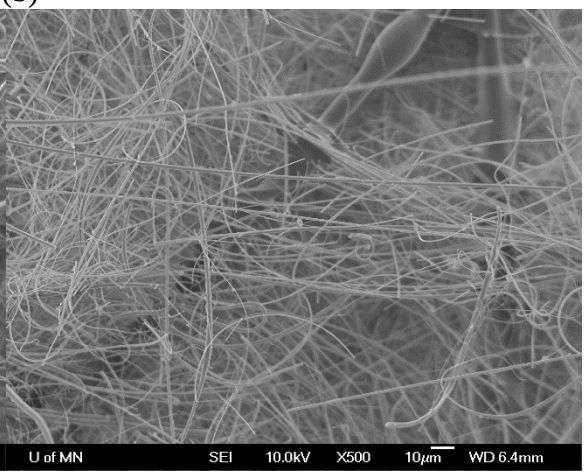
U of MN SEI 10.0kV X500 10μm WD 6.4mm

(c)

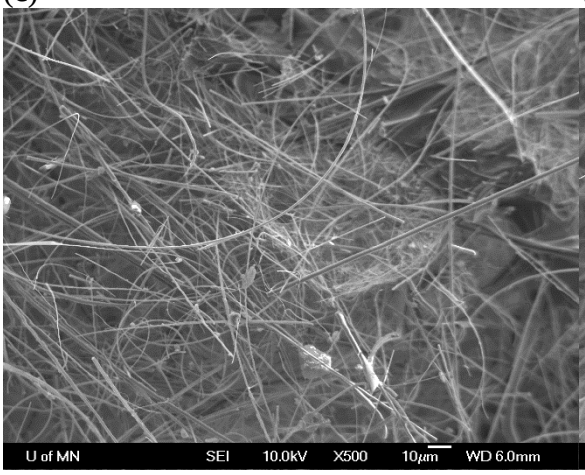
U of MN SEI 10.0kV X500 10μm WD 6.0mm

(d)

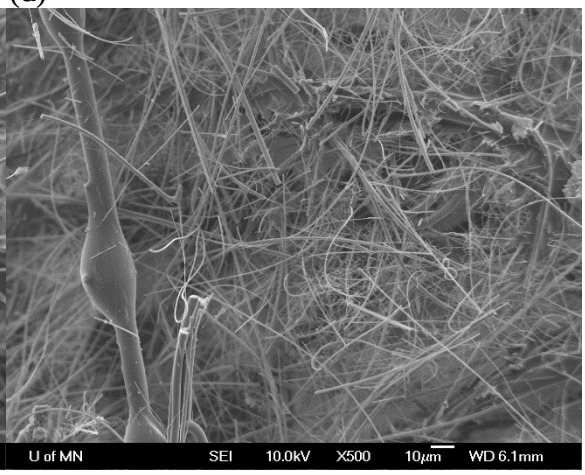
U of MN SEI 10.0kV X500 10μm WD 6.1mm

(e)

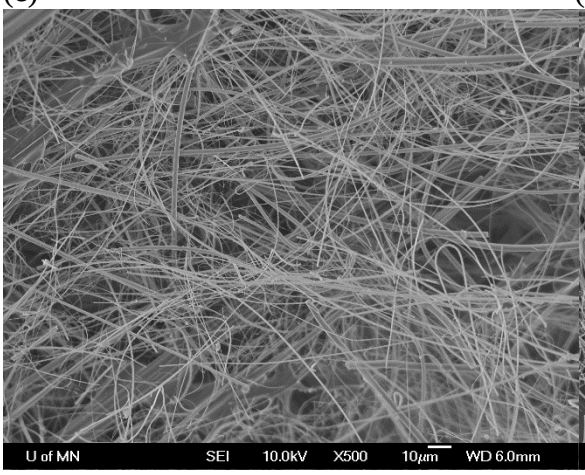
U of MN SEI 10.0kV X500 10μm WD 6.0mm

(f)

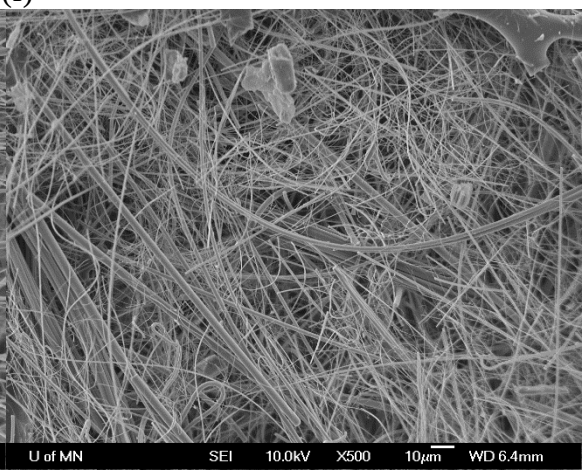
U of MN SEI 10.0kV X500 10μm WD 6.4mm

(g) (h)

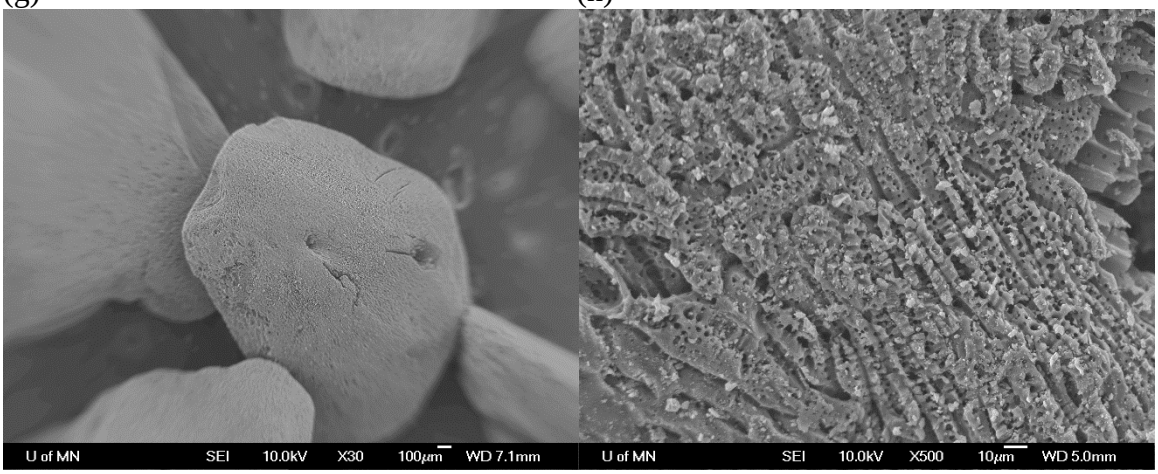

Figure 6-3. The scanning electron microscope (SEM) images of (a)-(f) the fibrous filters A-F (x500) and (g)-(h) the granular activated carbon (GAC) (x30 and x500)

Figure 6-4 shows the P of 1.5-5 nm NaCl NPs through the GAC, which was calculated through the equation (1) at different FVs (see Table 6-1). The P of the NaCl NPs increased with the particle size at the same FV as well as the FV at the same particle size due to the particle filtration mechanism, diffusion (Paretsky et al. 1971; Kim et al. 2007; Kim and Pui 2015). Previously, Kim and Pui (2015) presented the same result in the larger size range (3-30 nm ammonium sulfate ($(NH_4)_2SO_4$) particles) as shown in Figure 6-4. In addition, the current result at 3.27 cm/s overlapped well with the previous results at 2.46 and 3.93 cm/s in the particle size range 3-5 nm. Although the composition of NPs was different between the current and previous results, it was not an important factor on the P of NPs through filter media based on diffusion (Kim and Pui 2015). However, the current result at 3.27 cm/s was close to the previous result at 3.93 cm/s for the 5 nm particle. This result may have been caused by the difference of instruments, i.e., the HRDMA with the aerosol electrometer for the present work and the nano-DMA (TSI3085, TSI Inc.) with the UCPC for the previous work. The HRDMA voltage was calibrated by THABr ions with the known electrical mobility diameters (Ude and De La Mora 2005; Jiang et al. 2011), but the nano-DMA voltage was set by the tandem DMA technique (Chen et al. 1998; Stolzenburg and McMurry 2008). When the nano-DMA classified NPs at its low end size range (3-5 nm), it could become problematic due to the diffusion broadening, geometrical imperfection and space charge(Ude and De La Mora 2005). Although several unknown factors might cause the similar P at 5 nm, the current result at 3.27 cm/s still fell between the previous results at 2.46 and 3.93 cm/s. For the fibrous filters, the P of the NaCl NPs through the filters was almost zero (it was not plotted in Figure 6-4).

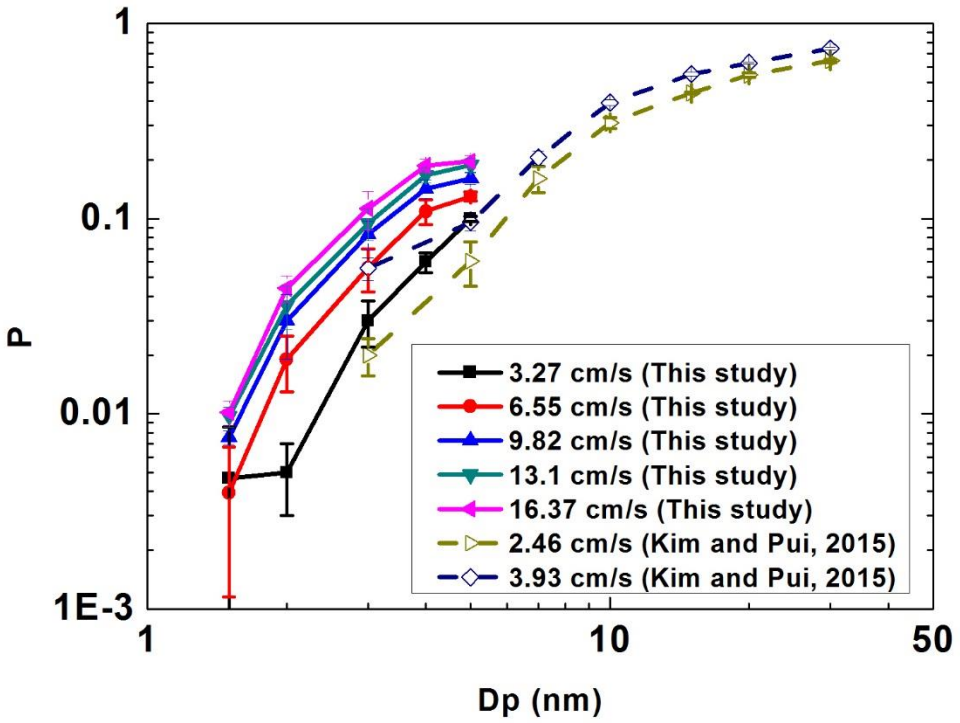

Figure 6-4. The penetration (P) of 1.5-5 nm sodium chloride (NaCl) NPs through the granular activated carbon (GAC) at different face velocities and previous results using 3-30 nm ammonium sulfate ($(NH_4)_2SO_4$)) particles (Kim and Pui, 2015)

Figure 6-5a shows the E_d of the GAC ($E_{d,GAC}$) for 1.5-5 nm NaCl particles, which was calculated from the P in Figure 4 through the equation (2). $E_{d,GAC}$ decreased from 99.5 to 80% with the particle size and FV due to diffusion (Kim and Pui 2015). However, the E_d of all the fibrous filters as shown in Figure 6-5b was 100% at the same conditions used for evaluating the GAC. Even though the aerosol electrometer was not able to detect very low particle concentration (McMurry 2000), the fibrous filters still showed higher particle filtration efficiency than the GAC between 1.5 and 5 nm. Kim et al. (2006) also presented

100% filtration efficiency for sub-2 nm particles of fibrous filters (Kim et al. 2006). Based on the results, the fibrous filters tested in this study can be used as the respirators to prevent unexpected hazards caused by inhaled NPs (Lee et al. 2008; Eninger et al. 2008) through respiratory tracts. The GAC have lower particle filtration efficiency than the fibrous filters because it was primarily manufactured to eliminate gas molecules through adsorption. However, the GAC can be used as an additional pre-particle filter for NPs by diffusion. For example, the exhaust air of facilities (or vehicles) is a mixture of gas molecules and NPs (primarily emitted or secondarily synthesized); therefore, by using the GAC, we can reduce the number concentration of NPs simultaneously with lower ΔP than the fibrous filters, in addition to removing gas molecules. If the NPs are sufficiently small and can diffuse into the pores of the GAC, the particle filtration efficiency may be increased due to the internal deposition on the pore surfaces. The $E_{d,GAC}$ was higher than 80% for sub-5 nm particles (or 90% for sub-3 nm particles) in the present work, and it can be increased by modifying the α and t of the GAC. By reducing the particle number concentration with the GAC, the life time of particle filters behind the gas filter can be extended.

(a) (b)

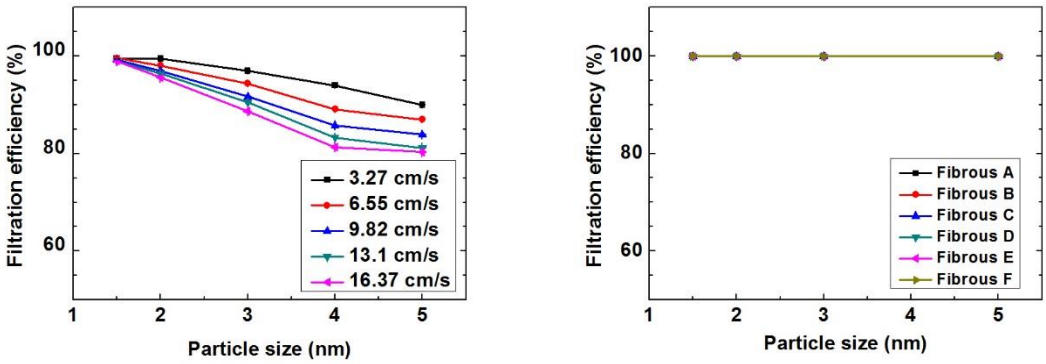

Figure 6-5. The diffusive filtration efficiency (E_d) of (a) the granular activated carbon (GAC) and (b) the fibrous filters (A-F) at different face velocities. All fibrous filters showed 100 % filtration efficiency for 1.5-5 nm sodium chloride (NaCl) particles at all tested face velocities (see in Table 6-1).

Figure 6-6a and b show the η_d according to the Pe at the two αs. The η_d was calculated from the measured P through the equation (3). The A of the η_d was changed according to the α at the same t and d_s of the GAC, i.e., 5.77 and 2.30 for $\alpha = 0.22$ and 0.44, respectively. However, the m of the fitting curves for both αs was the same as -0.35. The previous study for the larger size range (3-30 nm) also presented one m at both αs as -0.5 (Kim and Pui 2015), although the A was still changed according to the α. Lee and his colleagues (1979, 1982) derived theoretically the m as -2/3 (Lee and Gieseke 1979; Lee and Liu 1982) for the single fiber and sphere theories by diffusion. On the contrary, our results showed experimentally larger ms (-0.35 and -0.5 as shown in Figure 6-6c and d), and the m was a function of the Pe. If other conditions (FV, α, ds and t) are constant, the m becomes a function of the particle size (D_p) because the Pe is proportional to the D_p. In

other words, the m increased with decreasing D_p, and the diffusional collection of NPs on the pore surfaces of the GAC may increase the m at smaller D_p (Kim and Pui 2015). In addition, the m of the curve fitting for the combined size range (1.5-30 nm) turned into -0.43 (see Figure 6-6c and d), which was the same as the exponent of the empirical single fiber efficiency for 3-20 nm particles (Wang et al. 2007) investigated by Wang et al. (2007). Based on the results, the particle filtration by porous packed-beds media, such as the GAC, requires a new model to explain the m, which was higher in the ultrafine NP size range than calculated by Lee and Gieseke (1979) in their conventional single sphere theory (Lee and Gieseke 1979).

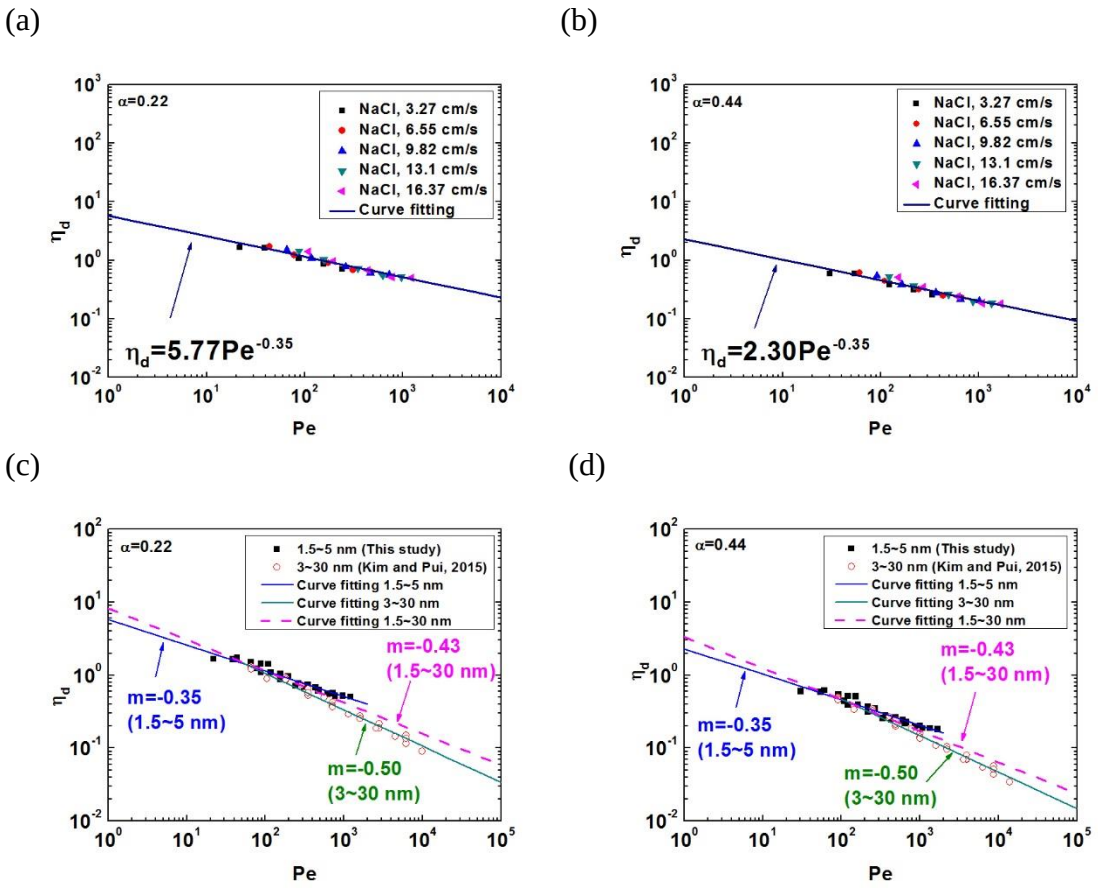

Figure 6-6. The single sphere efficiency (η_d) of the granular activated carbon (GAC) as a function of Peclet number (Pe) at α = (a) 0.22 and (b) 0.44 and exponent (m) of the power-law of Pe for each range of the particle size at a = (c) 0.22 and (d) 0.44

6.4 Summary

The P of the sub-3 nm NaCl particles through the GAC and the fibrous filters was measured to investigate the filtration efficiency of the filter media by employing the HRDMA and the aerosol electrometer. The measured P of the sub-3 nm particles was well-matched with the previous P of 3-30 nm particles through the same GAC. The filtration efficiency of the fibrous filters and the GAC for sub-3 nm particles was calculated from

the measured P, and all fibrous filters showed 100% filtration efficiency, while the GAC showed 90-99.5 % for the sub-3 nm particles. Based on the results, the fibrous filters can be used to prevent adverse effects caused by toxins adsorbed on the surface of inhaled NPs. Although the GAC showed lower filtration efficiency than the fibrous filters, it still can be a candidate material for reducing concentrations of both gas molecules and ultrafine NPs in the exhausted air. In addition, the η_d of the GAC was a power-law of the Pe, which was also observed in the conventional single sphere theory. However, the m of the power-law was different from the conventional theory. Moreover, it was the same as the exponent of the empirical single fiber efficiency in the similar particle size range. Therefore, a new filtration model for porous filter media, such as GACs, is required to understand the experimental results using ultrafine NPs including sub-3 nm particles. By investigating the particle filtration efficiency of GACs with different d_s at different α and t, the development of the new filtration model for porous packed-beds media can be facilitated. Further investigation of the simultaneous filtration for mixtures of gas molecules and NPs is also needed. If a detection method to measure neutralized sub-3 nm particles (Jiang et al. 2011) is commercially available, the further study will give results closer to the real filtration cases than the aerosol electrometer.

6.5 Supporting information (SI)

Calibration of the home-made high resolution differential mobility analyzer (HRDMA): applied voltage of the HRDMA for each particle size (D_p)

Tetraheptyl ammonium bromide (THABr) is one of the reference organic salts for the calibration of the high resolution differential mobility analyzer (HRDMA). The THABr ions can establish clusters, e.g, monomer, dimer and trimer. Each mer of the THABr ions has a well-known electrical mobility size such as 1.47 (monomer), 1.78 (dimer) and 1.97 (trimer) nm as shown in Table 6-S1. In addition, the ratios between the applied voltages of the HRDMA for classifying monomer, dimer and trimer (V_1, V_2 and V_3) are constant. Ude and de la Mora presented the reference ratios of V_1 to V_2 and V_1 to V_3 as 0.67 and 0.54(Ude and De La Mora 2005), respectively. The calibration of the HRMDA was conducted using 1) the known electrical mobility sizes and 2) the ratios between the applied voltages of the HRDMA for classifying mers as following steps.

First, the distribution of the THABr ions was measured repeatedly according to the applied voltage (50-1000 V) of the HRDMA to check the stability of the HRDMA as shown in Figure 6-S1. Figure 6-S1 shows the distribution of the THABr ions between 50 and 350 V because monomer, dimer and trimer of the THABr ions can be detected in this range. Next, V_1, V_2 and V_3 were found from the measured THABr ions distribution and the ratios of V_1 to V_2 and V_1 to V_3 were calculated. Table 6-S2 shows V_1, V_2 and V_3, which were measured thrice, and the ratios of V_1 to V_2 and V_1 to V_3 for the results. The averaged ratios of V_1 to V_2 and V_1 to V_3 were 0.65 and 0.52, respectively. The measured ratios were very close to the reference ratios (0.67 and 0.54), which means the HRDMA worked properly.

Once the good status of the HRDMA was confirmed by comparing the measured applied voltage ratios to the reference ones, the ZV for each mer was calculated by multiplying the inverse mobility (1/Z) in Table 6-S1 and the V_m in Table 6-S2. The average ZV (ZV_{avg}) of mers was 167 and used to find the applied voltages of the HRDMA (V_{HRDMA}) for the targeted particle sizes (D_p) as

$$V_{HRDMA} = \frac{ZV_{avg}}{C} \times D_p^2, \quad (1)$$

where C is a coefficient between the D_p and the V_{HRDMA} at the ZV_{avg}. When the ZV_{avg} was 167, C was 2.02, which was obtained through the equation (1) using the D_p (Table 6-S1) and the average V_{HRDMA} (Table 6-S2) for each mer of the THABr ions. Table S3 shows the V_{HRDMA} calculated through equation (1) for classifying 1.5-5.0 nanoparticles with the ZV_{avg} and C. After all experiments, the distribution of the THABr ions was measured again and compared with the distribution measured before the experiments to check the stability of the HRDMA during the experiments.

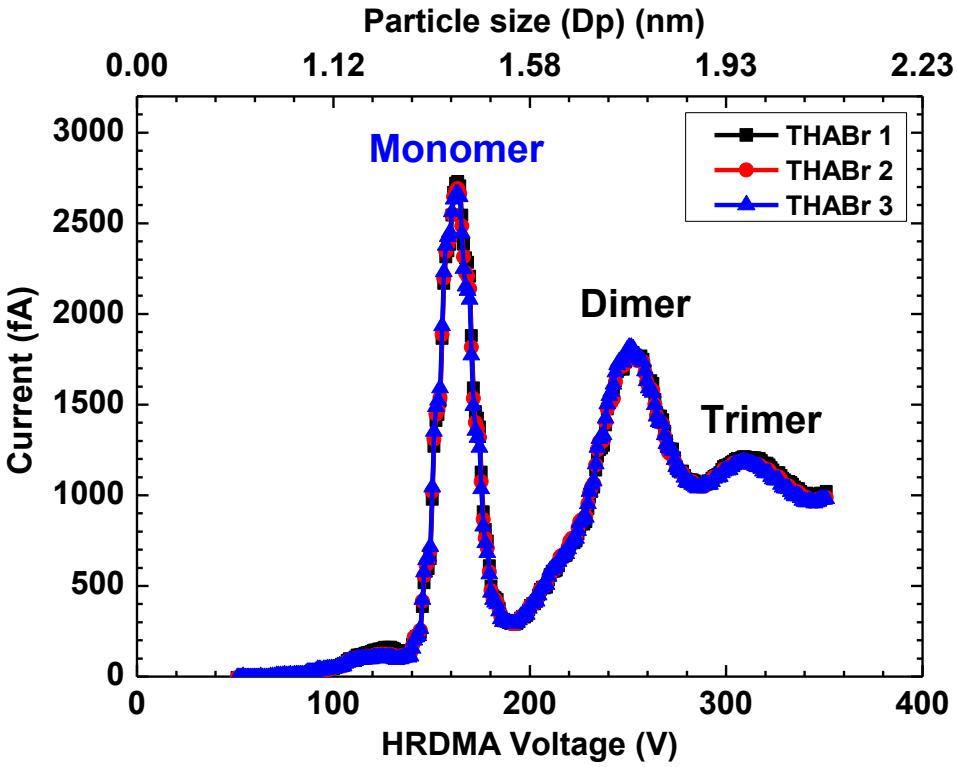

Figure 6-S1. The distribution of the THABr ions according to the applied voltage of the high resolution differential mobility analyzer (HRDMA) between 50 and 350 V, which was measured thrice. The classified nanoparticles were detected by an aerosol electrometer and the total current measured by the aerosol electrometer at each applied voltage was shown in y-axis.

Table 6-S1. The inverse mobility (1/Z) and electrical mobility size (D_p) for each mer (monomer, dimer and trimer) as well as the ratio of 1/Z between mers (1/Z for monomer divided by that for each mer) presented by Ude and de la Mora (2005).

mer	1/Z	D_p (nm)	Ratio of (1/Z)
Monomer	**1.03**	**1.47**	**1**
Dimer	**1.529**	**1.78**	**0.67**
Trimer	**1.893**	**1.97**	**0.54**

Table 6-S2. The applied voltage (V_{HRDMA}) of the HRDMA for each mer (V_m) and the ratios of V_1 to V_m. ZV for each mer was calculated by multiplying the V and the 1/Z (Table 6-S1).

No.	V_{HRDMA} (V)			Ratio of V_1/V_m		ZV		
	V_1	V_2	V_3	V_1/V_2	V_1/V_2	ZV_1	ZV_2	ZV_3
1	**172**	**259**	**326**	**0.66**	**0.53**	**167**	**169**	**172**
2	**169**	**259**	**329**	**0.65**	**0.51**	**164**	**169**	**174**
3	**169**	**260**	**326**	**0.65**	**0.51**	**164**	**170**	**172**
Avg.	**170**	**259**	**327**	**0.65**	**0.52**	**165**	**170**	**167**

Table 6-S3. The calculated V_{HRDMA} for each D_p through equation (1) at ZV_{avg} = 167.

D_p (nm)	V_{HRDMA} (V)
1.50	**186**
2.00	**330**
3.00	**745**
4.00	**1323**
5.00	**2067**

Chapter 7: Effect of The Filtered Particles on Changing Gas Adsorption Efficiency of GACs

7.1 Introduction

Activated carbons (ACs) are well-known materials for gas and liquid filtration. Due to their highly developed porosity, large surface area, variable characteristics of surface chemistry and high degree of surface reactivity, ACs are very effective adsorbents for gaseous contaminants and aqueous pollutants in liquids (Bansal and Goyal 2005; Dias et al. 2007). By using their advanced physical and chemical properties, ACs have been used in a wide range of applications for air and water treatments, e.g. drinking and waste water filters, respirators, car cabin air filters, aircraft cabin air filters, home air purifiers and cleanrooms.

Granular activated carbon (GAC) is a widely used type of ACs in the industry and vehicles for eliminating gaseous contaminants in the air using their pores as adsorption sites. During adsorption, gas molecules are diffused into the pores and adhere on the inner surface of the pores whose width matches with the gas molecule size. If the GAC is treated with counter chemicals, adsorption efficiency can be increased due to the reaction between gas molecules and chemicals on the surface of the pores (Karanfil and Kilduff 1999; Chingombe et al. 2005; Sharma et al. 2013). However, the chemical coating layer can reduce the specific surface area of the GAC or block the pores, which causes a trade-off problem. Similarly, particles deposited on the surface of the GAC can block the pores. For preventing the particle deposition, the GAC requires particle filter layers upstream of the

GAC for preventing the particle deposition. In addition, another particle filter layer is installed downstream of the GAC for removing particles generated through the disintegration of the GAC. Moreover, the sandwich-structure particle filters installed upstream and downstream of the GAC work as a holder of the GAC. While the particle filters increase the life time of the GAC by removing particles, the particle filters also increase the pressure drop (Kim et al. 2007; Wang and Otani 2012) of the total filtration system (a combination of the particle filters and the GAC), thus increasing the maintenance costs of the filtration system. If the particle filter layers can be removed or replaced with low pressure drop ones, the filtration system can be more energy- and cost-efficient.

Even if the modification of the filtration system may reduce the particle filtration efficiency, the GAC can compensate the reduction of the particle filtration efficiency, as a packed-beds filter. Recently, our group have investigated the filtration efficiency of the GAC for 1.5 – 30 nm particles through the subsequent studies and found that the GAC can eliminate nanoparticles as a packed-beds filter (Kim and Pui 2015; Kim et al. 2016a). The results showed that gaseous and particulate contaminants can be removed simultaneously using a single filter media, the GAC, i.e. nanoparticles by diffusion and gas molecules by adsorption. However, the filtered particles by the GAC may block the pores of the GAC and result in reducing the gas filtration efficiency of the GAC, which is the primary purpose why the GAC filter has been used. Therefore, investigating the effect of the filtered particles on changing gas filtration efficiency of the GAC should be conducted following the study for the particle filtration efficiency of the GAC, to apply the GAC as a single filter media for both gaseous and particulate contaminants.

In this study, we investigated the effect of the filtered particles on changing gas filtration efficiency of GACs with different granule sizes using a mixture of nanoparticles (NPs) and gas molecules. Toluene was used as the source of the gas molecules and the toluene/nanoparticles mixture were prepared in-situ through soft X-ray-radiolysis of toluene molecules (Kim et al. 2015; Kim et al. 2016b). Then, the penetration of toluene when the GACs were challenged by the toluene/NPs mixture was measured by the soft X-ray-assisted detection method for gas contamination (Kim et al. 2015) and plotted as a function. The time-resolved penetration of toluene through the GACs was compared with that when the GACs were challenged by only toluene molecules to determine the effect of the filtered particles on the gas adsorption efficiency. The properties (e.g. specific surface area, pore size distribution, and granule size) of the GACs used in this study were also analyzed for figuring out their effects on the difference of the GACs.

7.2 Materials and methods

Figure 7-1a shows the experimental setup for studying the effect of the filtered particles on changing gas filtration efficiency of the GACs using the toluene/mixture and toluene only. The experimental setup consisted of the two parts for preparing the toluene/NPs mixture and measuring the time-resolved penetration of toluene through the GACs, and both parts deployed soft X-ray to accomplish their purposes. For preparing the toluene/NPs mixture, which was one of the upstream conditions for the GACs, the toluene molecules were evaporated from the liquid toluene in the VOC chamber and introduced to the 1st soft X-ray radiolysis chamber. The nitrogen gas (N_2, UHP grade) was used as the

carrier gas for this study after removing its intrinsic particulate and gaseous contaminants through the high efficiency particulate air (HEPA) and activated carbon filters. The evaporation rate of the liquid toluene (Sigma-Aldrich, Co.) in the VOC chamber was 1 ml/hr at 25 °C, which corresponded to 1925 ppmV at 2 lpm N_2 (see the supporting information for the details in calculating the concentration of toluene in ppmV from the evaporation rate in ml/hr). In the 1st soft X-ray chamber, a part of the introduced toluene molecules was converted into polydisperse NPs through the soft X-ray assisted gas-to-particle conversion (Kim et al. 2015), thus forming the toluene/NPs mixture downstream of the 1st soft X-ray chamber. The dimension of the chamber was 5 in. diameter and 8 in. height. The bulk residence time in the chamber was 75s at 2 lpm or 100s at 1.5 lpm. For the other upstream condition, toluene only, was prepared by turning off the 1st soft X-ray. Then, no particle generation occurred in the 1st soft X-ray chamber, and only toluene molecules were prepared downstream of the chamber. The toluene molecules (toluene only) or toluene/NPs mixture was introduced to the GAC holder at 1.5 lpm, and each 10 ml GAC was contained in the GAC holder with 36 mm diameter. In the GAC holder, the stainless steel mesh was used to hold the GACs when the GAC holder was placed horizontally during the experiments. The face velocity of the gas stream through the GACs was fixed at 2.46 cm/s (Kim and Pui 2015). The toluene concentrations upstream and downstream of the GAC holder were measured by the soft X-ray assisted detection method (Kim et al. 2015), which consists of the 2nd soft X-ray radiolysis chamber and the scanning mobility particle sizer (SMPS, 3082 and 3085, TSI, Inc.). The aerosol and sheath flow rates were set at 1.5 and 15 lpm, and the corresponding particle size range for the SMPS

measurement was from 2.5 to 65 nm. Before measuring the toluene concentration by the soft X-ray assisted detection method, nanoparticles were removed by the HEPA filter in front of the 2nd soft X-ray chamber to avoid errors by the particles downstream of the GACs. After converting the toluene molecules into nanoparticles in the 2nd soft X-ray chamber, the number distribution of the nanoparticles was measured by the SMPS, and the volume distribution was calculated from the measured number distribution by assuming all particles were spherical. By integrating the volume distribution, the total particle volume concentration (Vp) was calculated and plotted as a function of time, up to 180 min (3 hours) as the time-resolved penetration of toluene through the GACs (see Figure 7-5). The time-resolved penetration of toluene was compared with the upstream toluene concentration (1925 ppmV), which corresponded to ~2.1 x 10^8 nm^3/cm^3 in Vp. The measurement of the time-resolve penetration was conducted thrice and averaged for each GAC. For the toluene/NPs upstream condition, NPs were introduced to the GACs at 60 min by turning on the 1st soft X-ray.

(a)

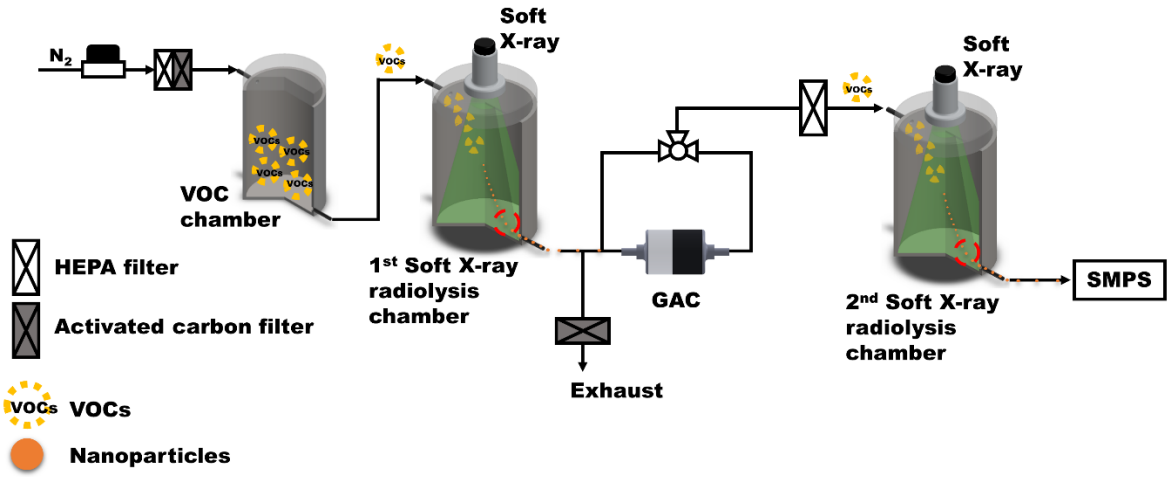

(b)

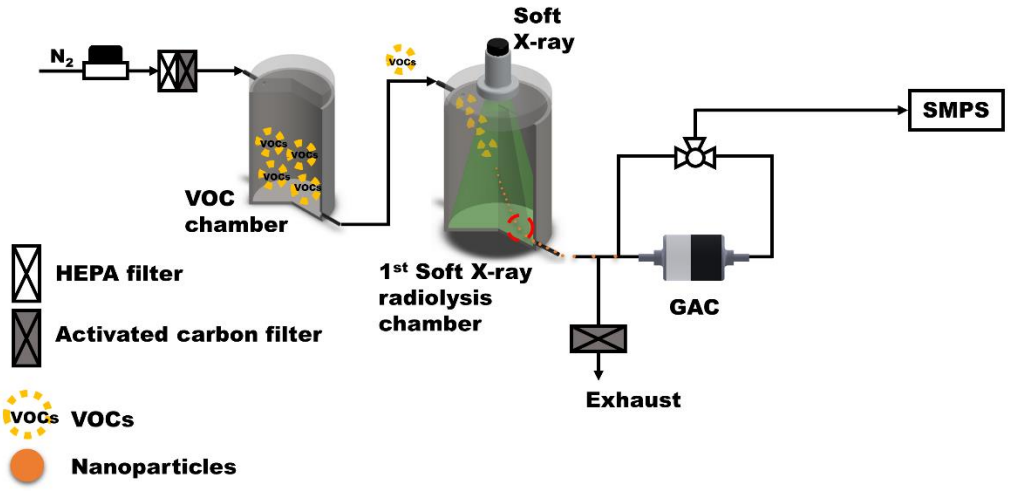

Figure 7-1. Experimental setup for measuring (a) time-resolved penetration of toluene and (b) penetration of nanoparticles through granular activated carbons (GACs)

The total number concentration of the nanoparticles (Np) collected on the GACs when the toluene/NPs mixture was introduced to the GACs was obtained from the penetration of the toluene-based nanoparticles through the GACs, which was measured by the SMPS in the experimental setup as shown in Figure 7-1b. The penetration of the nanoparticles through the GACs was calculated from the ratio of the number concentration of the nanoparticles downstream to that upstream of each GAC at each particle size (Dp, 2.5 – 65 nm) (see Figure 7-4a) through

$$\text{Penetration (Dp)} = \frac{\text{Number concetration of NPs downstream of the GAC}}{\text{Number oncentration of Nps upstream of the GAC}} \quad (1)$$

and plotted as a function of the Dp, as shown in Figure 7-4b. From the measured penetration of the nanoparticles, the Np was calculated as

$$\mathrm{N_p} = \int_{2.5\ nm}^{65\ nm} (1 - \text{penetration}) \times \text{number concentration of NP upstream of the GAC dDp}, \quad (2)$$

and plotted as an accumulative column in the five different Dp ranges with a 10 nm interval as shown in Figure 7-4d.

The diameter of the toluene molecule is in the range of sub-nm (Oh et al. 2008). In addition, the equivalent diameter of the toluene molecule ($d_{toluene}$) was calculated based on its diffusion coefficient ($D_{toluene}$), ~$8x10^{-6}$ m^2/s at 20 °C (Erbil and Avci 2002) by the following equation (Hinds 1998):

$$\mathrm{D_{toluene}} = \frac{kTC_c}{3\pi\nu d_{toluene}}, \quad (3)$$

where k is Boltzmann's constant, T is the temperature, C_c is the slip correction factor and ν is the viscosity of the N_2. As a result, $d_{toluene}$ was ~0.84 nm at 20 °C.

In this study, five GACs with different granule sizes were investigated. GAC0 was same as the commercial GAC (GVP-403, 3M, Co.) used in the previous studies (Kim and Pui 2015; Kim et al. 2016a) and other GACs were provided by 3M, Co. The properties (e.g. granule size, surface structure, pore size distribution and specific surface area) of the GACs were analyzed before investigating the effect of the filtered particles on the gas filtration efficiency of the GACs. The granule size of each GAC was measured by a laser diffraction particle size analyzer (Blue wave, Microtrac, Inc., see the distribution as shown in Figure 7-S1) and described in Table 7-1. The GACs used in this study had different granule size between 0.22 ± 0.02 and 1.26 ± 0.15 mm. The granule size of the GAC0 was well-matched with the value provided by the manufacturer (Kim et al. 2016a). The surface structures of the GACs were also analyzed by a field-emission gun scanning electron microscope (FEG-SEM, 6500F, JEOL Ltd.) as shown in Figure 7-2. The pore size distribution and specific surface area of the GACs were determined through Barrett-Joyner-Halenda (BJH) and Brunauer-Emmet-Teller (BET) methods using a gas adsorption analyzer (ASAP-2020, Micromeritics) and depicted in Figure 7-3 and Table 7-1, respectively (Gaur et al. 2005; Ioannidou and Zabaniotou 2007; Dias et al. 2007; Schneider

et al. 2008). The GAC4 was used only to compare the properties of the GACs, because the granule size of the GAC4 was too small to hold using a stainless steel mesh in the GAC holder.

Although the upstream toluene concentration was same at 1925 ppmV, the final Vp of the time-resolved penetration of toluene (i.e. concentration of toluene) through the GACs (see Figure 7-5) measured by the soft X-ray assisted detection method was different according to the GAC. Due to the different final Vp, the time-resolved penetration curve was normalized through dividing the original penetration curve (see Figure 7-5) by the final Vp for each GAC, as shown in Figure 6. As a result, the normalized penetration ended at ~1.

7.3 Results and discussion

Figure 7-2 shows the SEM images of the five GACs used in this study. The GACs had granular shapes as shown in Figure 7-2a, which is a granule of GAC0. In addition, a lot of micro-sized pores were observed on the surface of the GACs. However, the detailed surface structure changed according to the GAC, which came from the difference of the raw materials and the preparation methods (i.e. carbonization, activation and grinding) (Ioannidou and Zabaniotou 2007; Dias et al. 2007). In addition, nano-sized pores, which capture gas molecules during adsorption, were not clearly seen in the SEM images (Kim et al. 2016a).

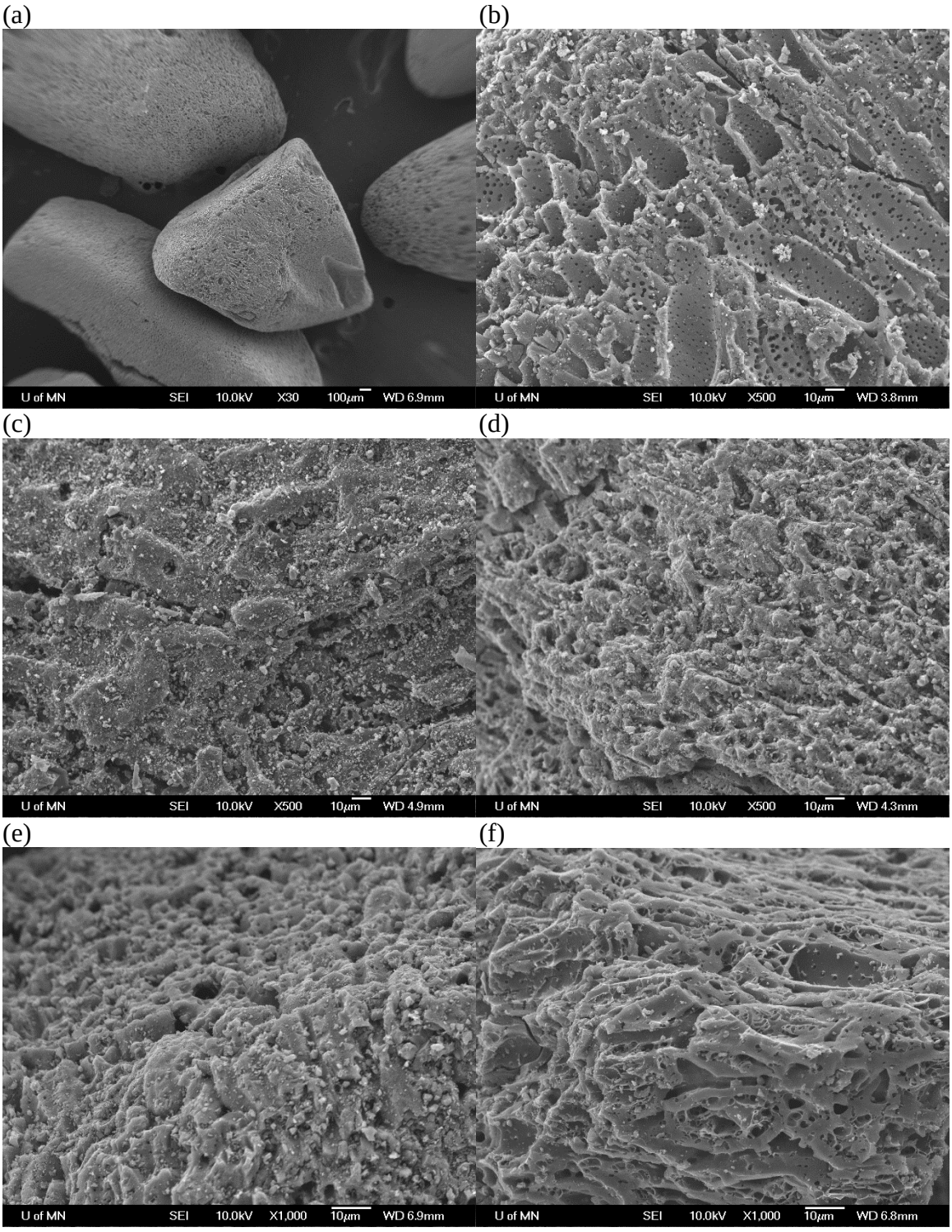

Figure 7-2. Scanning electron microscopy (SEM) images of (a) GAC0 (x50), (b) GAC0 (x500), (c) GAC1 (x500), (d) GAC2 (x500), (e) GAC3 (x1000) and (f) GAC4 (x1000)

The nano-sized pores measured by BJH method are shown in Figure 7-3. The peak sizes of the pores of the distributions for the GACs were 2, 4.7 and 23 nm. Because the BJH method can measure mesopores (2-50 nm) (Gaur et al. 2005), the smallest pore size seems to be smaller than 2 nm (micropore size range). The micropores (< 2nm) and macropores (> 50 nm) of the GACs are not shown in the pore volume distributions. Although the intensity of 4.7 nm peaks was different according to the GACs, the GACs had similar volume distributions. In addition, most of their pores were micropores, which were suitable for capturing toluene molecules effectively due to the sub-nm $d_{toluene}$ (Moreno-Castilla 2004).

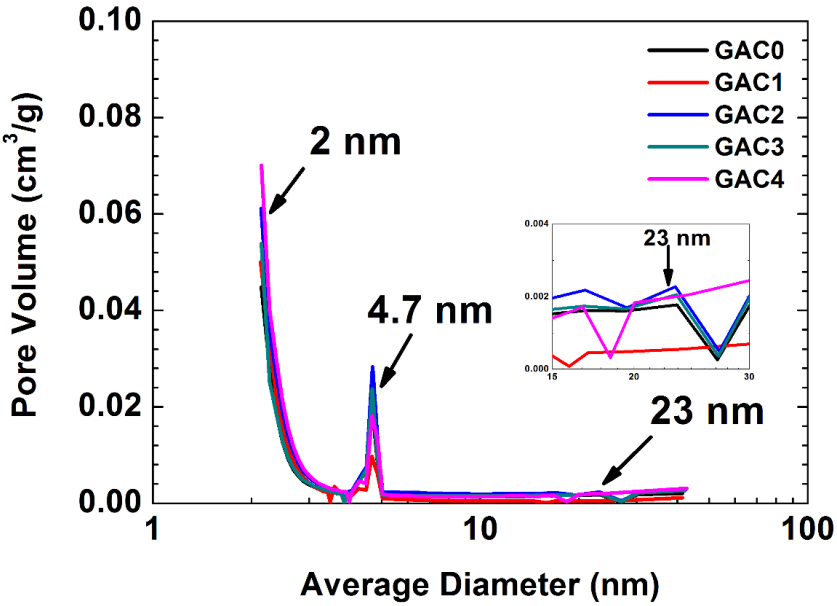

Figure 7-3. Pore volume distributions measured by the Barrett-Joyner-Halenda (BJH) method

Table 7-1 shows the granule size and BET specific surface area (S_{BET}) of the GACs. The S_{BET} of the GACs was over 1,000 m^2/g and increased with decreasing granule size. Interestingly, the S_{BET} of GAC3 (1209.20 m^2/g) was lower than that of GAC2 (1237.70 m^2/g), even though the granule size of the GAC3 (0.4 ± 0.04 mm) was smaller than half of the granule size of GAC2 (0.92 ± 0.09 mm). This phenomenon might come from the difference of the pore volume intensity at 4.7 and 23 nm between the two GACs, as shown in Figure 3. GAC2 had higher pore volume than GAC3 at the two peaks. The different surface structures of the two GACs (see Figure 2d and e) also can cause the phenomenon because the S_{BET} consists of the external surface area and pore surface area of the GACs, and the pore surface area contributes dominantly to the S_{BET} (Miyamoto et al. 2005). GAC2 seems to have more pores than GAC3, thus having larger S_{BET} than GAC3.

Table 7-1. Granule size and specific surface area of the GACs, which were measured by the laser diffraction particle size analyzer and the Brunauer-Emmet-Teller (BET) method, respectively.

GAC	Granule size (mm)	BET specific surface area (m^2/g)
GAC0	**1.26 ± 0.15**	**1182.08 ± 30.61**
GAC1	**1.26 ± 0.15**	**1079.19 ± 28.49**
GAC2	**0.92 ± 0.09**	**1237.70 ± 31.89**
GAC3	**0.4 ± 0.04**	**1209.20 ± 31.54**
GAC4	**0.22 ± 0.02**	**1331.89 ± 35.18**

Kim and his colleagues studied the filtration efficiency of the GACs for nanoparticles, which decreased with the particle size (Kim and Pui 2015; Kim et al. 2016a). Figure 7-4b also shows increasing penetration of nanoparticles through the GACs with the particle size due to decreasing particle filtration efficiency (i.e. penetration = 1 - filtration efficiency). The particle penetration through the GAC0 using the polydisperse NPs was well-matched with the previous results using 3-30 nm monodisperse NPs classified by a differential mobility analyzer (3085, TSI Inc.) (Kim and Pui 2015). Therefore, using polydisperse NPs can save time for measuring particle penetration through the GACs, instead of using monodisperse NPs. In addition, Figure 7-4a and b show increasing penetration with the granule size of the GAC, although the S_{BET} of GAC2 was higher than GAC3. This result implies the strong relation between the particle filtration and the external surface area of the GAC, because the external surface area of GAC3 should be much larger than other GACs based on the granule size. However, the smaller granule size also increased the pressure drop of GAC3 (see Figure 7-S2), which was not desirable for the particle filtration. Using Eq. 2, the Np calculated from the measured particle penetration was in the range of $1.5 – 2.0 \times 10^5$ #/cm^3 for the GACs, as shown in Figure 4d. Although the Np was different according to the GACs, most of the sub-10 nm particles upstream of the GACs were collected on the GACs because diffusion increased with decreasing particle size, as shown in Figure 7-4c. Moreover, the GACs captured more large-sized particles (> 10 nm) when the granule size was smaller, due to the larger external surface area.

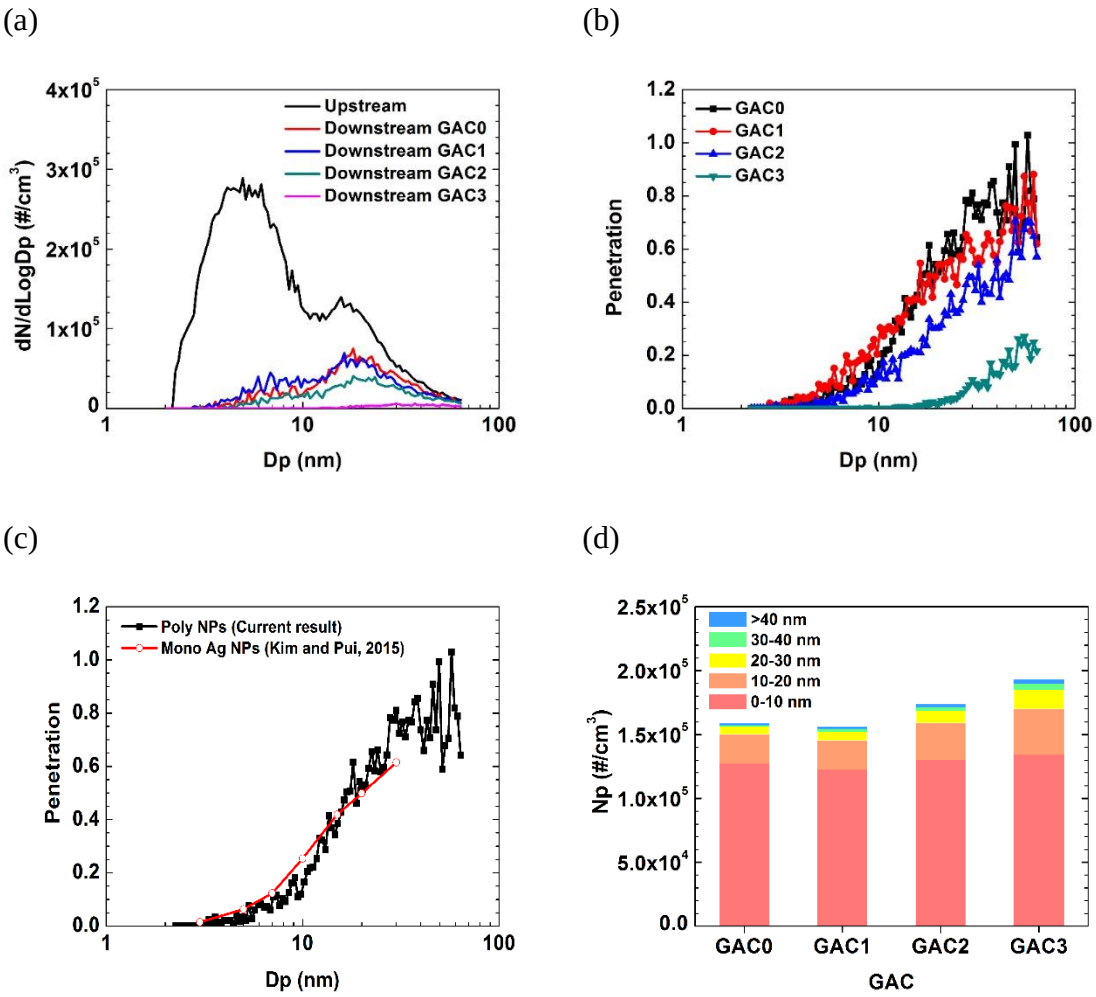

Figure 7-4. (a) Number distributions of nanoparticles upstream and downstream of the GACs, (b) penetration of nanoparticles calculated from the measured number distributions, (c) comparison of the penetration of nanoparticles through GAC0 between polydisperse (current study) and monodisperse NPs (Kim and Pui, 2015), and (d) cumulative total particle number concentration (Np) collected on each GAC

Figure 7-5a-c show the time-resolved penetrations of toluene through the GACs at the two upstream conditions, such as toluene only and toluene/NPs mixture for GAC0, GAC1 and GAC2. The time-resolved penetration curves for GAC0 – GAC2 represented the breakthrough of the GACs with the breakpoint at 90 min (Moreno-Castilla 2004; Bansal and Goyal 2005). The toluene penetration through GAC0 – GAC2 increased in the beginning and showed the plateau at ~2 x 10^7 nm^3/cm^3 (~10% of the upstream toluene concentration) between 30 and 90 min. Then, the toluene penetration increased again and approached to 2 – 2.4 x 10^8 nm^3/cm^3 in Vp. The penetration curves of GAC0 – GAC2 when the toluene/NPs mixture was introduced to them were overlapped with the penetration curves when only toluene molecules were introduced to them. In the overlapped penetration curves, no significant effect of the filtered NPs on changing gas filtration efficiency of the GACs was observed.

When the breakthrough of the GACs were done, GAC0 and GAC1 showed the final Vp in 5% difference (see Figure 7-5a and b) with the upstream toluene concentration, but the GAC2 showed 10 – 15 % (~2.3 – 2.4 x 10^7 nm^3/cm^3, see Figure 5c) higher final Vp than the upstream toluene concentration. The increased downstream toluene concentration might come from desorption of the toluene molecules on the external surface of the GAC. As described in Table 7-1, GAC2 had 25% smaller granule size (0.92 ± 0.09 mm) than GAC0 and GAC1 (1.26 ± 0.15 mm), thus increasing the external surface area of GAC2 in the same volume. Due to the larger external surface area, more toluene molecules could be adsorbed on the external surface of GAC2 than GAC0 and GAC1. Then, the toluene molecules on the external surface of the GAC2 were desorbed again by the carrier gas,

when the carrier gas passed through the GAC2. The desorbed toluene molecules increased the downstream toluene concentration than the upstream toluene concentration. Although the increasing downstream toluene concentration among GAC0 – GAC2 was not significantly high, it was much higher for GAC3 than GAC0 – GAC2. Because GAC3 (0.4 ± 0.04 mm) had much smaller granule size than GAC0 – GAC2, more toluene molecules were adsorbed on and desorbed from the external surface of GAC3, thus increasing the final Vp (toluene concentration downstream of the GACs) as shown in Figure 7-5d. Although GAC3 can remove more particles than other GACs as shown in Figure 7-4, the GAC3 was not considered further due to its worse characteristics such as higher pressure drop and final Vp.

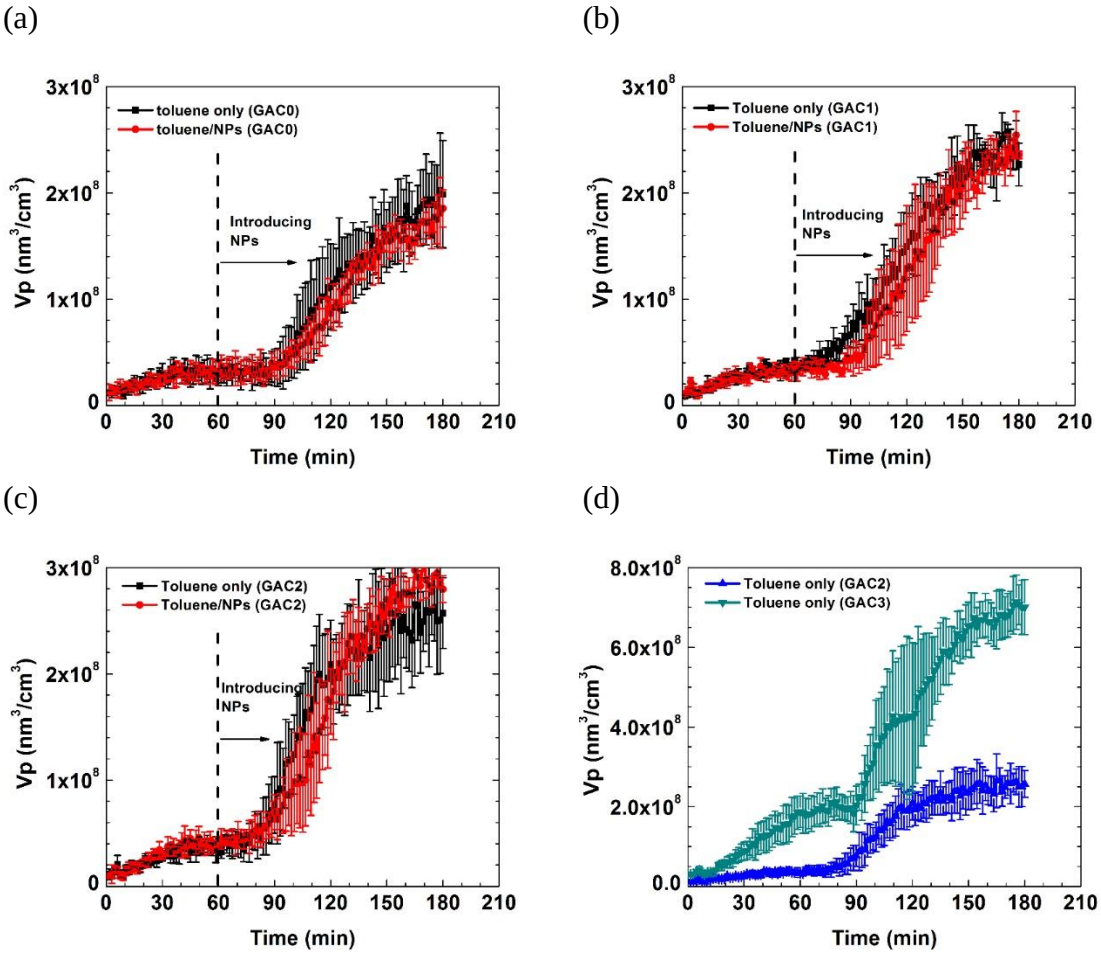

Figure 7-5. Time-resolved penetrations of toluene through the GACs at two upstream conditions, such as toluene only and toluene/nanoparticles mixture for (a) GAC0, (b) GAC1, (c) GAC2 and (d) GAC3

Figure 7-6 shows the normalized penetration of toluene through GAC0 – GAC2 (GAC3 was excluded in this normalization). Although the final Vp of the time-resolved penetration curves in Figure 7-5 was different according to the GACs, the normalized penetration curves for GAC0 – GAC2 were converged with the final penetration at ~1, as shown in Figure 6a and b. In the normalized penetration curves, the breakpoint was also at 90 min for both upstream conditions. By the normalization, the effect of the toluene

molecules desorbed from the external surface of the GAC was eliminated. Because toluene molecules were diffused into and captured at micropores (< 2 nm), the normalized penetration curves were converged without the effect of the desorbed toluene molecules. Figure 7-6c and d show the normalized penetrations of toluene through GAC0 and GAC2, which were same between the two upstream conditions (GAC1 also had same normalized penetration between the two upstream conditions, but was not shown in Figure 7-6). As the time-resolved penetration of toluene through GAC0 – GAC2, the normalized penetrations also showed no significant effect of the filtered particles on changing gas filtration efficiency of the GACs.

While measuring the penetration of toluene in 180 min for the GACs, the particle penetration through the GACs did not change, which was lower than 0.2 for sub-10 nm particles and higher than 0.5 for particles larger than 30 nm as shown in Figure 7-4b. The same particle penetration after filling up the pores with toluene molecules represented the external deposition of the NPs on the GACs, not much in the pores of the GACs. In addition, the filtered nanoparticles larger than 30 nm did not block the pores of the GACs significantly due to their high penetration through the GACs. Although most particles collected on the GACs were sub-10 nm particles, they did not significantly reduce the gas filtration efficiency of the GACs neither as shown in Figure 7-5 and 7-6. Based on the results, the GACs can be used to remove gas molecules by on the pore surface of the GACs and NPs (e.g. sub-10 nm) by the external surface of the GACs simultaneously, without decreasing gas filtration efficiency by the filtered particles.

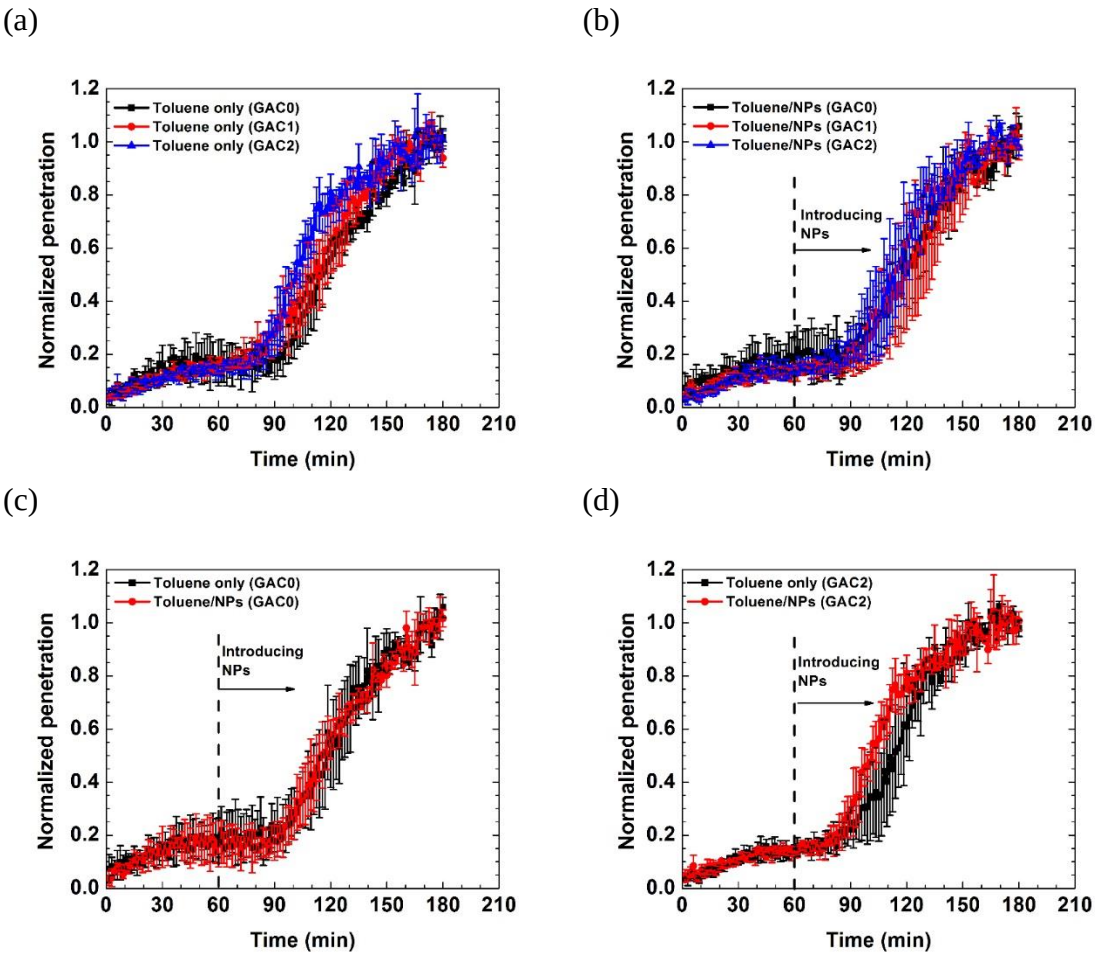

Figure 7-6. Normalized penetration of toluene through the GACs at the two upstream conditions such as (a) toluene only and (b) toluene/nanoparticles mixture; comparison of the normalized penetration of toluene through (c) GAC0 and (d) GAC2 between two upstream conditions

7.4 Summary

The effect of the filtered particles on changing gas filtration efficiency of the GACs were investigated in this study using the toluene/NPs mixture. The tolulene/NPs mixture was prepared in-situ by the soft X-ray assisted gas-to-particle conversion and introduced to the GACs. The toluene concentration downstream of the GACs were measured by the soft X-ray assisted detection method and plotted as a function of time up to 180 min. Three different GACs (GAC0 – GAC2) showed same trend of the time-resolved penetration of toluene, which was also observed in the normalized penetration curves. The experimental result exhibited that the nanoparticles collected on the GACs did not affect significantly on the gas filtration efficiency of the GACs. Even though the majority of the particles collected on the GACs were sub-10 nm particles and the particles might go through and deposited in the pores of the GACs, the nanoparticles did not change the gas filtration efficiency of the GACs. Particles larger than the pore sizes also could not change the gas filtration efficiency by blocking the pores, due to the low number concentration of the large particles collected on the GACs. In addition, particles were dominantly captured on the external surfaces of the GACs, not much in their pores. Based on the results, gas molecules and nanoparticles (e.g. sub-10 nm) can be removed simultaneously by a single gas filter, GAC.

7.5 Supporting information (SI)

(a)

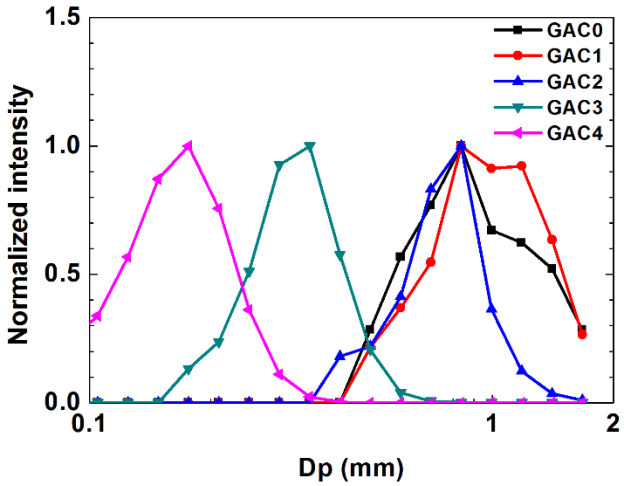

(b)

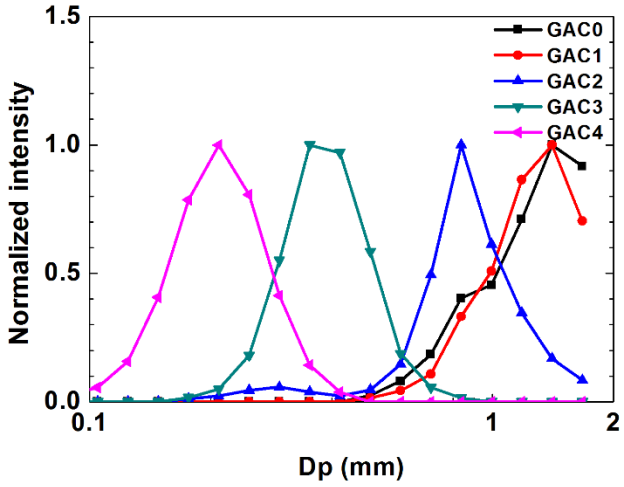

Figure 7-S1. Size distributions of the granular activated carbons (GACs) measured by the laser diffraction particle size analyzer: (a) number distribution (b) volume distribution. Each distribution was normalized by its peak intensity.

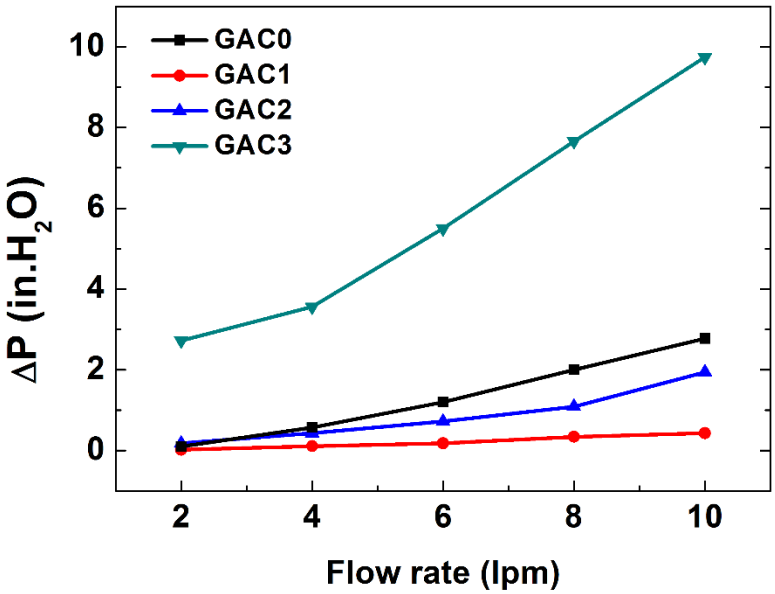

Figure 7-S2. Pressure drop (ΔP, in. H_2O) across the granular activated carbons (GACs) measured by magnehelic pressure gauges: GAC0 – GAC3. ΔP for GAC4 was not measured because the granule size of GAC4 was too small to hold by the stainless steel mesh.

Calculation of the toluene concentration upstream of the granular activated carbons (GACs)

From the ideal gas law,

PV = nRT,

$$\mathrm{V_{tol}} = \frac{nRT}{P} = \frac{M_{tol}}{Mw_{tol}} \times \frac{RT}{P}.$$

Using the properties as P=1 atm, R=0.0821 atm/molK, T=298 K, M_{tol}=1 ml/hr=14.5 mg/min and Mw_{tol}=92.14 g/mol,

$$\mathrm{V_{tol}} = \frac{1.45 \times 10^{-2} g/min}{9.214 \times 10^{1}\ g/mol} \times \frac{0.0821 \frac{atm}{molK} \times 298\ K}{1\ atm} l = 0.00385\ = 3.85 \times 10^{-3} l/min$$

$$\mathrm{ppmV} = \frac{\mathrm{V_{tol}}}{V_{N_2}} \times 10^{6} = \frac{3.85 \times 10^{-3} l/min}{2\ l/min} \times 10^{6} = 1.925 \times 10^{3} ppmV$$

IV. Conclusion

Chapter 8: Conclusion and Future Works

8.1 Summary and conclusion

In this dissertation, the detection method for AMC was developed by employing the soft X-ray-assisted gas-to-particle conversion and applied to diverse issues related to detection and filtration of AMC in cleanrooms. The newly developed soft X-ray-assisted detection method was on-line, real-time, simple and applicable for detecting diverse AMCs originated from different sources in cleanrooms, e.g. SO_2, organic compounds and outgassing from cleanroom-use materials and $PM_{2.5}$.

Chapter 2 describes the scheme of the soft X-ray-assisted detection method for AMC and its application to evaluate the gas filtration performance of two AMC filters (i.e. GAC) for SO_2 as a function of time. In this chapter, the AMC detection method showed its high sensitivity, which corresponded to ppt-level SO_2, and the measured concentration was well-matched to the reading of the commercial SO_2 monitor. By converting SO_2 molecules into nanoparticles and measuring them using the SMPS, this method measured the concentration of SO_2 downstream of the AMC filters from ppt to ppb or higher level SO_2 and determined a better AMC filter for preventing SO_2 from entering cleanrooms.

Chapter 3 discusses the use of the soft X-ray-assisted detection method to screen cleanroom-use materials by measuring their outgassing. For the screening purpose, the outgassing chamber was installed before the soft X-ray radiolysis chamber. By heating the outgassing chamber up to 200 °C, the measurement of outgassing can be accelerated. The measurements of VOCs from the super glue and different organic compounds showed the

high sensitivity and repeatability of this method. Subsequently, the VOC emission of the cleanroom-use adhesives was evaluated by this method, and the overall trend of the measured VOCs was well-matched with those measured by TD-GC-MS, which is a widely used off-line method for analyzing VOCs. Based on the results, this screening method can help accelerate the developing process for low-VOC materials used in cleanrooms.

In Chapter 4, the soft X-ray method was applied to determine the relation between $PM_{2.5}$ mass loading and its outgassing. The $PM_{2.5}$ samples were collected at Xi'an, China, which is currently suffering from the problems caused by high concentration of $PM_{2.5}$. After shipped to UMN, the outgassing from the $PM_{2.5}$ samples was measured by the soft X-ray method, and the measured outgassing changed linearly with the $PM_{2.5}$ mass loading. Simultaneously, the chemical analyses were conducted using the TOR, IC and TD-GC-MS, which showed the strong relation between OC and the outgassing measured by the soft X-ray and the effect of the sampling location on the composition of the outgassing. Based on the results, the soft X-ray method can be used to estimate the changing period of the filters in the manufacturing facilities because the temperature condition for the soft X-ray was closer to the real filtration condition in the semiconductor industry.

In Chapter 5 through 7, the soft X-ray method was employed to investigate the effects of the filtered particles on changing gas filtration efficiency of GACs. Before studying the effects of the filtered particles on gas adsorption efficiency of GACs, the particle filtration of GACs was investigated to figure out the feasibility of removing particles using GACs as packed-beds filters. First, Chapter 5 reports the filtration efficiency of GACs for 3-30 nm particles at different particle compositions and face velocities. The

particle filtration efficiency did not change according to the particle composition, but did with the FV, which followed the previous models for fibrous filters and packed-beds. In addition, the experimental results revealed that the particle filtration efficiency of the GAC could not be explained simply by the single sphere efficiency model for the packed-beds, despite its granular shape. The particle filtration behavior of GACs studied in this chapter can help design filters including GACs for both gaseous and particulate contaminants such as activated carbon embedded HEPA filters.

Next, Chapter 6 addresses the filtration efficiency of GACs for sub-3 nm particles and compares the results with that of fibrous respirators by employing the HRDMA and the aerosol electrometer. The filtration efficiency of the fibrous filters and the GAC for sub-3 nm particles was calculated from the measured P, and all fibrous filters showed 100% filtration efficiency, while the GAC showed 90-99.5 % for the sub-3 nm particles. Although the GAC showed lower filtration efficiency than the fibrous filters, it still can be a candidate material for reducing concentrations of both gas molecules and ultrafine NPs in the exhausted air. In addition, the single unit filtration efficiency of the GAC had the same exponent of the empirical single fiber efficiency in the similar particle size range. This also implies that a new filtration model for porous filter media, such as GACs, is required to understand their particle filtration efficiency.

In Chapter 7, the effect of the filtered particles on changing gas filtration efficiency of GACs was presented by measuring the time-dependent penetration of toluene through the GACs using the soft X-ray-assisted detection method. The three different GACs showed the same trend of time-resolved penetration of toluene. The experimental result

exhibited that the nanoparticles collected on the GACs did not affect significantly on the gas filtration efficiency of the GACs. Most of sub-10 nm particles were collected by the GACs, but did not change their gas filtration efficiency. Particles larger than the pore sizes also could not influence the gas filtration efficiency by blocking the pores, due to the low number concentration of the large particles collected on the GACs. In addition, the same particle filtration efficiency through the measurement presented particle deposition on the external surfaces of the GACs. Therefore, gas molecules and nanoparticles (in particular, sub-10 nm) can be removed simultaneously by a single gas filter, GAC.

The detection method for AMC assisted by soft X-ray developed in this dissertation can help increase yield of products and reduce maintenance costs in the semiconductor industry by several ways, e.g. monitoring AMC in cleanrooms and optimizing changing periods of filters. In addition, the method can provide strong background knowledge to improve the filtration systems in the semiconductor industry for AMC and nanoparticles with better characteristics, such as thinner thickness, lower pressure drop and costs.

8.2 Future works

The soft X-ray-assisted detection method for AMC developed in this dissertation can be improved in a few ways according to its applications.

1. In Chapter 2, this method was used to measure the filtration efficiency of the AMC filters for SO_2 conditioned at 50 ± 5 % RH and 23 ± 2 °C. In addition, the bulk residence time in the soft X-ray chamber was also fixed at 100 s. For other

inorganic AMCs, this method should be tested at multiple levels of RH, temperature and residence time to find optimal conditions for each AMC.

2. Correlation equations between AMC and the AMC originated particles should be found for estimating the concentration of AMC in terms of gas concentration, e.g. ppb or ppt. Because the cleanroom air includes many different kinds of AMCs, the effect of the reactions between two or more AMCs is required to study for avoiding the errors caused by the chemical reactions.
3. The design of the soft X-ray chamber also can be optimized by changing the direction of the soft X-ray irradiation and the size of the chamber. In this study, some AMCs could not be detected by this method including the SMPS. The SMPS used in this study could measure nanoparticles between 2.5 and 65 nm. Using other advanced aerosol instruments, such as 1 nm SMPS (TSI Inc., recently produced), the undetected AMCs can be measured. Moreover, the optimal condition for each AMC can be found, thus extending the application of this method.

In addition, the particle filtration efficiency of GACs and the effects of the filtered particles on changing gas filtration efficiency of the GACs can be conducted further by the following ways.

4. For measuring the filtration efficiency of the GACs for sub-3 nm particles, the aerosol electrometer could detect only charged particles. If the 1 nm SMPS is employed, neutralized particles smaller than 3 nm can be measured, which is closer to the particle filtration in the real situation.

5. In this study, only GACs were evaluated for the particle filtration efficiency. Other activated carbons can be investigated as particle filters. In particular, activated carbon fiber (ACF) is a good candidate material for removing gas molecules and nanoparticles simultaneously with lower pressure drop. The study on the gas and particle filtration efficiency of ACFs can be useful to produce better filtration systems for the cleanroom air and other fields, such as car and aircraft cabin air.
6. Finally, the GACs showed different filtration trends with the previous single sphere efficiency, although they had granular shapes. Modeling for the particle filtration behavior through the GACs (or ACFs later) will be helpful to design and optimize the filtration systems for the fields mentioned above.

Bibliography

Abbas I, Saint-Georges F, Billet S, et al (2009) Air pollution particulate matter ($PM_{2.5}$)-induced gene expression of volatile organic compound and/or polycyclic aromatic hydrocarbon-metabolizing enzymes in an in vitro coculture lung model. Toxicol Vitr 23:37–46. doi: 10.1016/j.tiv.2008.09.020

Akimoto H (2003) Global air quality and pollution. Science 302:1716–1719. doi: 10.1126/science.1092666

Atkinson R (2000) Atmospheric chemistry of VOCs and NO_x. Atmos Environ 34:2063–2101. doi: 10.1016/S1352-2310(99)00460-4

Attwood D (2000) Soft x-rays and extreme ultraviolet radiation: Principles and applications. Cambridge University Press, Cambridge; New York

Bailey J, Ettinger Y, Fisher A, Feder R (1982) Evaluation of the gas puff z pinch as an x-ray lithography and microscopy source. Appl Phys Lett 40:33–35. doi: 10.1063/1.92908

Bansal RC, Goyal M (2005) Adsorption. CRC Press, Boca Raton

Barro R, Regueiro J, Llompart M, Garcia-Jares C (2009) Analysis of industrial contaminants in indoor air: Part 1. Volatile organic compounds, carbonyl compounds, polycyclic aromatic hydrocarbons and polychlorinated biphenyls. J Chromatogr A 1216:540–566. doi: 10.1016/j.chroma.2008.10.117

Berndt T (2005) Rapid Formation of Sulfuric Acid Particles at Near-Atmospheric Conditions. Science (80-) 307:698–700. doi: 10.1126/science.1104054

Berndt T, Böge O, Stratmann F (2006) Formation of atmospheric $H_2SO_4H_2O$ particles in the absence of organics: A laboratory study. Geophys Res Lett. doi: 10.1029/2006GL026660

Berndt T, Stratmann F, Bräsel S, et al (2008) SO_2 oxidation products other than H_2SO_4 as a trigger of new particle formation – Part 1 : Laboratory investigations. Atmos Chem Phys J1 - ACP 8:9761–9782. doi: 10.5194/acp-8-6365-2008

Berndt T, Stratmann F, Sipilä M, et al (2010) Laboratory study on new particle formation from the reaction OH + SO_2: influence of experimental conditions, H_2O vapour, NH_3 and the amine tert-butylamine on the overall process. Atmos Chem Phys 10:7101–7116. doi: 10.5194/acp-10-7101-2010

Billet S, Abbas I, Goff J Le, et al (2008) Genotoxic potential of Polycyclic Aromatic Hydrocarbons-coated onto airborne Particulate Matter ($PM_{2.5}$) in human lung

epithelial A549 cells. Cancer Lett 270:144–155. doi: 10.1016/j.canlet.2008.04.044

Billet S, Garçon G, Dagher Z, et al (2007) Ambient particulate matter ($PM_{2.5}$): Physicochemical characterization and metabolic activation of the organic fraction in human lung epithelial cells (A549). Environ Res 105:212–223. doi: 10.1016/j.envres.2007.03.001

Blake RS, Monks PS, Ellis AM (2009) Proton-transfer reaction mass spectrometry. Chem Rev 109:861–896. doi: 10.1021/cr800364q

Cao JJ, Lee SC, Ho KF, et al (2003) Characteristics of carbonaceous aerosol in Pearl River Delta Region, China during 2001 winter period. Atmos Environ 37:1451–1460. doi: 10.1016/S1352-2310(02)01002-6

Cao J-J, Shen Z-X, Chow JC, et al (2012a) Winter and Summer $PM_{2.5}$ Chemical Compositions in Fourteen Chinese Cities. J Air Waste Manage Assoc 62:1214–1226. doi: 10.1080/10962247.2012.701193

Cao JJ, Wang QY, Chow JC, et al (2012b) Impacts of aerosol compositions on visibility impairment in Xi'an, China. Atmos Environ 59:559–566. doi: 10.1016/j.atmosenv.2012.05.036

Cao JJ, Zhu CS, Chow JC, et al (2009) Black carbon relationships with emissions and meteorology in Xi'an, China. Atmos Res 94:194–202. doi: 10.1016/j.atmosres.2009.05.009

Chao W, Harteneck B, Liddle J, et al (2005) Soft X-ray microscopy at a spatial resolution better than 15 nm. Nature 435:1210–1213. doi: 10.1038/nature03719

Chen DR, Pui DYH, Hummes D, et al (1998) Design and evaluation of a nanometer aerosol differential mobility analyzer (Nano-DMA). J Aerosol Sci 29:497–509. doi: 10.1016/S0021-8502(97)10018-0

Chen JP, Wu S, Chong KH (2003) Surface modification of a granular activated carbon by citric acid for enhancement of copper adsorption. Carbon N Y 41:1979–1986. doi: 10.1016/S0008-6223(03)00197-0

Chingombe P, Saha B, Wakeman RJ (2005) Surface modification and characterisation of a coal-based activated carbon. Carbon N Y 43:3132–3143. doi: 10.1016/j.carbon.2005.06.021

Chow JC, Watson JG, Chen L-WA, et al (2007) The IMPROVE_A Temperature Protocol for Thermal/Optical Carbon Analysis: Maintaining Consistency with a Long-Term Database. J Air Waste Manage Assoc 57:1014–1023. doi: 10.3155/1047-3289.57.9.1014

Christensen PS, Madsen NM, Livbjerg H (1992) The formation of aerosols from SO_3 and NH_3 in humid air. J Aerosol Sci 23:261–264.

Christensen PS, Wedel S, Livbjerg H (1994) The kinetics of the photolytic production of aerosols from SO_2 and NH_3 in humid air. Chem Eng Sci 49:4605–4614. doi: 10.1016/S0009-2509(05)80044-2

Cookson Jr. JT (1970) Removal of Submicron Particles in Packed Beds. Environ Sci Technol 4:128–134. doi: 10.1021/es60037a005

Dai WT, Ho SSH, Ho KF, et al (2012) Seasonal and diurnal variations of mono- and di-carbonyls in Xi'an, China. Atmos Res 113:102–112. doi: 10.1016/j.atmosres.2012.05.001

Dallas AJ, Graham KM, Clarysse M, Fonderle V (2002) Characterization and control of organic airborne contamination in lithographic processing. In: Herr DJC (ed). SPIE, Santa Clara, CA, pp 1085–1109

Den W, Bai H, Kang Y (2006) Organic Airborne Molecular Contamination in Semiconductor Fabrication Clean Rooms. J Electrochem Soc 153:G149. doi: 10.1149/1.2147286

Dias JM, Alvim-Ferraz MCM, Almeida MF, et al (2007) Waste materials for activated carbon preparation and its use in aqueous-phase treatment: A review. J Environ Manage 85:833–846. doi: 10.1016/j.jenvman.2007.07.031

Donovan RP (1990) Particle control for semiconductor manufacturing. M. Dekker, New York

Edney EO, Driscoll DJ, Weathers WS, et al (2001) Formation of Polyketones in Irradiated Toluene/Propylene/NO_x /Air Mixtures. Aerosol Sci Technol 35:998–1008. doi: 10.1080/027868201753306769

Elsaesser A, Howard CV (2012) Toxicology of nanoparticles. Adv Drug Deliv Rev 64:129–137. doi: 10.1016/j.addr.2011.09.001

Eninger RM, Honda T, Adhikari A, et al (2008) Filter performance of N99 and N95 facepiece respirators against viruses and ultrafine particles. Ann Occup Hyg 52:385–396. doi: 10.1093/annhyg/men019

Erbil HY, Avci Y (2002) Simultaneous determination of toluene diffusion coefficient in air from thin tube evaporation and sessile drop evaporation on a solid surface. Langmuir 18:5113–5119. doi: 10.1021/la011557a

Fernández de la Mora J, Kozlowski J (2013) Hand-held differential mobility analyzers of

high resolution for 1-30nm particles: Design and fabrication considerations. J Aerosol Sci 57:45–53. doi: 10.1016/j.jaerosci.2012.10.009

Figueiredo J., Pereira MF., Freitas MM., Órfão JJ. (1999) Modification of the surface chemistry of activated carbons. Carbon N Y 37:1379–1389. doi: 10.1016/S0008-6223(98)00333-9

Fisk WJ, Faulkner D, Palonen J, Seppanen O (2002) Performance and costs of particle air filtration technologies. Indoor Air 12:223–234. doi: doi:10.1034/j.1600-0668.2002.01136.x

Forstner HJL, Flagan RC, Seinfeld JH (1997) Secondary organic aerosol from the photooxidation of aromatic hydrocarbons: Molecular composition. Environ Sci Technol 31:1345–1358. doi: 10.1021/es9605376

Fu TM, Cao JJ, Zhang XY, et al (2012) Carbonaceous aerosols in China: Top-down constraints on primary sources and estimation of secondary contribution. Atmos Chem Phys 12:2725–2746. doi: 10.5194/acp-12-2725-2012

Gaur V, Sharma A, Verma N (2005) Catalytic oxidation of toluene and m-xylene by activated carbon fiber impregnated with transition metals. Carbon N Y 43:3041–3053. doi: 10.1016/j.carbon.2005.06.039

Gebhart J, Roth C, Stahlhofen W (1973) Filtration properties of glass bead media for aerosol particles in the 0??1-2 ??m size range. J. Aerosol Sci. 4:355–371.

Geng H (2005) Semiconductor Manufacturing Handbook. McGraw-Hill, New York

Gordon J, Chan D, Frisa LE, et al (2007a) Influence of environmental components on haze growth. pp 660707–1–13

Gordon J, Frisa L, Chovino C, et al (2007b) Study of Time Dependent 193 nm Reticle Haze. pp 67301E–1–12

Gordon J, Murray B, Frisa LE, et al (2005) Use of excimer laser test system for studying haze growth. In: Weed JT, Martin PM (eds). SPIE, Monterey, CA, p 59923J–59923J–11

Gordon JS, Silova M, Connolly B, et al (2009) Contamination control for ArF photo masks. pp 1–13

Grassian VH, O'Shaughnessy PT, Adamcakova-Dodd A, et al (2007) Inhalation exposure study of Titanium dioxide nanoparticles with a primary particle size of 2 to 5 nm. Environ Health Perspect 115:397–402. doi: 10.1289/ehp.9469

Habuka H, Suzuki K, Okamura S, et al (2005) Quartz Crystal Microbalance for Silicon Surface Organic Contamination. J Electrochem Soc 152:G241. doi: 10.1149/1.1864472

Hakim M, Broza YY, Barash O, et al (2012) Volatile organic compounds of lung cancer and possible biochemical pathways. Chem Rev 112:5949–5966. doi: 10.1021/cr300174a

Han B, Shimada M, Choi M, Okuyama K (2003) Unipolar Charging of Nanosized Aerosol Particles Using Soft X-ray Photoionization. Aerosol Sci Technol 37:330–341. doi: 10.1080/02786820300962

Heim M, Attoui M, Kasper G (2010) The efficiency of diffusional particle collection onto wire grids in the mobility equivalent size range of 1.2-8 nm. J Aerosol Sci 41:207–222. doi: 10.1016/j.jaerosci.2009.10.002

Herrmann W, Eichler T, Bernardo N, Fernandez de la Mora J (2000) Turbulent Transition Arises at Reynolds Number 35,000 in a Short Vienna Type DMA with a Large Laminarization Inlet. In: Abstract AAAR Conference. St. Louis, Missouri, USA, p 15B5

Hildebrandt L, Donahue NM, Pandis SN (2009) High formation of secondary organic aerosol from the photo-oxidation of toluene. Atmos Chem Phys 9:2973–2986. doi: 10.5194/acp-9-2973-2009

Hinds W (1998) Aerosol Technoogy: properties, Behaviour and measurement of airborne particles. Wiley, New York

Huang RJ, Zhang Y, Bozzetti C, et al (2014) High secondary aerosol contribution to particulate pollution during haze events in China. Nature 514:218–222. doi: 10.1038/nature13774

Huang W, Cao J, Tao Y, et al (2012) Seasonal variation of chemical species associated with short-term mortality effects of PM 2.5 in Xi'an, a central city in China. Am J Epidemiol 175:556–566. doi: 10.1093/aje/kwr342

Huey LG, Tanner DJ, Slusher DL, et al (2004) CIMS measurements of HNO3 and SO2 at the South Pole during ISCAT 2000. Atmos Environ 38:5411–5421. doi: 10.1016/j.atmosenv.2004.04.037

Iida K, Stolzenburg MR, McMurry PH (2009) Effect of Working Fluid on Sub-2 nm Particle Detection with a Laminar Flow Ultrafine Condensation Particle Counter. Aerosol Sci Technol 43:81–96. doi: 10.1080/02786820802488194

Ioannidou O, Zabaniotou A (2007) Agricultural residues as precursors for activated

carbon production-A review. Renew Sustain Energy Rev 11:1966–2005. doi: 10.1016/j.rser.2006.03.013

Ito T, Okazaki S (2000) Pushing the limits of lithography. Nature 406:1027–1031. doi: 10.1038/35023233

Jang E, Jun S, Jang H, et al (2010) White-light-emitting diodes with quantum dot color converters for display backlights. Adv Mater 22:3076–3080. doi: 10.1002/adma.201000525

Jang M, Kamens RM (2001) Characterization of secondary aerosol from the photooxidation of toluene in the presence of NOx and 1-propene. Environ Sci Technol 35:3626–3639. doi: 10.1021/es010676+

Japuntich DA, Franklin LM, Pui DY, et al (2007) A comparison of two nano-sized particle air filtration tests in the diameter range of 10 to 400 nanometers. J Nanoparticle Res 9:93–107. doi: 10.1007/s11051-006-9179-1

Jiang J, Chen M, Kuang C, et al (2011) Electrical Mobility Spectrometer Using a Diethylene Glycol Condensation Particle Counter for Measurement of Aerosol Size Distributions Down to 1 nm. Aerosol Sci Technol 45:510–521. doi: 10.1080/02786826.2010.547538

Jimenez JL, Canagaratna MR, Donahue NM, et al (2009) Evolution of Organic Aerosols in the Atmosphere. Science (80-) 326:1525–1529. doi: 10.1126/science.1180353

Jordan A, Haidacher S, Hanel G, et al (2009) An online ultra-high sensitivity Proton-transfer-reaction mass-spectrometer combined with switchable reagent ion capability (PTR + SRI - MS). Int J Mass Spectrom 286:32–38. doi: 10.1016/j.ijms.2009.06.006

Kang Y, Den W, Bai H, Ko FH (2005) Direct quantitative analysis of phthalate esters as micro-contaminants in cleanroom air and wafer surfaces by auto-thermal desorption-gas chromatography-mass spectrometry. J Chromatogr A 1070:137–145. doi: 10.1016/j.chroma.2005.02.055

Karanfil T, Kilduff JE (1999) Role of granular activated carbon surface chemistry on the adsorption of organic compounds. 1. Priority pollutants. Environ Sci Technol 33:3217–3224. doi: 10.1021/es981016g

Katz JL, Lihavainen H, Rudek MM, Salter BC (2000) Photoinduced nucleation: A novel tool for detecting molecules in air at ultra-low concentrations. J Chem Phys 112:8363. doi: 10.1063/1.481441

Katz JL, Wen FC, McLaughlin T, et al (1977) Nucleation on photoexcited molecules.

Science 196:1203–5. doi: 10.1126/science.196.4295.1203

Keywood MD, Varutbangkul V, Bahreini R, et al (2004) Secondary organic aerosol formation from the ozonolysis of cycloalkenes and related compounds. Environ Sci Technol 38:4157–4164. doi: 10.1021/es035363o

Kim C, Kang S, Pui DYH (2016a) Removal of airborne sub-3 nm particles using fibrous filters and granular activated carbons. Carbon N Y 104:125–132. doi: 10.1016/j.carbon.2016.03.060

Kim C, Pui DYH (2015) Experimental study on the filtration efficiency of activated carbons for 3-30 nm particles. Carbon N Y 93:226–229. doi: 10.1016/j.carbon.2015.05.048

Kim C, Sul YT, Pui DYH (2016b) Real-time and On-line Screening Method for Materials Emitting Volatile Organic Compounds.

Kim C, Zuo Z, Finger H, et al (2015) Soft X-ray-assisted detection method for airborne molecular contaminations (AMCs). J Nanoparticle Res 17:126. doi: 10.1007/s11051-015-2936-2

Kim CS, Bao L, Okuyama K, et al (2006) Filtration efficiency of a fibrous filter for nanoparticles. J Nanoparticle Res 8:215–221. doi: 10.1007/s11051-005-9017-x

Kim S, Karl T, Guenther a., et al (2009) Emissions and ambient distributions of Biogenic Volatile Organic Compounds (BVOC) in a Ponderosa pine ecosystem: interpretation of PTR-MS mass spectra. Atmos Chem Phys Discuss 9:20819–20852. doi: 10.5194/acpd-9-20819-2009

Kim SC, Harrington MS, Pui DYH (2007) Experimental study of nanoparticles penetration through commercial filter media. J Nanoparticle Res 9:117–125. doi: 10.1007/s11051-006-9176-4

Kim TO, Ishida T, Adachi M, et al (1998) Nanometer-Sized Particle Formation from NH 3 /SO 2 /H 2 O/Air Mixtures by Ionizing Irradiation. Aerosol Sci Technol 29:111–125. doi: 10.1080/02786829808965556

Kirkby J, Curtius J, Almeida J, et al (2011) Role of sulphuric acid, ammonia and galactic cosmic rays in atmospheric aerosol nucleation. Nature 476:429–433. doi: 10.1038/nature10343

Kleindienst TE, Conver TS, McIver CD, Edney EO (2004) Determination of secondary organic aerosol products from the photooxidation of toluene and their implications in ambient PM2.5. J Atmos Chem 47:79–100. doi: 10.1023/B:JOCH.0000012305.94498.28

Kleindienst TE, Corse EW, Li W, et al (2002) Secondary organic aerosol formation from the irradiation of simulated automobile exhaust. J Air Waste Manag Assoc 52:259–72. doi: 10.1080/10473289.2002.10470782

Kleindienst TE, Smith DF, Li W, et al (1999) Secondary organic aerosol formation from the oxidation of aromatic hydrocarbons in the presence of dry submicron ammonium sulfate aerosol. Atmos Environ 33:3669–3681. doi: 10.1016/S1352-2310(99)00121-1

Kuang C, McMurry PH, McCormick A V., Eisele FL (2008) Dependence of nucleation rates on sulfuric acid vapor concentration in diverse atmospheric locations. J Geophys Res Atmos. doi: 10.1029/2007JD009253

Kulmala M (2003) ATMOSPHERIC SCIENCE: How Particles Nucleate and Grow. Science (80-) 302:1000–1001. doi: 10.1126/science.1090848

Kulmala M, Vehkamäki H, Petäjä T, et al (2004) Formation and growth rates of ultrafine atmospheric particles: a review of observations. J Aerosol Sci 35:143–176. doi: 10.1016/j.jaerosci.2003.10.003

Laaksonen A, Kulmala M, Berndt T, et al (2008) SO2 oxidation products other than H2SO4 as a trigger of new particle formation. Part 2: Comparison of ambient and laboratory measurements, and atmospheric implications. Atmos Chem Phys 8:7255–7264. doi: 10.5194/acp-8-7255-2008

Lebens JA, McColgin WC, Russell JB, et al (1996) Unintentional doping of wafers due to organophosphates in the clean room ambient. J Electrochem Soc 143:2906–2909.

Lee KW, Gieseke JA (1979) Collection of aerosol particles by packed beds. Environ Sci Technol 13:466–470. doi: 10.1021/es60152a013

Lee KW, Liu BYH (1982) Theoretical Study of Aerosol Filtration by Fibrous Filters. Aerosol Sci Technol 1:147–161. doi: 10.1080/02786828208958584

Lee S-A, Grinshpun S a., Reponen T (2008) Respiratory Performance Offered by N95 Respirators and Surgical Masks: Human Subject Evaluation with NaCl Aerosol Representing Bacterial and Viral Particle Size Range. Ann Occup Hyg 52:177–185. doi: 10.1093/annhyg/men005

Levard C, Mitra S, Yang T, et al (2013) Effect of Chloride on the Dissolution Rate of Silver Nanoparticles and Toxicity to E. coli. Environ Sci Technol 47:5738–5745. doi: 10.1021/es400396f

Licciardello A, Puglisi O, Pignataro S (1986) Effect of organic contaminants on the oxidation kinetics of silicon at room temperature. Appl Phys Lett 48:41. doi:

10.1063/1.96755

Lin I-K, Bai H, Wu B (2010) Analysis of Relationship between Inorganic Gases and Fine Particles in Cleanroom Environment. Aerosol Air Qual Res. doi: 10.4209/aaqr.2009.10.0065

Lobert JM, Cate PW, Ruede DJ, et al (2010) Advances in the understanding of low molecular weight silicon formation and implications for control by AMC filters. In: Raymond CJ (ed). SPIE, San Jose, CA, pp 763832–1–9

Lobert JM, Miller CM, Grayfer A, Tivin AM (2009) Measurement of low molecular weight silicon AMC to protect UV optics in photo-lithography environments. In: Allgair JA, Raymond CJ (eds). SPIE, San Jose, CA, pp 727222–1–12

Ma H, Williams PL, Diamond S a. (2013) Ecotoxicity of manufactured ZnO nanoparticles – A review. Environ Pollut 172:76–85. doi: 10.1016/j.envpol.2012.08.011

McCash EM (2001) Surface chemistry. Oxford University Press, Oxford; New York

McKenzie DR, Muller D, Pailthorpe BA (1991) Compressive-stress-induced formation of thin-film tetrahedral amorphous carbon. Phys Rev Lett 67:773–776. doi: 10.1103/PhysRevLett.67.773

McMurry P (2000) A review of atmospheric aerosol measurements. Atmos Environ 34:1959–1999. doi: 10.1016/S1352-2310(99)00455-0

Menon S, Hansen J, Nazarenko L (2002) Climate Effects of Black Carbon Aerosols in China and India. 297:2250–2254.

Miyamoto JI, Kanoh H, Kaneko K (2005) The addition of mesoporosity to activated carbon fibers by a simple reactivation process. Carbon N Y 43:855–857. doi: 10.1016/j.carbon.2004.10.049

Mølhave L, Bach B, Pedersen OF (1986) Human reactions to low concentrations of volatile organic compounds. Environ Int 12:167–175. doi: 10.1016/0160-4120(86)90027-9

Mølhave L, Clausen G, Berglund B, et al (1997) Total Volatile Organic Compounds (TVOC) in Indoor Air Quality Investigations. Indoor Air 7:225–240. doi: 10.1111/j.1600-0668.1997.00002.x

Moreno-Castilla C (2004) Adsorption of organic molecules from aqueous solutions on carbon materials. Carbon N Y 42:83–94. doi: 10.1016/j.carbon.2003.09.022

Mugisidi D, Ranaldo A, Soedarsono JW, Hikam M (2007) Modification of activated carbon using sodium acetate and its regeneration using sodium hydroxide for the adsorption of copper from aqueous solution. Carbon N Y 45:1081–1084. doi: 10.1016/j.carbon.2006.12.009

Munson MS, Field F-H (1966) Chemical ionization mass spectrometry. I. General introduction. J Am Chem Soc 88:2621–2630.

Nie Z, Petukhova A, Kumacheva E (2010) Properties and emerging applications of self-assembled structures made from inorganic nanoparticles. Nat Nanotechnol 5:15–25. doi: 10.1038/nnano.2009.453

Oh GY, Ju YW, Kim MY, et al (2008) Adsorption of toluene on carbon nanofibers prepared by electrospinning. Sci Total Environ 393:341–347. doi: 10.1016/j.scitotenv.2008.01.005

Paretsky L, Theodore L, Pfeffer R, Squires AM (1971) Panel Bed Filters for Simultaneous Removal of Fly Ash and Sulfur Dioxide:: II. Filtration of Dilute Aerosols by Sand Beds. J Air Pollut Control Assoc 21:204–209. doi: 10.1080/00022470.1971.10469520

Park SS, Jung SA, Gong BJ, et al (2013) Characteristics of PM2.5 haze episodes revealed by highly time-resolved measurements at an air pollution monitoring supersite in Korea. Aerosol Air Qual Res 13:957–976. doi: 10.4209/aaqr.2012.07.0184

Pedata P, Stoeger T, Zimmermann R, et al (2015) "Are we forgetting the smallest, sub 10 nm combustion generated particles?" Part Fibre Toxicol 12:34. doi: 10.1186/s12989-015-0107-3

Peng G, Tisch U, Adams O, et al (2009) Diagnosing lung cancer in exhaled breath using gold nanoparticles. Nat Nanotechnol 4:669–673. doi: 10.1038/nnano.2009.235

Pic N, Martin C, Vitalis M, et al (2010) Defectivity decrease in the photolithography process by AMC level reduction through implementation of novel filtration and monitoring solutions. In: Raymond CJ (ed). SPIE, San Jose, CA, pp 76380M–1–12

Pitts JN, Grosjean D, Van Cauwenberghe K, et al (1978) Photooxidation of aliphatic amines under simulated atmospheric conditions: formation of nitrosamines, nitramines, amides, and photochemical oxidant. Environ Sci Technol 12:946–953. doi: 10.1021/es60144a009

Pui DYH, Chen SC, Zuo Z (2014) $PM_{2.5}$ in China: Measurements, sources, visibility and health effects, and mitigation. Particuology 13:1–26. doi: 10.1016/j.partic.2013.11.001

Reiss G, Hütten A (2005) Magnetic nanoparticles: Applications beyond data storage. Nat Mater 4:725–726. doi: 10.1038/nmat1494

Riddle Vogt S, Landoni C (2011) Approaches to airborne molecular contamination assessment. 7971:79712I–79712I–7. doi: 10.1117/12.881654

Rivera-Utrilla J, Sánchez-Polo M (2011) Adsorbent-adsorbate interactions in the adsorption of organic and inorganic species on ozonized activated carbons: a short review. Adsorption 17:611–620. doi: 10.1007/s10450-011-9345-3

Salata O (2004) Applications of nanoparticles in biology and medicine. J Nanobiotechnology 2:3. doi: 10.1186/1477-3155-2-3

Sato K, Hatakeyama S, Imamura T (2007) Secondary organic aerosol formation during the photooxidation of toluene: NOx dependence of chemical composition. J Phys Chem A 111:9796–9808. doi: 10.1021/jp071419f

Schmidt EW, Gieseke J a., Gelfand P, et al (1978) Filtration Theory for Granular Beds. J Air Pollut Control Assoc 28:143–146. doi: 10.1080/00022470.1978.10470582

Schneider P, Hudec P, Solcova O (2008) Pore-volume and surface area in microporous-mesoporous solids. Microporous Mesoporous Mater 115:491–496. doi: 10.1016/j.micromeso.2008.02.024

Schueler BW (1992) Microscope imaging by time-of-flight secondary ion mass spectrometry. Microsc Microanal Microstruct 3:119–139. doi: 10.1051/mmm:0199200302-3011900

Sematech International (2011) International technology roadmap for semiconductors (ITRS).

SEMI Standard F21-95 (1996) Semiconductor Equipment and Materials International (SEMI).

Semonin OE, Luther JM, Choi S, et al (2011) Peak External Photocurrent Quantum Efficiency Exceeding 100% via MEG in a Quantum Dot Solar Cell. Science (80-) 334:1530–1533. doi: 10.1126/science.1209845

Sharma M, Vyas RK, Singh K (2013) A review on reactive adsorption for potential environmental applications. Adsorption 19:161–188. doi: 10.1007/s10450-012-9436-9

Sihto S-L, Kulmala M, Kerminen V-M, et al (2006) Atmospheric sulphuric acid and aerosol formation: implications from atmospheric measurements for nucleation and early growth mechanisms. Atmos Chem Phys 6:4079–4091.

Smith JN, Moore KF, McMurry PH, Eisele FL (2004) Atmospheric Measurements of Sub-20 nm Diameter Particle Chemical Composition by Thermal Desorption Chemical Ionization Mass Spectrometry. Aerosol Sci Technol 38:100–110. doi: 10.1080/02786820490249036

Stevie FA, Martin Jr. EP, Kahora PM, et al (1991) Boron contamination of surfaces in silicon microelectronics processing: Characterization and causes. J Vac Sci Technol A Vacuum, Surfaces, Film 9:2813. doi: 10.1116/1.577206

Stolzenburg MR, McMurry PH (2008) Equations Governing Single and Tandem DMA Configurations and a New Lognormal Approximation to the Transfer Function. Aerosol Sci Technol 42:421–432. doi: 10.1080/02786820802157823

Tamaoki M, Uemura E, Nishiki K, et al (2010a) Influence of airborne H2S on haze generation in ArF lithography. IEEE, pp 1–4

Tamaoki M, Uemura E, Nishiki K, et al (2010b) Influence of airborne H_2S on haze generation in ArF lithography. pp 1–4

Tennant MF, Mazyck DW (2007) The role of surface acidity and pore size distribution in the adsorption of 2-methylisoborneol via powdered activated carbon. Carbon N Y 45:858–864. doi: 10.1016/j.carbon.2006.11.009

Tiwari S, Srivastava AK, Bisht DS, et al (2010) Black carbon and chemical characteristics of PM10 and PM2.5 at an urban site of North India. J Atmos Chem 62:193–209. doi: 10.1007/s10874-010-9148-z

Ude S, De La Mora JF (2005) Molecular monodisperse mobility and mass standards from electrosprays of tetra-alkyl ammonium halides. J Aerosol Sci 36:1224–1237. doi: 10.1016/j.jaerosci.2005.02.009

Veillerot M, Danel A, Cetre S, Tardif F (2003) Deposition kinetic of airborne organic contamination on wafers measured by TD-GC/MS. Mater Sci Eng B 102:385–389. doi: 10.1016/S0921-5107(02)00628-1

Wang C, Otani Y (2012) Removal of Nanoparticles from Gas Streams by Fibrous Filters: A Review. Ind Eng Chem Res 52:120712152932002. doi: 10.1021/ie300574m

Wang J, Chen DR, Pui DYH (2007) Modeling of filtration efficiency of nanoparticles in standard filter media. J Nanoparticle Res 9:109–115. doi: 10.1007/s11051-006-9155-9

Weineck G, Zastera D, Dallas AJ, et al (2010) AMC Control in Photolithography : The Past Decade in Review. In: Raymond CJ (ed) SPIE Proceedings. SPIE, San Jose, CA, CA, pp 1–9

Weir A, Westerhoff P, Fabricius L, et al (2012) Titanium Dioxide Nanoparticles in Food and Personal Care Products. Environ Sci Technol 46:2242–2250. doi: 10.1021/es204168d

Wood WP, Castleman AWJ, Tang IN (1975) Mechanisms of aerosol formation from SO2. J Aerosol Sci 6:367–374.

Yong Z, Mata VG, Rodrigues AE (2001) Adsorption of Carbon Dioxide on Chemically Modified High Surface Area Carbon-Based Adsorbents at High Temperature. Adsorption 7:41–50.

Yun KM, Lee SY, Iskandar F, et al (2009) Effect of X-ray energy and ionization time on the charging performance and nanoparticle formation of a soft X-ray photoionization charger. Adv Powder Technol 20:529–536. doi: 10.1016/j.apt.2009.07.002

Zhang R, Suh I, Zhao J, et al (2004) Atmospheric New Particle Formation Enhanced by Organic Acids. Science (80-) 304:1487–1490. doi: 10.1126/science.1095139

Zhao J, Smith JN, Eisele FL, et al (2011) Observation of neutral sulfuric acid-amine containing clusters in laboratory and ambient measurements. Atmos Chem Phys 11:10823–10836. doi: 10.5194/acp-11-10823-2011

Zhu C-S, Cao J-J, Ho K-F, et al (2015) The optical properties of urban aerosol in northern China: A case study at Xi'an. Atmos Res 160:59–67. doi: 10.1016/j.atmosres.2015.03.008

Zhu C-S, Cao J-J, Tsai C-J, et al (2014) Comparison and implications of $PM_{2.5}$ carbon fractions in different environments. Sci Total Environ 466-467:203–9. doi: 10.1016/j.scitotenv.2013.07.029

Appendix

This Appendix contains copies of copyright permissions granted by the owners of the journals when the work is published.

Title: Soft X-ray-assisted detection method for airborne molecular contaminations (AMCs)
Author: Changhyuk Kim
Publication: Journal of Nanoparticle Research
Publisher: Springer
Date: Jan 1, 2015

Order Completed

Thank you for your order.

This Agreement between Changhyuk Kim ("You") and Springer ("Springer") consists of your license details and the terms and conditions provided by Springer and Copyright Clearance Center.

Your confirmation email will contain your order number for future reference.

Get the printable license.

License Number	3883211175440
License date	Jun 06, 2016
Licensed Content Publisher	Springer
Licensed Content Publication	Journal of Nanoparticle Research
Licensed Content Title	Soft X-ray-assisted detection method for airborne molecular contaminations (AMCs)
Licensed Content Author	Changhyuk Kim
Licensed Content Date	Jan 1, 2015
Licensed Content Volume	17
Licensed Content Issue	3
Type of Use	Thesis/Dissertation
Portion	Full text
Number of copies	1
Author of this Springer article	Yes and you are the sole author of the new work
Order reference number	
Title of your thesis / dissertation	Soft X-Ray-Assisted Detection Method for Airborne Molecular Contamination (AMC) and its Applications to AMC Filtration Issues
Expected completion date	Jul 2016
Estimated size(pages)	160
Requestor Location	Changhyuk Kim 111 Church St. SE MINNEAPOLIS, MN 55455 United States Attn: Changhyuk Kim
Billing Type	Invoice
Billing address	Changhyuk Kim 111 Church St. SE

MINNEAPOLIS, MN 55455
United States
Attn: Changhyuk Kim

Total 0.00 USD

ORDER MORE CLOSE WINDOW

Title: Experimental study on the filtration efficiency of activated carbons for 3–30nm particles
Author: Changhyuk Kim,David Y.H. Pui
Publication: Carbon
Publisher: Elsevier
Date: November 2015

Order Completed

Thank you for your order.

This Agreement between Changhyuk Kim ("You") and Elsevier ("Elsevier") consists of your license details and the terms and conditions provided by Elsevier and Copyright Clearance Center.

Your confirmation email will contain your order number for future reference.

Get the printable license.

License Number	3883210983412
License date	Jun 06, 2016
Licensed Content Publisher	Elsevier
Licensed Content Publication	Carbon
Licensed Content Title	Experimental study on the filtration efficiency of activated carbons for 3–30nm particles
Licensed Content Author	Changhyuk Kim,David Y.H. Pui
Licensed Content Date	November 2015
Licensed Content Volume	93
Licensed Content Issue	n/a
Licensed Content Pages	4
Type of Use	reuse in a thesis/dissertation
Portion	full article
Format	both print and electronic
Are you the author of this Elsevier article?	Yes
Will you be translating?	No
Order reference number	
Title of your thesis/dissertation	Soft X-Ray-Assisted Detection Method for Airborne Molecular Contamination (AMC) and its Applications to AMC Filtration Issues
Expected completion date	Jul 2016
Estimated size (number of pages)	160
Elsevier VAT number	GB 494 6272 12
Requestor Location	Changhyuk Kim 111 Church St. SE MINNEAPOLIS, MN 55455 United States Attn: Changhyuk Kim
Total	0.00 USD

ORDER MORE CLOSE WINDOW

Title: Removal of airborne sub-3 nm particles using fibrous filters and granular activated carbons

Author: Changhyuk Kim,Seungkoo Kang,David Y.H. Pui

Publication: Carbon

Publisher: Elsevier

Date: August 2016

Order Completed

Thank you for your order.

This Agreement between Changhyuk Kim ("You") and Elsevier ("Elsevier") consists of your license details and the terms and conditions provided by Elsevier and Copyright Clearance Center.

Your confirmation email will contain your order number for future reference.

Get the printable license.

License Number	3883210867049
License date	Jun 06, 2016
Licensed Content Publisher	Elsevier
Licensed Content Publication	Carbon
Licensed Content Title	Removal of airborne sub-3 nm particles using fibrous filters and granular activated carbons
Licensed Content Author	Changhyuk Kim,Seungkoo Kang,David Y.H. Pui
Licensed Content Date	August 2016
Licensed Content Volume	104
Licensed Content Issue	n/a
Licensed Content Pages	8
Type of Use	reuse in a thesis/dissertation
Portion	full article
Format	both print and electronic
Are you the author of this Elsevier article?	Yes
Will you be translating?	No
Order reference number	
Title of your thesis/dissertation	Soft X-Ray-Assisted Detection Method for Airborne Molecular Contamination (AMC) and its Applications to AMC Filtration Issues
Expected completion date	Jul 2016
Estimated size (number of pages)	160
Elsevier VAT number	GB 494 6272 12
Requestor Location	Changhyuk Kim 111 Church St. SE MINNEAPOLIS, MN 55455 United States Attn: Changhyuk Kim
Total	0.00 USD

ORDER MORE CLOSE WINDOW